Dalton Transactions

ROYAL SOCIETY OF CHEMISTRY

PERSPECTIVE

View Article Online
View Journal | View Issue

Cite this: *Dalton Trans.*, 2026, **55**, 1548

Tracking *in situ* transformation of metal–organic frameworks into layered double hydroxides during synthesis and alkaline water oxidation through *operando* mechanistic studies

Meena Chettri, [a] Nilankar Diyali [a] and Bhaskar Biswas *[a,b]

Received 2nd July 2025,
Accepted 25th November 2025

DOI: 10.1039/d5dt01557j

rsc.li/dalton

Metal-organic frameworks (MOFs) have become powerful precursors for generating layered double hydroxides (LDHs) with excellent oxygen evolution reaction (OER) activity, yet the mechanistic pathways guiding their transformation remain unclear. Existing reviews largely emphasize synthetic routes and performance metrics, leaving the real-time structural and chemical evolution of MOF-derived LDHs fragmented. This work fills that gap by providing the focused overview of the in situ/operando mechanisms that govern MOF-to-LDH conversion and their electrocatalytic function. We summarize the fundamentals of water oxidation, outline the chemical principles that drive LDH formation from MOFs, and highlight how phase evolution under synthetic and electrochemical environments dictates OER activity. Advances in *in situ/operando* characterization, Raman spectroscopy, Attenuated Total Reflectance Fourier-transform infrared (ATR-FTIR), Electrochemical Impedance Spectroscopy (EIS), X-ray absorption spectroscopy (XAS), X-ray photoelectron spectroscopy (XPS), liquid-cell transmission electron microscopy (LCTEM), etc., are integrated with DFT insights to construct a unified picture of intermediate species, structural dynamics, and thermodynamic stability. We further discuss how defect chemistry, metal-oxygen flexibility, and dissolution-reprecipitation behaviour shape durability under harsh OER conditions. The perspective concludes with key challenges and future opportunities for mechanistically guided design of next-generation MOF-derived LDH electrocatalysts.

1. Introduction

Layered double hydroxides (LDHs) have emerged as one of the most promising classes of non-precious electrocatalysts for water splitting, offering a cost-effective and sustainable alternative to noble metals such as Pt, Ir, and Ru.[1–7] LDHs are a class of two-dimensional (2D) anionic clays with the general formula $[M_{1-x}^{2+}M_x^{3+}(OH)_2]^{x+}[A_{x/n}]^{n-}\cdot mH_2O$, where divalent Ni^{2+}, Co^{2+}, Cu^{2+}, or Zn^{2+}, *etc.* and trivalent Fe^{3+}, Mn^{3+}, Al^{3+}, *etc.* metal cations are integrated into positively charged nanoscale layers *via* covalent bonding. These layers are intercalated with anions like CO_3^{2-}, OH^-, NO^{3-}, and SO_4^{2-} and water molecules and are stabilized through electrostatic interactions and hydrogen bonding.

The unique two-dimensional (2D) structure of LDHs provides abundant active sites, tunable composition, and excellent stability, making them particularly attractive for the electrocatalytic hydrogen evolution reaction (HER) and oxygen evolution reaction (OER) in alkaline media. LDHs possess abundant hydrophilic and hydroxyl groups that anchor reactants, while exposed metal centers offer numerous active sites for fast kinetics.[8] Also, the synergistic interaction between divalent and trivalent cations tunes electronic states, enhancing charge transfer and catalytic activity, making LDHs promising alternatives to noble metal catalysts for efficient, scalable hydrogen production.[9,10]

In this context, metal–organic framework (MOF)-derived LDHs have gained considerable attention as an advanced material design strategy. The porous and highly ordered architecture of MOFs serves as an excellent sacrificial template for constructing LDHs with enhanced conductivity, higher surface area, and tailored nanostructures[11,12] It is well known that during electrochemical OER, most transition-metal based MOFs transform into hydroxide or oxyhydroxide phases under alkaline conditions,[13] whereas LDHs represent the thermodynamically stable reconstruction product rather than a decomposed or amorphous residue. MOF-derived LDHs can inherit unique morphologies and structural features from their parent MOFs, often exhibiting increased surface areas and a high density of pores compared with that of traditional bulk materials that can limit the bulk material's practical

[a]*Laboratory for Structural Engineering & Sustainable Catalysis, Department of Chemistry, University of North Bengal, Darjeeling, West Bengal, 734013, India. E-mail: bhaskarbiswas@nbu.ac.in, bhaskarbiswas@ait.ac.th*
[b]*Department of Energy and Climate Change, School of Environment, Resources and Development, Asian Institute of Technology, Pathumthani 12120, Thailand*

use.[14] The anion-exchangeable interlayer gallery also buffers volume changes during potential cycling, improving durability. This makes MOF-derived LDHs a more sustainable and scalable pathway toward industrial-grade water-splitting catalysts.[15,16]

In situ transformations of MOFs into LDHs have gained growing interest due to their pseudomorphic nature, where the original morphology of MOFs, such as hollow cages, nanosheets, or nanorods, is remarkably preserved.[17,18] This pseudomorphic transformation allows for the creation of nanomaterials with precisely tailored porosity and architecture, unlocking new avenues for designing advanced materials with optimized functionality. Integrating *in situ*-derived LDHs with highly conductive supports such as nickel foam (NF), carbon nanotubes (CNTs), graphene, MXenes *etc.* further boosts electrical conductivity and overall catalytic performance.[19–22] Collectively, these improvements lead to significantly enhanced electrocatalytic water-splitting (EWS) performance, characterized by lower overpotentials, higher current densities, and superior cycling stability.

The development of advanced synthetic designs also demands an understanding of the formation mechanism of electrocatalysts.[23,24] Not only that, the overall understanding of the reaction mechanism under operational conditions is critical. As such, *in situ*/*operando* characterization has proved to be a powerful tool for elucidating the dynamic chemical and structural transformations that occur on electrocatalyst surfaces during WS.[25] These techniques allow real-time monitoring of catalysts under actual working conditions, bridging the gap between static characterization and true catalytic behaviour. Many catalysts undergo structural and/or electronic transformations during electrolysis; in such cases, *operando* studies reveal the active species for catalysis.[26,27] Also, these techniques detect phase transitions, oxidation state changes, and lattice strain in real time, which are essential for understanding catalyst activation/deactivation.[28–30]

Operando measurements under prolonged conditions reveal when, where, and how catalysts transform or reconstruct, *e.g.*, leaching, amorphization, thus aiding the design of more robust and durable systems.[31,32] *Operando* studies are indispensable for uncovering the true catalytic mechanisms in WS, thus enabling the rational design of more active, stable, and earth-abundant electrocatalysts. Without such *in situ* observations, many insights would remain speculative or misleading due to the dynamic nature of catalyst surfaces under electrochemical conditions. Recently, our group has fabricated a bifunctional electrocatalyst for WS, by growing NBU-1 MOF crystals on the surface of NF (NBU-1/NF) and subsequent *in situ* transformation to oxyhydroxide material (NBU-1/NF@CoOOH) through electro-oxidation.[33]

In this context, this work provides a comprehensive discussion that begins with the promise of and advances into the *in situ* transformation of MOFs into LDHs, and culminates in the mechanistic exploration of their *in situ* evolution, an aspect that has been overlooked in prior reviews. This focus not only distinguishes the review from prior work but also offers guidance for the rational design and study of next-generation catalysts capable of driving sustainable energy.

Meena Chettri

Ms. Meena Chettri is a Senior Research Fellow (SRF) and doctoral candidate in the field of material chemistry at the Laboratory for Structural Engineering & Sustainable Catalysis, University of North Bengal, under the guidance of Prof. Bhaskar Biswas. She holds a B.Sc. degree in Chemistry from Darjeeling Government College (2018) and a Master's degree in Chemistry from Sikkim University, Gangtok (2020). In 2023, she qualified for the Graduate Aptitude Test in Engineering (GATE) in chemical sciences. Her research centers on designing and optimizing transition-metal–based electrocatalysts for efficient overall water splitting. Emphasizing on earth-abundant materials and sustainable synthesis, her work aims to deliver scalable, energy-efficient solutions for renewable energy technologies.

Nilankar Diyali

Mr. Nilankar Diyali (MRSC) is an emerging researcher from the picturesque hills of Darjeeling, currently pursuing his PhD at the Laboratory for Structural Engineering & Sustainable Catalysis, Department of Chemistry, University of North Bengal, India, under the mentorship of Prof. Bhaskar Biswas. He completed his B.Sc. in Chemistry from St Joseph's College, Darjeeling (2018), followed by an M.Sc. in Chemistry with a specialization in Inorganic Chemistry from Sikkim University, Gangtok (2020). He has qualified, the GATE and CSIR–UGC NET examinations. Driven by a deep passion for inorganic chemistry, Nilankar works diligently on metal–organic frameworks (MOFs), focusing on their applications in electrocatalytic water splitting. His research approach reflects clarity of thought, scientific curiosity, and a collaborative mindset. Rooted in the serene landscapes of Darjeeling, Nilankar carries a sense of grounded purpose into his scientific endeavors. His work embodies a commitment to creating meaningful, impactful advances towards a cleaner and more sustainable future.

2. Scope of the review

Although numerous review articles have comprehensively documented the synthetic routes and electrochemical performances of MOF-derived electrocatalysts, including phosphides, chalcogenides, oxides, nitrides, carbides, hydroxides, and LDHs,[34–36] the crucial mechanistic aspects behind their formation and transformation remain largely fragmented. In particular, the pathway by which MOFs convert into LDHs, and the real-time structural and chemical evolution of these intermediates during electrochemical operation, has not been systematically consolidated in the existing literature. At the same time, several excellent reviews have explored *in situ*/*operando* mechanistic studies for metal-free electrocatalysts and oxide/hydroxide-based OER catalysts, which have collectively broadened our understanding of catalytic pathways.[23,25,37,38] However, MOF-derived LDHs, despite their increasing prominence, have not yet been systematically examined through the lens of *in situ*/*operando* mechanistic insights.

This review fills that critical gap. Here, we bring forward a focused and timely discussion dedicated to the *in situ*/*operando* transformation of MOF-derived LDHs and the mechanistic roles they play in the oxygen evolution reaction (OER). The novelty of this work lies in integrating mechanistic, structural, and thermodynamic perspectives that are often missing in general MOF-derived electrocatalyst reviews. We begin with a concise and comprehensive overview of water-splitting fundamentals, followed by the key chemical and structural factors governing the formation of LDHs from MOF precursors. Building upon this foundation, the central theme of the review is an in-depth analysis of how MOFs evolve into LDHs under synthetic and electrochemical environments, and how these structural transformations dictate catalytic function. To achieve this, we systematically examine the major advances in *in situ* and *operando* characterization techniques, including Liquid Cell Transmission electron microscopy (LCTEM), *operando* Raman spectroscopy, Attenuated Total Reflectance–Fourier-transform infrared (ATR-FTIR), X-ray photoelectron spectroscopy (XPS), X-ray absorption spectroscopy (XAS), electrochemical impedance spectroscopy (EIS), etc., as well as complementary DFT studies that offer atomic-level insight into phase evolution, intermediate species, and thermodynamic driving forces. By surveying progress from 2015 to 2025, we present the first consolidated framework that connects real-time structural evolution with catalytic behavior in MOF-derived LDHs. Importantly, this review also highlights the experimental and thermodynamic stability of MOF-derived LDH electrocatalysts. We discuss how features such as defect density, metal–oxygen bond flexibility, dissolution–reprecipitation dynamics, and electric double-layer effects shape catalyst durability under harsh OER conditions. These insights illuminate why certain MOF precursors yield exceptionally robust LDHs, while others degrade or restructure during operation. Finally, we outline the remaining challenges, including limitations in temporal resolution, ambiguity in identifying metastable intermediates, and the scarcity of constant-potential theoretical approaches, and propose future research opportunities that can accelerate the rational design of MOF-derived LDHs for high-performance OER.

Bhaskar Biswas

Dr Bhaskar Biswas is presently serving as a Professor of Chemistry at the University of North Bengal, Darjeeling, India. He obtained his M.Sc. and PhD from the University of Burdwan. Prof. Biswas is a bioinspired Synthetic Chemist with vast experience in the design and development of coordination-driven functional materials and electrocatalysts for csustainable energy transitions. He received the Young Scientist Award in 2013 and the Teachers' Associateship for Research Excellence Award (TARE) in 2018 from the Science & Engineering Research Board (SERB), India. Prof. Biswas established the Laboratory for Structural Engineering & Sustainable Catalysis (LSESC) in 2022 and is presently engaged in the design and development of coordination-driven energy-efficient electrocatalysts and composite materials for the sustainable energy economy. As a Principal Investigator, he has completed a number of research projects, including a consultancy project with Hydrogen Innovation Pvt Ltd, Singapore. Prof. Biswas has published more than 150 research articles, including a few review articles and book chapters in journals of international repute. Ten (10) scholars have already been awarded their doctoral degrees, and twelve (12) scholars are pursuing their doctoral research under his supervision.

3. A brief overview of the mechanisms involved in electrocatalytic hydrogen evolution and oxygen evolution reactions in different electrolytic media

The EWS reaction (eqn (1)) involves two half-cell reactions: the HER occurring at the cathode and the OER occurring at the anode.[39]

$$\mathrm{H_2O\,(l)} \rightarrow \mathrm{H_2\,(g)} + \frac{1}{2}\mathrm{O_2\,(g)}, \quad \Delta G^\circ = +237.2\ \mathrm{kJ\ mol^{-1}}$$
$$\Delta E^\circ = 1.23\ \mathrm{V}\ \textit{vs.}\ \text{normal hydrogen electrode (NHE)} \tag{1}$$

Hydrogen evolution reaction

$$2\mathrm{H^+} + 2\mathrm{e^-} \rightarrow \mathrm{H_2}\ \text{in acid solution}$$

$$2\mathrm{H_2O} + 2\mathrm{e^-} \rightarrow \mathrm{H_2} + 2\mathrm{OH^-}\ \text{in alkaline solution}$$

Oxygen evolution reaction

$$2\mathrm{H_2O} + 4\mathrm{e^-} \rightarrow \mathrm{O_2} + 4\mathrm{H^+}\ \text{in acid solution}$$

$$4\mathrm{OH^-} + 4\mathrm{e^-} \rightarrow \mathrm{O_2} + 2\mathrm{H_2O}\ \text{in alkaline solution}$$

3.1. Hydrogen evolution reaction

The HER is a two-electron reduction of water at the cathode, requiring a theoretical potential of 0 V *vs.* RHE.[40] In practice, an additional energy input, known as the overpotential (η), is needed to overcome kinetic barriers.[41–44] The HER proceeds through different mechanistic pathways depending on the electrolyte pH, generally following the Volmer–Heyrovsky or Volmer–Tafel processes.[45–47]

In acidic media, the key descriptor of catalytic activity is the hydrogen adsorption free energy (ΔG_{H^*}) (Fig. 1(a)), which should ideally be close to zero for optimal performance (Fig. 1(b) & (c)).[48,49] In alkaline media, besides ΔG_{H^*}, the sluggish water dissociation step often becomes a kinetic bottleneck (Fig. 1(d)).[50,51]

Deciphering the precise HER mechanism on various electrocatalysts remains challenging. Nonetheless, the Tafel slope often serves as a useful indicator of the rate-determining step, offering valuable insight into the underlying reaction pathway. Fundamentally, the HER proceeds through three key steps (Fig. 1(e)).[39,52] The reaction begins with the Volmer step, where protons (H_3O^+ in acid or H_2O in base) are reduced to adsorbed H* on the catalyst surface. H_2 formation then proceeds either *via* the Heyrovsky step (electrochemical desorption) or the Tafel step (surface recombination).

Step I. Volmer reaction (~120 mV dec^{-1}): electrochemical hydrogen adsorption (eqn (2) and (3))

$$H_3O^+ + M + e^- \leftrightharpoons M\text{–}H^* + H_2O \text{ (acidic medium)} \quad (2)$$

$$H_2O + M + e^- \leftrightharpoons M\text{–}H^* + OH^- \text{(alkaline medium)} \quad (3)$$

Step II. Heyrovsky reaction (~40 mV dec^{-1}): electrochemical desorption (eqn (4) and (5))

$$H^+ + e^- + M\text{–}H^* \leftrightharpoons H_2 + M \text{ (acidic medium)} \quad (4)$$

$$H_2O + e^- + M\text{–}H^* \leftrightharpoons H_2 + OH^- + M \text{ (alkaline medium)} \quad (5)$$

Step III. Tafel reaction (~30 mV dec^{-1}): chemical desorption

$$2\ M\text{–}H^* \leftrightharpoons H_2 + 2\ M \text{ (both acidic and alkaline media)} \quad (6)$$

The Tafel slope provides mechanistic insight by identifying the rate-determining step.[3] Characteristic values are ~120 mV dec^{-1} for the Volmer step, ~40 mV dec^{-1} for the Heyrovsky step, and ~30 mV dec^{-1} for the Tafel step. Thus, analyzing the Tafel slope helps to distinguish whether hydrogen adsorption, electrochemical desorption, or recombination governs the HER kinetics on a given catalyst.

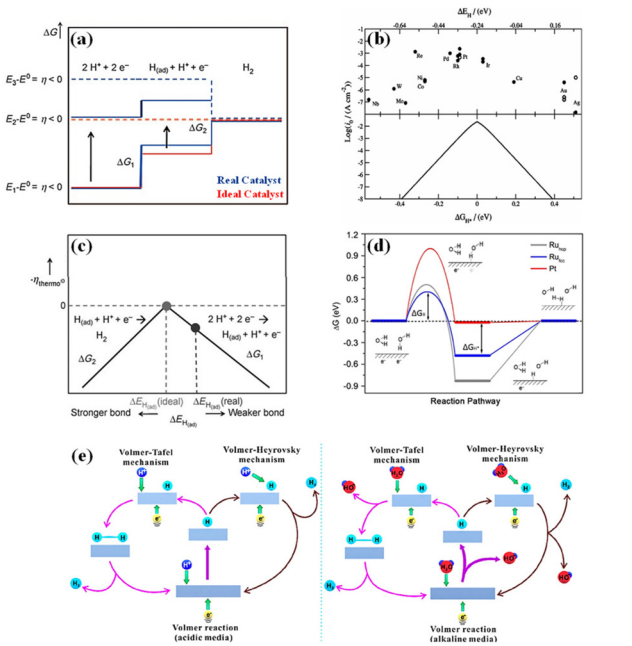

Fig. 1 (a) Plot of Gibbs free energies of reactive species and Gibbs free energies of chemisorptions of intermediates (horizontal lines) *versus* the reaction coordinate of the HER, adapted from ref. 51 with permission from Wiley,[51] copyright 2010. (b) Experimentally measured exchange current, log(i_0), for hydrogen evolution over different metal surfaces plotted as a function of the calculated hydrogen chemisorption energy per atom, ΔE_H (top axis). Adapted from ref. 53; (c) one-dimensional thermochemical volcano plot of the HER. The negative thermodynamic overpotential is plotted against the total hydrogen chemisorption energy $\Delta E_{H(ad)}$, adapted from ref. 51 with permission from Wiley,[51] copyright 2010; (d) Gibbs free energy diagram of HER on different surfaces including reactant initial state, intermediate state, final state, and an additional transition state representing water dissociation, adapted from ref. 50, with permission from American Chemical Society,[50] copyright 2016 and (e) mechanism of hydrogen evolution on the surface of an electrode in acidic (left) and alkaline (right) solutions, adapted from ref. 39 with permission from American Chemical Society,[39] copyright 2019.

3.2. Oxygen evolution reaction

Understanding the mechanisms of the OER is essential for the rational design of efficient electrocatalysts. Three main frameworks are generally proposed: the adsorbate evolution mechanism (AEM), the lattice oxygen mechanism (LOM), and the oxide pathway mechanism (OPM).

3.2.1. Adsorbate evolution mechanism (AEM). In the widely accepted AEM, the OER proceeds *via* four successive proton–electron transfer (PCET) steps involving adsorbed intermediates like OH*, O*, OO*, O_2 bound to metal active sites.[54] In alkaline media, OH^- is oxidized stepwise to form OH*, O*, and OOH*, before releasing O_2, while in acidic media the same intermediates are involved through proton-assisted pathways. The step with the highest reaction free energy defines the overpotential, ideally 1.23 eV, though in practice this ideal condition is rarely achieved because the adsorption energies of the intermediates are linearly correlated.[51] Fig. 1(c) illustrates the energetics of the real and ideal catalyst at various electrode potentials.[55]

Alkaline media

$$M^* + OH^- \rightarrow OH^* + e^- \quad (7)$$

$$OH^* + OH^* \rightarrow H_2O + O^* + e^- \quad (8)$$

$$O^* + OH^- \rightarrow OOH^* + e^- \quad (9)$$

$$OOH^* + OH^- \rightarrow M^* + O_2 + e^- \quad (10)$$

Acidic media

$$H_2O\ (l) + M^* + \rightarrow OH^* + H^+ + e^- \quad (11)$$

$$OH^* \rightarrow O^* + H^+ + e^- \quad (12)$$

$$H_2O\ (l) + O^* \rightarrow OOH^* + H^+ + e^- \quad (13)$$

$$OOH^* \rightarrow M^* + O_2\ (g) + H^+ + e^- \quad (14)$$

3.2.2. Lattice oxygen mechanism (LOM). The LOM introduces lattice oxygen participation, where surface O* couples directly with lattice oxygen atoms to form O_2 through an anionic redox process, with electrolyte oxygen replenishing vacancies to sustain structural stability.

$$O^* + O_L \rightarrow O_2\ (g) + O_V \quad (15)$$

3.2.3. Oxide pathway mechanism (OPM). By contrast, the OPM involves direct O–O radical coupling between O* and OH* without generating OOH* or creating lattice vacancies, preserving catalyst integrity but requiring strict geometric and electronic conditions.

Although AEM dominates across most transition-metal (oxy)hydroxides and MOFs due to its well-defined PCET steps, LOM and OPM provide complementary advantages such as enhanced activity or stability under demanding conditions. A cooperative interplay between these mechanisms offers a promising strategy to optimize OER efficiency and durability.

4. Factors influencing the *in situ* formation of MOF-derived LDHs for effective EWS in alkaline media

4.1. Conversion route: *in situ* synthetic methods of MOF to LDH transformation

The widely employed conventional methods for converting MOFs to LDHs, such as direct pyrolysis and *ex situ* hydrothermal treatment, are often detrimental; they typically cause morphological collapse, porosity loss, and particle aggregation due to harsh conditions, nullifying the MOF's structural advantages.[56] The *in situ* transformation of MOFs into LDHs involves a series of chemical and structural evolutions that occur under specific reaction conditions through hydrothermal or solvothermal processes, acid or alkaline etching, electrochemical activation, *etc.* during which metal nodes in the MOFs undergo partial dissolution and re-precipitation, accompanied by intercalation of hydroxide anions and other species. The organic ligands may also decompose or be replaced during this process.[57] *In situ* transformation under mild conditions enables a topotactic reaction that perfectly retains the MOF's original morphology while constructing a hierarchical structure of LDH nanostructures. In this section, we discuss various strategies involved in the *in situ* transformation of MOF into LDHs, along with their application in WS reactions.

4.1.1. Electrochemical activation. Electrochemical activation serves as a precise and controllable method for inducing the *in situ* transformation of MOFs into LDHs under ambient conditions.[58,59] This process involves applying a carefully selected electrode potential to a MOF-coated electrode immersed in an electrolyte, initiating faradaic reactions that trigger structural reorganization. This continuous electrochemical driving force facilitates a transformation, wherein the original porous MOF architecture is preserved while its internal structure is converted into an interconnected network of ultrathin LDH nanoplatelets.

When a pulsed cathodic potential is applied, the oxygen reduction reaction (ORR) generates a localized high-pH environment near the electrode surface.[60] This transient alkaline front induces hydrolysis of the metal–ligand bonds in the MOF, releasing metal cations and simultaneously supplying hydroxide ions necessary for LDH nucleation and growth.[61,62] Conversely, anodic polarization induces local acidification *via* water oxidation, which promotes the hydrolytic etching of the MOF and the release of metal ions that can subsequently precipitate as LDH under suitable pH conditions.[63] The selection of potential whether anodic or cathodic is determined by the redox stability of the MOF components and the desired electrochemical reaction pathway, often guided by cyclic voltammetry to identify optimal activation windows.[64,65] Moreover, the organic ligands released during dissociation may undergo electrochemical decomposition, forming a conductive carbon matrix that intertwines with the growing LDH, enhancing electron transfer and mechanical stability.[66] The resulting composite exhibits a hierarchical porosity that promotes efficient mass transport and exposes abundant active sites, making it particularly advantageous for applications in electrocatalysis. The distinctive design of the hybrid catalysts, achieved through electronic structure modulation and morphological control, promotes the formation and exposure of abundant active sites, thereby improving electrolyte penetration and transport.[67] Electrochemical activation aids in doping or heterostructuring that can modify the electronic structure of active sites, optimizing the d-band center and enhancing adsorption/desorption of intermediates.[68]

In this context, Liang *et al.* fabricated a composite electrode on NF by combining ZIF-67-derived Ni–Co–Se with NiFe LDHs on NF through *in situ* hydrothermal and electrodeposition techniques.[69] Electrodeposition using a solution containing Fe and Ni salts in a three-electrode setup was carried out, wherein Ni–Co–Se/NF served as the working electrode, at a constant potential of −1.0 V *vs.* Ag/AgCl for 120 seconds, resulting in the formation of **Ni–Co–Se@NiFe LDH/NF** (Fig. 2(a)). The **Ni–Co–Se@NiFe LDH** composite electrode displayed outstanding electrocatalytic activity for both, HER and OER. It required a low overpotential of just 78 mV to reach 10 mA cm^{-2} for the HER and 234 mV to reach 50 mA cm^{-2} for the OER (Fig. 2(b) & (c)). Notably, the catalyst demonstrated superior overall water-splitting performance, achieving 10 mA cm^{-2} at a low cell voltage of 1.52 V, surpassing the benchmark noble-metal-based system RuO_2/NF‖Pt–C/NF, which required 1.60

V. Additionally, the composite showed good operational stability, maintaining performance for approximately 50 hours (Fig. 2(d)).

Modifying the substrate is generally essential for developing effective electrocatalytic electrodes with significantly enhanced catalyst loading, increasing the number of active sites, and improving long-term operational stability.[70–72] On similar grounds, Gao and coworkers fabricated a **NiFe-LDH/Ni-BDC/NF** electrode, wherein a Ni-BDC MOF nanosheet layer was grown *in situ* on NF, followed by electrodeposition of NiFe-LDH (Fig. 3(a)).[73] The loading of NiFe-LDH was precisely controlled by monitoring the total charge passed (3 C, 4.5 C, and 6 C) during electrodeposition at −0.76 V *vs.* NHE. Since the amount of deposited material is directly proportional to the charge, this approach enabled systematic tuning of catalyst thickness and active site density. The Ni-BDC layer improved hydrophilicity and conductivity, enhancing catalyst loading and electron transfer. The optimized electrode exhibited remarkable OER activity, needing just 223 mV overpotential to reach 100 mA cm^{-2} (Fig. 3(b)), along with a low Tafel slope of 33.1 mV dec^{-1}, and sustained stable performance for more than 10 days in 1 M KOH (Fig. 3(c)). The superior activity and durability for about 10 days were attributed to the conductive, hydrophilic Ni-BDC support and strong interfacial contact.

Despite its promise, electrochemical activation for MOF-to-LDH conversion faces significant challenges, including sensitivity to parameters that complicate reproducibility, an incomplete mechanistic understanding of the transformation pathway, and difficulties in scaling beyond lab-scale electrodes due to substrate dependency and limited mass loadings.

4.1.2. Alkaline treatment. In this method, selective etching of the MOF under alkaline conditions occurs, followed by recrystallization into LDH nanosheets. Generally, the MOF precursor is immersed in aqueous NaOH or KOH solution at room temperature or mildly elevated temperatures of ~40–80 °C. The hydroxide ions hydrolyze the organic ligands, leading to the collapse of the framework and ultimately liberating the metal ions from the MOF structure. These released metal ions then re-nucleate and recrystallize as LDHs, often forming ultrathin nanosheets or porous/hollow nanostructures.[12,18,74] The interlayer anions like CO_3^{2-} or NO_3^- and water molecules facilitate layered stacking, forming the LDH structure. The involvement of ionic rearrangement and localized dissolution–reprecipitation is particularly advantageous due to its simplicity, low energy requirement, and ability to produce high surface area 2D LDH structures. Enhanced exposure of active sites, efficient mass and ion transport, and a large electrochemically active surface area collectively contribute to the development of a highly effective electrocatalyst.

Pertaining to this, Zhai *et al.* reported the partial transformation of FeNi-MOF-74 in 0.25 M KOH at 75 °C for 6 hours to obtain **Fe–Ni LDH/MOF-b2** (Fig. 4(a)).[75] Ultra-thin ~5 nm LDH nanosheets grew *in situ* on the MOF surface, forming a hierarchical structure. Upon increasing the alkali concentration, the FeNi-MOF-74 precursor underwent structural transformation into **Fe–Ni LDH/MOF-b2**, which retained the original MOF-74 morphology while integrating ultra-thin 2D LDH structures. A distinct hollow architecture was observed in **Fe–Ni LDH/MOF-b2**, featuring vertically aligned LDH nanosheet arrays embedded within a hollow, columnar MOF framework

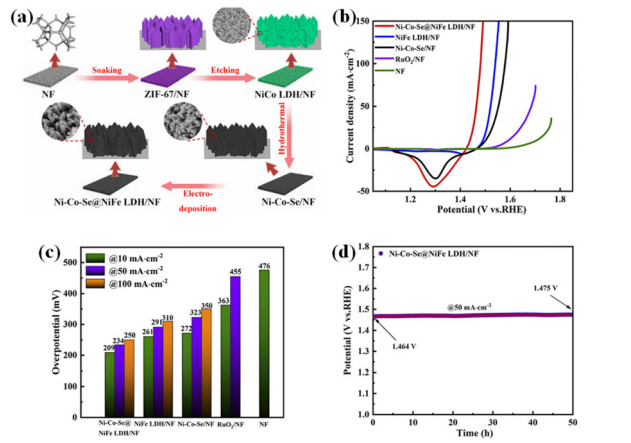

Fig. 2 (a) Schematic representation of the synthesis route for the **Ni–Co–Se@NiFe LDH/NF** composite electrode; (b) LSV profiles comparing the electrocatalytic performance of **Ni–Co–Se@NiFe LDH/NF** with NiFe LDH/NF, Ni–Co–Se/NF, RuO_2/NF, and bare NF; (c) bar graph depicting the overpotentials required by the different electrodes **(Ni–Co–Se@NiFe LDH/NF**, NiFe LDH/NF, Ni–Co–Se/NF, RuO_2/NF, and NF) to achieve current densities of 10, 50, and 100 mA cm^{-2} and (d) long-term stability assessment of **Ni–Co–Se@NiFe LDH/NF** conducted at a constant current density of 10 mA cm^{-2}, adapted from ref. 69 with permission from Royal Society of Chemistry,[69] copyright 2024.

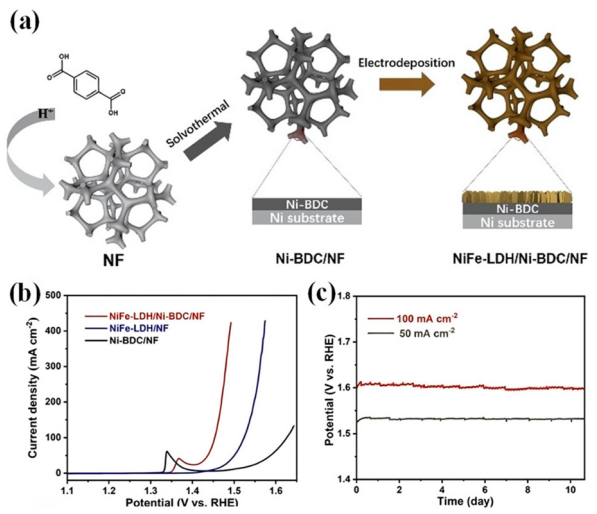

Fig. 3 (a) Schematic illustration of the synthesis procedure for the **NiFe-LDH/Ni-BDC/NF** electrode; (b) LSV curves comparing the electrocatalytic performance of **NiFe-LDH/Ni-BDC/NF** with that of NiFe-LDH/NF and Ni-BDC/NF; and (c) chronopotentiometric stability test of the **NiFe-LDH/Ni-BDC/NF** electrode conducted at constant current densities of 50 mA cm^{-2} and 100 mA cm^{-2}, adapted from ref. 73 with permission from Wiley,[73] copyright 2024.

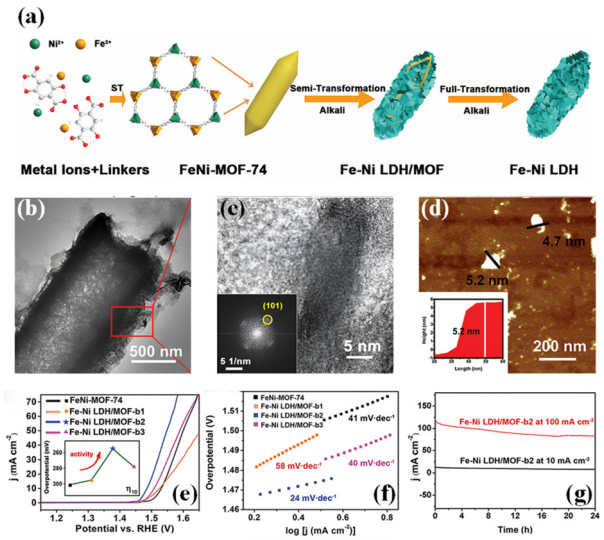

Fig. 4 (a) Schematic illustration of the *in situ* semi-transformation strategy used to synthesize hierarchical Fe–Ni LDH/MOF hybrid structures; (b) TEM image of the **Fe–Ni LDH/MOF-b2** composite, showing its nanoscale morphology; (c) HRTEM image along with the corresponding fast Fourier transform (FFT) pattern of **Fe–Ni LDH/MOF-b2**, confirming its crystallinity; (d) AFM image highlighting the presence of ultrathin LDH nanosheets on the surface of the **Fe–Ni LDH/MOF-b2 hybrid**; (e) LSV curves comparing FeNi-MOF-74 and **Fe–Ni LDH/MOF-b1, b2, and b3**, where b1, b2, and b3 represent materials treated with 0.10 M, 0.25 M, and 0.50 M KOH, respectively, at 75 °C. (f) Corresponding Tafel plots illustrating the OER kinetics of FeNi-MOF-74 and **Fe–Ni LDH/MOF-b1, b2, and b3**. (g) Long-term electrochemical stability test of **Fe–Ni LDH/MOF-b2** conducted over 24 hours, adapted from ref. 75 with permission from Royal Society of Chemistry,[75] copyright 2020.

(Fig. 4(b)). HRTEM images of the ultrathin LDH nanosheets revealed clear lattice fringes with an interplanar distance of 0.2 nm, corresponding to the (101) plane of Fe–Ni LDHs (Fig. 4(c)). AFM data confirmed that the nanosheet thickness was approximately 5 nm (Fig. 4(d)). This hybrid architecture exhibited excellent OER activity, with a low overpotential of 255 mV at a current density of 10 mA cm^{-2} and a Tafel slope of just 24 mV dec^{-1} (Fig. 4(e) & (f)). The superior activity and stability for 24 h was attributed to the increased surface area, improved charge transport, and strong redox synergy between Ni^{3+}/Ni^{2+} and Fe^{3+}/Fe^{2+} couples (Fig. 4(g)).

Although alkaline transformation of MOFs into LDHs is simple and versatile, it faces several limitations in terms of the mechanistic understanding of etching and recrystallization dynamics, with unclear kinetic pathways and intermediate species. It is still unclear whether the transformation occurs *via* complete dissolution or partial rearrangement of the precursor. Morphology control is unpredictable, as the influence of MOF facets, defect density, and etching rate is not well defined, leading to inconsistent architectures across different precursors. Metal ion leaching often results in inhomogeneous compositions and phase impurities, especially in multimetallic systems. Additionally, some structures exhibit low electrochemical surface area (ECSA) due to incomplete active site exposure or nanosheet restacking. Scalability is constrained by substrate compatibility, as alkaline treatments are mostly limited to metal foils and may not suit flexible or inert supports. Critically, most studies rely on *ex situ* analysis, with limited use of *operando* techniques to elucidate real-time transformation and active phase evolution.

4.2. Hydrothermal/solvothermal treatment

Hydrothermal treatment is the most common approach for the *in situ* transformation of MOFs into LDHs. Under hydrothermal conditions, the metal centres are partially leached and then reassembled with hydroxide ions to form LDH structures. The morphology of the resulting LDHs can be controlled by adjusting parameters such as temperature, time, precursor concentration, and pH.

The **NiFe-LDH/MOF** heterostructure was prepared using a Ni-MOF as the template and grown with NiFe-LDH through a straightforward two-step hydrothermal method (Fig. 5(a)).[76] The hybrid structure preserved the uniform leaf-like morphology characteristic of the original Ni-MOF, but its nanosheet surface became noticeably rougher, which facilitated greater exposure of active sites. HRTEM and selected area electron diffraction (SAED) analyses further validated the presence of well-defined crystalline facets corresponding to NiFe-LDH (Fig. 5(b)). Further structural insight was gained *via* HAADF-STEM imaging, which revealed a high density of lattice defects responsible for the material's intrinsic catalytic activity (Fig. 5(c)). The **NiFe-LDH/MOF** hybrid catalyst exhibited outstanding OER activity, requiring only 208 mV and 275 mV overpotentials to reach current densities of 20 mA cm^{-2} and 100 mA cm^{-2}, respectively, in 1 M KOH (Fig. 5(d)). In seawater electrolysis, it maintained comparable performance, with overpotentials of just 235 mV and 307 mV at the same current densities. Furthermore, the catalyst demonstrated exceptional long-term durability, continuously operating at 20 mA cm^{-2} for 100 hours in both freshwater and seawater, surpassing the stability and activity of commercial RuO_2.

Similarly, Dong *et al.* reported **BDC@NiFe-LDH** through *in situ* surface-conversion of Ni-BDC derived *via* a solvothermal method (Fig. 6(a)). The Ni-BDC precursor surface reacted with OH^- ions in an alkaline environment, disrupting the original MOF structure and initiating the formation of LDH nanosheets.[77] TEM imaging revealed a well-organized, layered nanosheet morphology with size ranging from 5 to 60 nm of the **Ni-BDC@NiFe-LDH** (Fig. 6(b)). High-magnification TEM further revealed that the nanosheets retained elements of the Ni-BDC framework, a structural feature that facilitates enhanced electron transport and contributed to improved catalytic activity. Additionally, the HRTEM image shows lattice fringes with an interplanar spacing of 0.24 nm, corresponding to the (110) plane of **Ni-BDC@NiFe-LDH** (Fig. 6(c)). Nonetheless, **Ni-BDC@NiFe-LDH** exhibited OER performance with a low overpotential of 272 mV at 10 mA cm^{-2} (Fig. 6(d)) and a small Tafel slope of 45 mV dec^{-1}, and stability over 30 hours. This enhanced activity was attributed to the increased number of accessible metal active sites and the

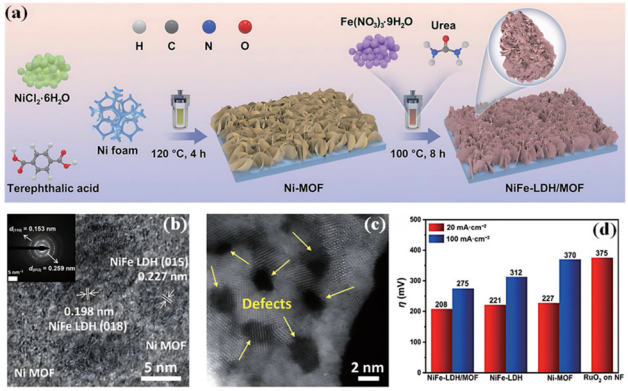

Fig. 5 (a) Schematic representation of the fabrication process for **NiFe-LDH/MOF** nanosheet arrays grown on a NF substrate; (b) TEM images of the **NiFe-LDH/MOF** nanosheets, with the inset showing the corresponding SAED patterns;(c) HRTEM images highlighting the presence of structural defects within the **NiFe-LDH/MOF** nanosheets. (d) Bar graph illustrating the overpotentials required to reach 20 and 100 mA cm^{-2}, derived from the polarization curves for the OER, adapted from ref. 76 with permission from Springer Nature,[76] copyright 2023.

improved electron transport pathways resulting from the formation of the ultra-thin layered structure during the conversion process.

The templating approach effectively produces hollow nanostructures but often involves complex steps like surface modification and toxic etching, resulting in low reproducibility, high costs, and poor uniformity. It also limits homogeneous incorporation of functional species, leading to surface agglomeration and pore blockage. Yilmaz *et al.* reported hydrothermal synthesis of **ZIF-67-C**-derived surface-active hollow frameworks bearing hollow rhombic dodecahedra **NiCo-LDH**, followed by sulfurization of NiCo-LDHs, yielding a **NiCo-LDH/Co_9S_8** hybrid (Fig. 7(a)).[17] SEM images showed that annealed ZIF-67 (**ZIF-67-C**) retained its original morphology with inward wall contraction due to ligand cross-linking (Fig. 7(b)). The derived **NiCo-LDH (C/LDH)** preserved the rhombic dodecahedral shape (Fig. 7(c)), which was maintained after sulfurization into the **NiCo-LDH/Co_9S_8** hybrid **(C/LDH/S)**; the SEM and its inset (Fig. 7(d)) confirmed the polyhedral form of **C/LDH/S**. TEM images revealed that **C/LDH** featured interconnected nanosheets forming a hollow interior (Fig. 7(e)–(g)). Similarly, elemental mapping using EDX confirmed the uniform presence of Ni, Co, O, S, and C (Fig. 7(h)). The hollow MOF-derived materials were tested for HER in 1.0 M KOH using LSV. Among various substrates tested **C/LDH/S** showed vigorous H_2 bubbling, at a low onset potential of 47 mV, and an overpotential of 142 mV at 10 mA cm^{-2} (Fig. 7(i)). It also exhibited a Tafel slope of 62 mV dec^{-1}, indicating fast HER kinetics. Embedding Co_9S_8 within LDH interlayers enhanced the interfacial contact, structural stability, redox activity, and conductivity, resulting in superior HER.

Similarly, Pal *et al.* synthesized ultrathin 2D NiCo-LDH nanosheet arrays *via in situ* growth on the surface of NH_2-UiO-66 octahedrons, using 2-methylimidazole as a precursor (Fig. 8(a)). This cost-effective and straightforward strategy produced a catalyst highly efficient for electrocatalytic OER, HER, and overall water splitting under ambient conditions.[78] Owing to its engineered interfacial structure, the **NiCo-LDH@NH_2-UiO-66** catalyst exhibited remarkable water-splitting performance, achieving a current density of 10 mA cm^{-2} at 1.65 V in alkaline electrolyte, along with excellent long-term durability (Fig. 8(b) & (c)).

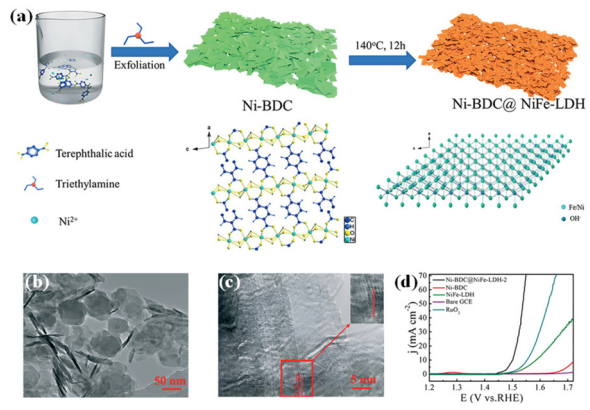

Fig. 6 (a) Schematic illustration of the synthesis process of **Ni-BDC@NiFe-LDH**; (b) TEM image of **Ni-BDC@NiFe-LDH**; (c) HRTEM images showing lattice fringes of **Ni-BDC@NiFe-LDH**; (d) OER polarization curves of GCE, Ni-BDC, NiFe-LDH, RuO_2, and **Ni-BDC@NiFe-LDH**, adapted from ref. 77 with permission from Royal Society of Chemistry,[77] copyright 2021.

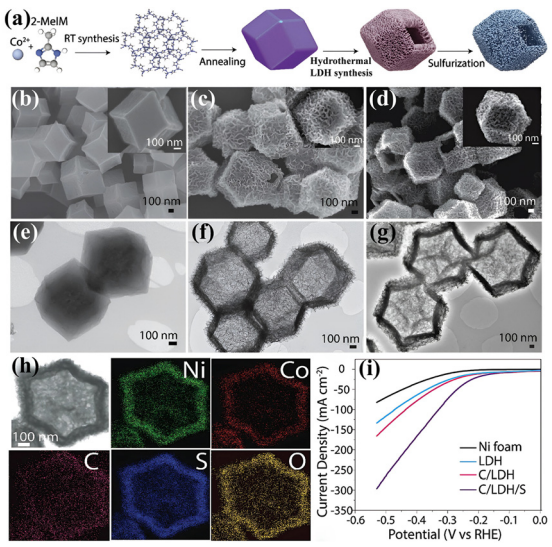

Fig. 7 (a) Schematic illustration of the synthesis process of hollow **NiCo-LDH/Co_9S_8** hybrid; SEM images of (b) **ZIF-67-C**, (c) **C/LDH**, and (d) **C/LDH/S** polyhedrons; TEM images of (e) **ZIF-67-C**, (f) **C/LDH**, and (g) **C/LDH/S** polyhedrons; (h) elemental mapping of C/LDH/S showing the distribution of Ni, Co, C, O, and S; (i) HER polarization curves of NF, **LDH, C/LDH, and C/LDH/S**, adapted from ref. 17 with permission from Wiley,[17] copyright 2017.

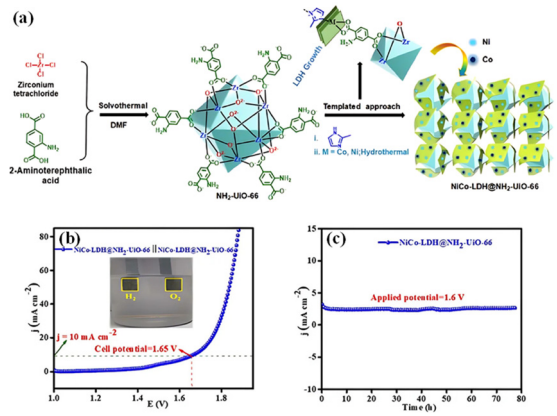

Fig. 8 (a) Schematic diagram for the synthesis of **NiCo-LDH@NH_2-UiO-66** heterostructure, (b) LSV polarization curves of the **NiCo-LDH@NH_2-UiO-66** hybrid towards EWS; (c) long-term static stability test of the **NiCo LDH@NH_2-UiO-66** heterostructure for 78 h at 1.6 V, adapted from ref. 78 with permission from Royal Society of Chemistry,[78] copyright 2023.

In summary, solvothermal treatments provide effective pathways for transforming MOFs into LDHs with tailored morphologies, controlled crystallinity, and enhanced catalytic performance. These methods facilitate defect engineering, metal site dispersion, and hierarchical structuring beneficial for electrocatalysis. However, critical challenges remain, including limited mechanistic understanding of MOF degradation and LDH nucleation, lack of real-time insights into phase evolution, and dependency on empirical parameter tuning. Additionally, issues such as multistep processing, toxic reagents, substrate compatibility, and high energy demand impact scalability and sustainability.

To address the limitations of these synthetic methods, future research must prioritize the use of advanced *in situ* and *operando* characterization techniques such as liquid-cell TEM and XAS to elucidate real-time transformation mechanisms at the atomic scale. Furthermore, expanding the approach to novel MOF architectures and deliberately engineering the electrochemical process for specific applications such as creating strained active sites for electrocatalysis will be crucial to fully realize the potential of this sophisticated synthesis strategy.

4.3. External additives/templates: 2D supports of graphene, MXene, CNTs

Hybrid structures of MOF-derived LDHs with 2D materials such as MXenes, graphene, reduced graphene oxide (rGO), or graphene quantum dots (GQDs) represent a powerful design strategy to boost electrocatalytic activity through synergistic structural and electronic effects.[79,80] The MOF-to-LDH transformation produces high-surface-area, defect-rich architectures, while conductive 2D supports provide rapid charge-transport channels, prevent LDH restacking, and improve mechanical stability during gas evolution. Strong interfacial coupling through covalent linkages like Ni–C, Fe–C, M–O–C or electrostatic interactions modulates the d-band center, optimizes adsorption energies of reaction intermediates, and accelerates reaction kinetics for both HER and OER.[81] Improving the intrinsic activity and unveiling the true active sites of transition metal-based electrocatalysts remains a significant challenge.

Han *et al.* developed an effective partial *in situ* transformation (PTS) strategy to convert a NiFe-MOF-74 precursor into a NiFe-LDH@MOF composite.[82] Subsequent F^- coordination induced a rapid structural reconstruction of F-doped NiFe-LDH@MOF on MXene (Fd-PTS-NLM) during overall water splitting. Mechanistic studies revealed that tuning the electron diffusion process can regulate the electron transfer rate, thereby lowering the energy barriers of catalytic reactions. The combined effects of F-doping and PTS modified the d-band center, markedly enhancing the bifunctional catalytic activity. *In situ* Raman spectroscopy confirmed that metal hydroxyl oxides serve as the actual active species for the OER. The catalyst demonstrated excellent electrochemical performance, requiring 150 mV for HER and 171 mV for OER at 10 mA cm^{-2}.

Similarly, Hu and coworkers used multifunctional Ti_3C_2 MXene as a support, and applying an etching–coprecipitation treatment to the MOF precursor the resulting CoFe MLDH/Ti_3C_2 hybrid achieved exceptional OER activity, with overpotentials of 170 mV and 238 mV at current densities of 10 and 100 mA cm^{-2}, respectively.[83] Experimental measurements combined with theoretical calculations confirmed that strong electronic coupling between CoFe MLDH and Ti_3C_2 MXene optimizes the binding strength of OER intermediates. This work provides a pathway for designing highly active MOF-based electrocatalysts and improving the intrinsic activity of (oxy)hydroxide catalysts.

Fan *et al.* demonstrated that integrating MOF-derived Ni–Co sulfide with $Ti_3C_2T_x$ MXene produced a hierarchical hybrid catalyst with significantly improved water oxidation performance (Fig. 9(a)).[21] The porous structure and intimate interfacial coupling between NiCoS and the conductive MXene sheets

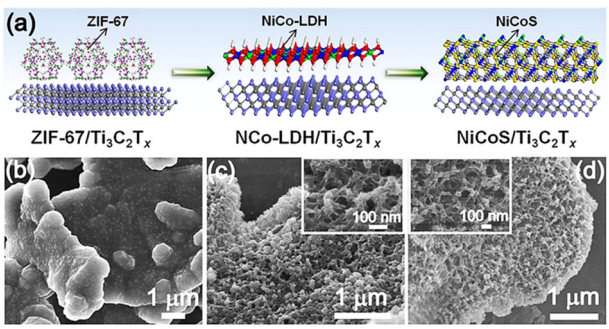

Fig. 9 (a) Scheme of the preparation process of NiCoS/$Ti_3C_2T_x$. SEM images of (b) ZIF-67/$Ti_3C_2T_x$, (c) NiCo-LDH/$Ti_3C_2T_x$, and (d) NiCoS/$Ti_3C_2T_x$. Inset: the high-magnification SEM images of the samples, adapted from ref. 21 with permission from American Chemical Society,[21] copyright 2018.

increased the accessible surface area, accelerate charge-transfer kinetics, and expose abundant active sites (Fig. 9(b)–(d)). As a result, the NiCoS/$Ti_3C_2T_x$ hybrid exhibited superior electrocatalytic activity toward the OER compared with its individual components, underscoring the critical role played by MXene in optimizing the structure–activity relationship of MOF-derived materials for efficient OER. $Ti_3C_2T_x$ MXene served as a conductive 2D scaffold for uniform NiCo-LDH growth, preventing aggregation and forming a porous structure with abundant active sites. It was established that during the OER, MOF-derived NiCoS transformed *in situ* into NiCoOOH, confirmed through XPS studies of the catalyst before and after electrocatalysis.

Beyond MXenes, carbon-based supports also play a key role, *via* interface engineering to overcome the intrinsically poor electron transport of LDHs by regulating electron distribution through the incorporation of secondary components. In this context, Yang *et al.* fabricated a hierarchical hybrid CoFe-LDH@NPC by anchoring CoFe-LDH nanosheets onto layered N-doped porous carbon (NPC).[84] The resulting CoFe-LDH@NPC exhibited excellent bifunctional electrocatalytic activity, requiring overpotentials of only 280 mV for the OER and 100 mV for the HER. In overall water splitting, the catalyst delivered a stable current density of 10 mA cm^{-2} at 1.61 V for 60 hours. The theoretical analysis revealed that the intimate interface between NPC and CoFe-LDH formed electron-deficient and electron-rich regions, facilitated charge transfer and modulated the adsorption of key intermediates, thereby enhancing WS. Electrochemical evaluation further confirmed this effect wherein, at 10 mA cm^{-2}, CoFe-LDH@NPC showed an OER overpotential of 280 mV, significantly lower than that of RuO_2 (380 mV). Additionally, its Tafel slope 93.3 mV dec^{-1} was much smaller than those of other benchmark catalysts, underscoring faster reaction kinetics and superior catalytic performance.

Further, Rinawati *et al.* developed a hybrid catalyst comprising dual boron- and nitrogen-doped graphene quantum dots (B,N-GQDs) integrated into NiFe-LDH derived from NiFe-MOF-74 to address the intrinsic conductivity and active-site limitations of LDHs.[22] The *in situ* incorporation of heteroatom-doped GQDs during MOF synthesis, followed by spontaneous transformation to LDH in alkaline media, preserved the MOF-derived porous framework while introducing abundant defect sites and strong Ni–C/Fe–C/Ni/Fe–O–C linkages. Dual heteroatom doping synergistically modulated the d-band center, optimized Ni/Fe oxidation states, and enhanced charge transfer, as confirmed by XPS and soft-XAS analyses. The resulting B, N-GQDs/MOF-derived NiFe-LDH exhibited outstanding OER activity in alkaline electrolyte, delivering an overpotential of 251 mV at 100 mA cm^{-2}, a low Tafel slope of 34.9 mV dec^{-1}, high electrochemically active surface area, and excellent durability over 24 h, surpassing pristine NiFe-LDH, undoped or single-doped analogues, and even commercial IrO_2. This work highlighted the effectiveness of synergistic heteroatom doping combined with MOF-derived architectures in maximizing active-site exposure and tailoring the electronic structure for high-performance, earth-abundant electrocatalysts.

Collectively, these studies demonstrate that interface engineering in MOF-derived LDH/2D hybrids simultaneously addresses conductivity, active-site accessibility, and structural stability. Strategies such as heteroatom doping, conductive 2D supports, and strong interfacial coupling consistently emerge as key design principles for advancing high-performance, Earth-abundant electrocatalysts for water splitting. Despite these advances, critical gaps remain: the true nature of active sites under operating conditions is poorly understood due to limited *operando* studies; interfacial charge-transfer rates are rarely quantified; benchmarking across studies lacks standardization; and durability at industrially relevant current densities is scarcely reported.

5. Reaction medium: role played by electrolytes

While ongoing research on efficient electrocatalyst design and application is progressing, recognizing electrolyte effects remains crucial for sustainable hydrogen production *via* renewable-powered water electrolysis. Electrolytes play a pivotal role in electrocatalytic water splitting far beyond serving as reactant reservoirs. They directly control ionic conductivity, thereby influencing ohmic resistance and overall energy efficiency. By judiciously tailoring electrolyte environments, it becomes possible to balance activity, stability, and cost, thereby bridging the gap between laboratory demonstrations and scalable, device-integrated hydrogen technologies.[85]

In acidic media, hydronium ions (H_3O^+) act as direct proton sources, enabling rapid HER on Pt-group metals (PGMs).[86–88] Conversely, in alkaline solutions, the rate is limited by sluggish water dissociation, resulting in up to two orders of magnitude lower activity on Pt compared with acidic conditions.[89,90] Neutral and near-neutral pH conditions introduce mass transport limitations and local pH gradients at the electrode surface, often necessitating buffered electrolytes, *e.g.*, phosphate, carbonate, borate, to maintain HER rates comparable to strongly acidic or alkaline environments.[91] Beyond conventional liquid electrolytes, alternative systems such as solid electrolytes and ionic liquids (ILs) have also been investigated for HER applications. Owing to their unique features including low vapor pressure, high ionic conductivity, and structural tunability, ILs have shown promise in enhancing HER performance.[86] For instance, Amaral *et al.* demonstrated that incorporating the ionic liquid [Emim][$MeSO_3$] (Emim = ethymethyl imidazole) into an 8 M KOH electrolyte improved HER activity on a Pt cathode. Moreover, the activation energy in IL-modified KOH was reduced to 10 kJ mol^{-1} compared with the IL-free system.[92] Thus, ionic liquids can provide an avenue for tuning interfacial kinetics beyond conventional aqueous systems.

Apparently inactive components in electrolytes too have a significant impact on catalytic performance. Specifically, alkali metal cations in high-pH aqueous electrolytes can cause notable changes in the reaction turnover frequency through noncovalent interactions with water molecules, spectator ions,

surface adsorbates, and electrified interfaces. Alkali metal cations like Li^+, Na^+, K^+, Cs^+ modify interfacial water structure, intermediate adsorption, and hydrogen binding energies. Li^+ ions can either enhance or suppress the HER depending on the metal substrate: they improve the HER on Au, Fe, and Ni, while suppressing activity on Pt, Pd, and Ir. This tunability arises from altered M–H bond strengths and interfacial OH^- dynamics.[93] However, the use of Li^+-containing aqueous electrolytes is not yet commercialized, making HER suppression necessary in certain processes. Similarly, anions such as perchlorate (ClO_4^-), chloride (Cl^-), or bis(trifluoromethanesulfonyl)imide ($TFSI^-$), further modulate kinetics by participating in co-adsorption or by forming passivating surface films like LiF from LiTFSI electrolytes. Tailored cation selection Li^+ *vs.* K^+/Cs^+ has shown promise in accelerating interfacial water activation, pointing to practical electrolyte formulations that could boost efficiency in large-scale systems. For example, coupling $Ni(OH)_2$ with Pt and using alkali metal ions-rich electrolytes enhances HER kinetics by balancing hydrogen adsorption and hydroxyl desorption, offering a scalable route toward low-cost alkaline devices.[80]

For next-generation energy devices such as water electrolyzers, regenerative fuel cells, and metal–air batteries, electrolyte optimization must be pursued in tandem with catalyst design to achieve commercially viable performance. Parameters such as pH, ionic species, concentration, and functional additives profoundly influence not only thermodynamics and kinetics but also long-term durability. In future energy infrastructures, electrolytes shall no longer be passive components but active design parameters enabling high-efficiency PEM (proton exchange membrane), AEMEL (Anion Exchange Membrane Electrolyzer), and solar-driven electrolyzers, as well as multifunctional energy storage devices that bridge hydrogen production with batteries and fuel cells. Alkaline media enables the deployment of earth-abundant catalysts such as MOF-derived LDHs without severe dissolution. However, the sluggish water dissociation step limits HER activity. For MOF-derived LDHs, the electrolyte can dictate phase stability, tune intermediate adsorption, and sustain operation under industrially relevant conditions. Yet, systematic investigations remain scarce, particularly under *operando* conditions that capture electrolyte–catalyst interactions at dynamic interfaces. Bridging this gap will be crucial for translating MOF-derived LDHs into robust electrolyzers and integrated hydrogen energy platforms.

In this context, for MOF-derived LDHs, synergy with optimized electrolytes holds a huge area of exploration involving:

i. Enhancement of intrinsic activity by modulating the adsorption energy of reaction intermediates through ion–surface interactions.

ii. Accelerating reaction pathways *via* selective stabilization of key intermediates like –OOH in the OER and promotion of water dissociation in the HER.

iii. Stabilizing active oxyhydroxide phases generated under OER conditions, preventing their reduction or amorphization.

iv. Limited *operando* studies on cation/anion restructuring of interfacial water under high current need more attention.

v. Coupling electrolyte optimization with *in situ* phase evolution of MOF-derived LDHs is underexplored.

vi. Stability of ionic-liquid or water-in-salt electrolytes at device scale.

vii. Sustained performance at industrially relevant current densities (>200–500 mA cm^{-2}) by minimizing mass-transport limitations and controlling local temperature rise.

Advancement of MOF-derived LDH electrocatalysts relies on co-engineering the catalyst–electrolyte interface, where the catalyst's structural and electronic attributes are purposefully matched to an electrolyte environment that maximizes activity, selectivity, and operational lifespan.

To contextualize the heterojunction catalysts in electrocatalytic water splitting, we have compiled a comparative table (Table 1) that benchmarks MOF-derived LDH-heterostructures against other reported heterojunction systems. The table summarizes synthesis routes, HER/OER overpotentials, Tafel slopes, durability metrics, and references, enabling side-by-side evaluation of framework-to-hydroxide catalysts relative to current state-of-the-art materials.

6. The utilization and importance of *in situ*/*operando* characterization

In situ/*operando* characterization plays a pivotal role in unveiling the dynamic structural and electronic transformations of electrocatalysts under actual working conditions. Although *ex situ* characterization techniques can reveal the phase and microstructural evolution of pre-catalysts before and after catalytic reactions, they fail to capture transient intermediates and offer limited insight into the real-time reconstruction mechanisms.[110] *In situ*/*operando* studies bridge the gap between precursor design and catalytic performance, offering mechanistic insights into how metal centers, coordination environments, and redox dynamics evolve under applied potential.[111] Combining *ex situ* characterization with *in situ*/*operando* techniques involving Raman spectroscopy, ATR-FTIR, XPS, EIS, TEM, and XAS allows researchers to directly observe the dynamic evolution of catalysts, closing the knowledge gap between static, pre- and post-catalyst states.[112–114] There are reports that underline the real-time picture of *in situ* transformation of MOFs as precursors into active catalytic entities during electrochemical process.[115] Thus, investigating the transformation of MOF-derived LDHs into catalytically active species during electrochemical water splitting is essential for uncovering the true origin of catalytic activity. Understanding these processes helps design structurally resilient electrocatalysts for sustained operation at industrial current densities.

6.1. *Operando* characterization for structural transformation of MOFs into LDHs

There are reports that use *in situ* NMR, XAS, IR, UV–vis spectroscopy, and LCTEM to monitor nucleation and growth of MOFs during synthesis and electrochemical conditions.[13,28,30,116–119] Some researchers have also reported the application of these

Table 1 Comparison table of MOF-derived LDHs with other heterojunction catalysts for electrocatalytic water splitting in 1 M KOH

Catalyst	Template	Synthesis method	HER η@ 10mA cm^{-2} (mV)	OER η@ 10 mA cm^{-2} (mV)	Tafel slope (HER/OER) mV dec^{-1}	Stability@ 10 mA cm^{-2} Ref.
MOF-derived LDH: without support						
Co-LDH[94]	ZIF-67	Ultrasonic synthesis, 30 min at room temperature	—	300	110	Nearly 3 h
NiFe-LDH[95]	NiFe-MOF-74	1. Hydrothermal synthesis of NiFe-MOF-74, 120 °C, 24 h 2. Hydrothermal treatment of NiFe-MOF-74 at various reaction temperature of immersion process at 25, 120, and 180 °C	—	299	48.7	Over 24 h
MOF-derived LDH heterojunctions (metal foams, MXenes)						
Co,V-FeNi-LDHs/NF[96]	ZIF-67	One-step hydrothermal method to transform ZIF-67 with various metal dopants	180	244	121.5 (HER) 58 (OER)	60 h
CoFe-LDH/Ti_3C_2 on NF[97]	ZIF-67	1. Deposition of ZIF-67 on Ti_3C_2/NF 2. Etching and doping of deposited ZIF-67/Ti_3C_2/NF at 120 °C	—	170	31.5	Nearly 50 h
CuO@CoZn-LDH on CuF (copper foam)[98]	CoZn-ZIF	1. Different Co/Zn ratios were used to obtain Cu$(OH)_2$@ZIF/CF *via* electrostatic interaction and constant stirring 2. Cu$(OH)_2$@ZIF/CF was immersed in salt solutions and subjected to hydrothermal treatment at 120 °C for 1.5 h	124	194	98.5 (HER) 78.3 (OER)	Over 48 h
EE-NiFe-LDH on NF[61]	NiFe-BDC-MOF	*In situ* electrochemical transformation of NiFe-BDC MOF NS	—	205	41.8	24 h
Ni-MOF/LDH on NF[99]	Ni-MOF/Ox-MOF	1. Preparation of Ni-MOF/Ox-MOF heterostructures on the Ni foam at 120 °C, 4 h 2. Alkaline treatment of Ni-MOF/Ox-MOF using 1 M KOH	—	220	36	20 h
MIL-101@NiFe-LDH[100]	MIL-101@Ox-MOF	1. Synthesis of MIL-101 on NF *via* hydrothermal method, 110, 20 h 2. Synthesis of MIL-101@OX-MOF on NF at room temperature 3. Synthesis of MIL-101@NiFe-LDH on NF *via* alkaline etching at ambient conditions	—	215	55.1	24 h
Ni–Fe–Ce-LDH[101]	MIL-88A	1. Ce0doped-MIL-88 A was obtained through hydrothermal synthesis 2. Chemical etching led to the formation of Ni–Fe–Ce-LDH microcapsules	—	242	34	24 h
NiFe-LDH@Fe-MOF/IF(iron foam)[102]	Fe-MOF	1. Hydrothermal synthesis of Fe-MOF/IF, 120 °C for 12 h 2. Second hydrothermal synthesis to obtain NiFe-LDH@Fe-MOF/IF-2@150 °C for 6 h	—	183	38.9	20 h
MOF-derived heterojunctions and other heterojunctions: oxides, sulphides, carbides, selenides, phosphides supported on metal foams, CC, MXenes						
$CoSe_2$@CNC NAs on CC[103]	ZIF-L-67	Hydrothermal treatment at 80 °C for 2 h; annealing at 400 °C for 2 h in Se vapor under Ar atmosphere	84	—	38	Over 72 h
NiCoSe@NF[104]	ZIF-67	1. Ion-exchange reaction using ZIF-67/NF to obtain NiCo LDH@NF at 90 °C, 2 h 2. Hydrothermal treatment of NiCo LDH@NF with Se powder at 180 °C, 12 h	170	278	82.3 (HER) 92 (OER)	Over 48 h
MoCoNiS on NF[105]	ZIF-67	1. MoCo-LDH/NF was obtained from Co-MOF/NF after reaction for 15 min at 85 °C 2. Solvothermal synthesis at 140 °C,4 h	—	151	44.7	Over 10 h
NiCoZnP/NC on CC (carbon cloth)[106]	Co, Zn-MOF	1. Room temperature synthesis of precursors	74	228	47.51 (HER)	45 h

Table 1 *(Contd.)*

Catalyst	Template	Synthesis method	HER η@ 10mA cm^{-2} (mV)	OER η@ 10 mA cm^{-2} (mV)	Tafel slope (HER/OER) mV dec^{-1}	Stability@ 10 mA cm^{-2} Ref.
$FeN_{0.023}/Mo_2C/C$ heterostructure[107]	Coprecipitation of metal salts	2. Pyrolysis at 350 °C for 2 h@10 °C min^{-1} Pyrolysis, N_2 at 2 °C min^{-1} ramp rate for 3 h@800 °C	76	227	60.12 (OER) 65.2 (HER)	10 h
NiCoP/C[108]	ZIF-67	1. Etching ZIF-67 with Ni-salt at room temperature 2. Phosphidation with NaH_2PO_2	—	330	73.8 (OER) 96	Over 10 h
Ni_2P/FeP@NPC (N,P-doped-carbon-encapsulated nanorods)[109]	(Fe,Ni) STA-12	1. Solvothermal synthesis of MOF@160 °C for 48 h 2. Phosphidation under argon vapor at 450 °C for 2 h	182	273	85 (HER) 79 (OER)	100 h at 500 mA cm^{-2}

(1) All full-cell voltages are for two-electrode alkaline cells at 10 mA cm^{-2} unless otherwise noted. (2) When only half-cell data are available, we have marked the missing metric as "—".

techniques to identify and modify MOF-derived LDHs during electrochemical conditions. However, to date very few studies employing these methods of investigation extend to real-time transformation of MOF-derived LDHs under synthetic conditions. LCTEM is one powerful microscopy technique that has been widely explored to study mostly the transformation dynamics of ZIF-based MOFs. In this section we discuss the principles and applications of the same. Whether these observed pathways apply to other MOF families with different metal nodes, ligand chemistries, and structural stabilities remains still unknown. Therefore,expanding LCTEM studies to non-ZIF MOFs is essential for establishing broader principles governing MOF-to-LDH reconstruction.

6.1.1. *In situ* liquid cell transmission electron microscopy (LCTEM). LCTEM is a powerful technique that enables the direct observation and analysis of samples in a liquid environment using a TEM (Fig. 10). In this technique, a liquid cell is used to encapsulate the sample in a thin liquid layer between two electron-transparent windows.[120] The liquid cell is then inserted into the TEM, allowing the electron beam to pass through the liquid and interact with the sample in real time. By continuously imaging the sample under the electron beam while controlling the liquid environment, researchers can study various processes, such as nanoparticle synthesis, chemical reactions, and biological interactions, to gain insights into the behaviour and transformations of materials and nanoparticles in a liquid environment.[121,122] Considering all the advances of LCTEM, it has also enabled the researchers to image the morphological and structural evolution such as etching, dissolution, and recrystallization dynamics of MOFs and MOF-derived LDHs in real time under controlled chemical conditions, providing unprecedented insight into the reaction pathways and kinetics.[18,117,123]

Mirsaidov *et al.* reported a detailed mechanistic insight into the transformation of ZIF-8 MOF nanoparticles (NPs) into hollow LDH nanocages, using LCTEM to visualize the process in real time (Fig. 11).[18] It was found that the $Co(NO_3)_2$ solution induces etching of the MOF *via* proton-mediated linker cleavage, while Co^{3+} and Zn^{2+} ions co-deposit as LDH nanosheets on the MOF surface. ZIF-8 nanocubes and rhombic dodecahe-

Fig. 10 Schematic diagram of a LCTEM and its application for imaging phenomena in various fields, adapted from ref. 120 with permission from American Chemical Society,[120] copyright 2021.

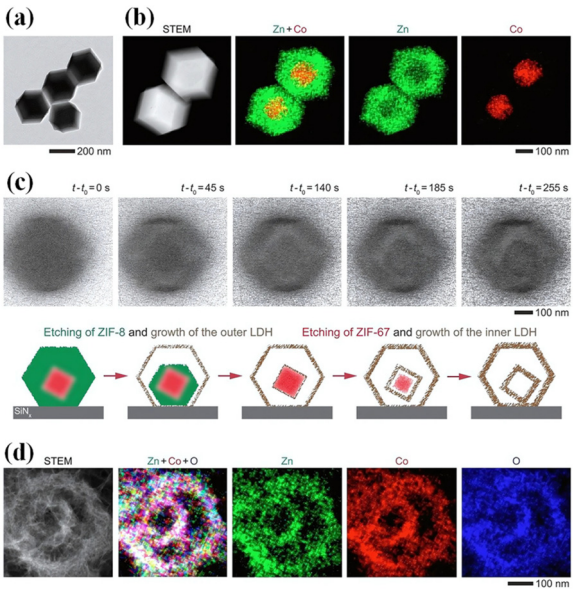

Fig. 11 Conversion of **ZIF-67@ZIF-8** core–shell NPs into "shell-in-shell" LDH nanocages *via* etching. (a) TEM and (b) STEM images of **ZIF-67@ZIF-8** core–shell NPs. (c) Sequential *in situ* liquid-phase TEM images captured at room temperature, showing the stepwise transformation of a **ZIF-67@ZIF-8** nanoparticle into a shell-in-shell LDH nanocage in 5 mg mL^{-1} $Co(NO_3)_2$ ethanol–water. A schematic illustration outlines the overall conversion pathway from the initial MOF core–shell particle to the final nested LDH structure. (d) STEM image with corresponding EDX mapping of the resulting shell-in-shell LDH nanocage, obtained under the same reaction conditions post *in situ* transformation, adapted from ref. 18 with permission from American Chemical Society,[18] copyright 2021.

drons were used as sacrificial templates, wherein simultaneous etching led to the LDH nanosheet growth in the presence of cobalt salt in ethanol–water media of V_{EtOH}/V_{H_2O} = 0.5. The study confirmed that the conversion process could be extended to fabricate more intricate hollow LDH nanostructures derived from MOFs. Specifically, **ZIF-67@ZIF-8** nanoparticles with cubic cores and rhombic dodecahedral (RD) shells were employed, as visualized *via* TEM and STEM images in (Fig. 11(a)) and (Fig. 11(b)), respectively. This approach led to the formation of unique shell-in-shell LDH architectures. As illustrated in (Fig. 11(c)), the transformation of a core–shell **ZIF-67@ZIF-8** particle began with the selective etching of the ZIF-8 RD shell in $Co(NO_3)_2$ solution, accompanied by the rapid formation of an outer LDH layer during the early stage ($t - t_0$ = 0–45 s). Continued etching led to the full removal of ZIF-8, yielding an RD LDH nanocage around the ZIF-67 core, which subsequently began to convert into its own inner LDH shell ($t - t_0$ = 140–185 s). With prolonged reaction time, ZIF-67 was completely etched, resulting in a final shell-in-shell LDH nanoparticle, where an inner LDH nanocage was encapsulated within an outer one. The EDX elemental mapping in (Fig. 11(d)) clearly revealed the spatial distribution of both the outer and inner LDH layers, confirming the hierarchical hollow structure. During the *in situ* LCTEM, it was observed that the conversion began with nucleation of LDH on MOF surfaces, preferentially on specific crystal facets. Ultimately, the core–shell **ZIF-67@ZIF-8** NPs were transformed into "shell-in-shell" LDH nanostructures, demonstrating the approach's versatility for advanced catalyst design. The reaction required a delicate balance between etching and growth rates; optimal conditions leading to LDH shells that preserved the original MOF shape, while excessively fast etching resulted in complete MOF dissolution without LDH formation. By tuning precursor concentration and solvent composition, the morphology of the final hollow LDH structures could be controlled. This method has enriched the scope for the synthesis of more complex architectures such as shell-in-shell LDH nanocages using core–shell MOF templates.

In essence, the roles played by transient intermediates, ligand decomposition kinetics, and facet-dependent nucleation remain insufficiently understood. Additionally, this approach is complicated by the potential for the electron beam to damage the sample or alter the reaction pathway. Bridging these gaps will be critical for achieving predictive control over MOF-to-LDH transformations and unlocking their full potential in designing efficient and durable catalysts for sustainable energy conversion.

6.2. *Operando* characterization for studying *in situ* transformations of MOF-derived LDHs during EWS

Operando characterization techniques have become essential tools for probing the dynamic, real-time structural, electronic, and chemical transformations that MOF-derived LDHs experience under the harsh electrochemical environment of water splitting, enabling researchers to directly correlate transient active phases with catalytic performance. This section discusses the various techniques involved in MOF-derived LDHs for OER (Table 2).

6.2.1. *In situ* Raman spectroscopy and infrared spectroscopy (IR). Raman spectroscopy uses monochromatic laser light to illuminate a sample, where most photons scatter elastically and a few inelastically, exchanging energy with molecular vibrations or rotations. The resulting Raman shift, the energy difference between incident and scattered photons, reveals the sample's unique molecular structure and composition through non-destructive spectroscopic analysis. It can detect low-wavenumber vibrational modes associated with metal–ligand or metal–oxygen bonds, enabling the identification of catalytic active sites and key intermediate species that are typically inaccessible through infrared spectroscopy. Raman spectroscopy offers rich structural insights into surface species and intermediates; however, conventional Raman spectroscopy often lacks the sensitivity required to detect trace active species adsorbed on catalyst surfaces.[124]

To overcome this limitation, shell-isolated nanoparticle-enhanced Raman spectroscopy (SHINERS) has been developed as a powerful *in situ* technique.[125] SHINERS employs core–shell nanostructures, typically Au cores coated with ultrathin silica shells, as Raman signal amplifiers, providing exceptional surface sensitivity while maintaining catalytic stability. By integrating *operando* SHINERS measurements with density func-

Table 2 General *in situ* characterization techniques for the mechanistic study of MOF-derived LDH

In situ techniques	Intermediates identified	Disadvantages	Mitigation
Raman spectroscopy: Monitoring chemical and structural changes, active-site formation, and reaction intermediates	Metal–O, M–H stretching vibrations	Weak signal and limited sensitivity for certain species like H_{ads}, O_2	The use of surface-enhanced Raman (SERS) amplifies weak Raman signals and enhances sensitivity to surface-bound intermediates
	O_2*, *OOH, *OH signals	Laser-induced heating or damage can alter the sample *e.g.*, oxidize LDH or degrade MOFs, especially at higher powers	Low-power lasers & short acquisition minimizes laser-induced damage
	MOOH formation (OER); limited HER insight (M–H bonding inferred)	Spectral overlap: Overlapping bands (*e.g.*, metal–O and M–OH) can complicate peak assignment and mechanistic interpretation	Coupling with other techniques (*e.g.*, ATR-FTIR, XAS, XPS) provides complementary chemical and structural insights
	Oxidation/reduction of catalyst surface	Bubble interference: In alkaline water splitting, bubbles (O_2, H_2) can obstruct the laser path and distort Raman signals	Time resolution is limited unless using fast-acquisition setups or pulsed lasers. Careful cell design (*e.g.*, flow cells, gas outlets) reduces bubble and alignment issues
Attenuated total reflectance Fourier transform infrared (ATR-FTIR): molecular-level insight into vibrational modes of the intermediates, structural evolution, and catalyst–electrolyte interactions under electrochemical conditions	Vibrational modes of intermediates, catalyst–electrolyte interface dynamics:	**Water absorption interference:** water has strong IR absorption, especially in the O–H bending and stretching	Replacing water with D_2O
	*O_2, *OH, *OOH, H_2O_2 *via* vibrational modes	**Low signal for thin films or poorly adsorbed species**: if the catalyst layer is too thin or the intermediates are weakly adsorbed, the signal may be too low to detect meaningful changes	Use of thin, well-adhered electrocatalyst layers on infrared-compatible substrates
	Anion adsorption (*e.g.*, Cl^-, SO_4^{2-}) Understanding interlayer anion exchange (*e.g.*, $CO_3^{2-} \leftrightarrow OH^-$) M–OH, M–$O_2$ formation and dynamics Carbonyl, hydroxyl, nitride vibrations	**Complex cell design:** the *in situ* ATR-FTIR setup requires a well-designed spectro-electrochemical cell that maintains good contact between the electrode, crystal, and electrolyte, which can be technically challenging	Combining complementary techniques—*e.g.*, Surface-Enhanced *Infrared Absorption Spectroscopy (SEIRAS)* + *XAS* + *Raman*—to get complete insight into structure, oxidation states, and adsorbed intermediates during HER/OER
Atomic force microscopy–infrared spectroscopy (AFM-IR): chemical, structural, and morphological information at the nanoscale	*OH, *OOH, peroxide species on catalyst surfaces	**Water absorption interference**: water has strong IR absorption, especially in the O–H bending and stretching	Replace water with deuterated solvent (D_2O) to shift strong O–H vibrations (~3400 cm^{-1}) out of the critical IR region
		Low IR absorption signal in liquid media: electrical noise from electrochemical reactions can interfere with AFM sensitivity	Use custom-designed electrochemical cells with thin electrolyte layers or IR-transparent windows
		Limited spectral range and resolution in liquid: operating in aqueous environments narrows the usable IR window due to water's absorption, especially in the 1500–3700 cm^{-1} range (relevant for O–H/N–H vibrations)	Use pulsed laser sources and lock-in amplification to enhance signal-to-noise ratio under aqueous conditions
		Small sample area/low throughput: AFM-IR provides nanoscale resolution but only probes a very small area at a time	Pair AFM-IR with *in situ* Raman, SECM, or EC-AFM, where one offers structural resolution and another gives chemical or electrochemical insight
Synchrotron radiation–Fourier transform infrared spectroscopy (SR-FTIR): high-resolution FTIR under *operando* conditions, with spatial resolution, brightness, and signal-to-noise ratio	Molecular vibrations, surface reactions, and chemical changes	SR-FTIR requires access to synchrotron facilities, making it costly and less accessible	Using collaborative synchrotron access and efficient scheduling to manage limited availability
	Ideal for studying complex reactions and heterogeneous materials	Sample preparation is demanding, and *in situ* measurements are challenging due to cell compatibility issues	Apply thin-film techniques for better sample prep
	Identifies *OOH, *OH, peroxide, O_2 species	The intense beam can cause sample damage or heating	Design custom IR-transparent *in situ* cells (*e.g.*, with CaF_2 windows)
	Probes adsorbed anions (Cl^-, SO_4^{2-}, *etc.*)	It also has limited time resolution for fast processes and involves complex data interpretation due to overlapping signals and environmental interference	Complement with faster techniques for dynamics. Use spectral deconvolution tools to handle complex data

Table 2 *(Contd.)*

In situ techniques	Intermediates identified	Disadvantages	Mitigation
	Detects oxide/hydroxide formation		Minimize beam damage by reducing exposure or scanning the beam
	Observes carbon oxidation or ligand breakdown		
Electrochemical impedance spectroscopy (EIS): evaluating charge transport, reaction kinetics, interfacial behaviour, and material stability	Solution resistance (R_s,charge transfer resistance(R_ct)double-layer capacitance (C_dl),Warburg impedance (Z_w),pseudo capacitance, interfacial processes and degradation	Data interpretation is complex and model-dependent	Use well-validated equivalent circuit models and complementary techniques for accurate interpretation
		Measurements are time-consuming at low frequencies	Limit frequency range to reduce time
		Susceptible to noise and environmental instability	Shield setup to minimize noise. Ensure stable experimental conditions and use reference electrodes with low drift
		Lacks spatial resolution and requires system stability	
X-ray photoelectron spectroscopy (XPS)	Monitoring electronic structure, oxidation states, and surface composition of catalysts	Surface-sensitive (\~5–10 nm), limiting bulk information	Use ion sputtering or angle-resolved XPS for depth profiling
	Transition metal oxidation (*e.g.*, $Ni^{2+} \rightarrow Ni^{3+}$) during OER	Requires high vacuum, restricting *in situ*/*operando* studies	Employ *in situ*/near-ambient pressure XPS setups for realistic conditions
	Generation of surface hydroxyls and oxygen vacancies	Charging effects can distort data for non-conductive samples	Apply charge neutralization to reduce charging in insulating samples
	Formation of protonated species during HER	Quantification is semi-quantitative and sensitive to sample prep	Calibrate with standards to improve quantification
		Slow data acquisition for large areas or depth profiling	Optimize sample prep to ensure surface cleanliness and stability
X-ray absorption spectroscopy (XAS): monitoring the oxidation state (*via* XANES) and local atomic structure (*via* EXAFS) of catalyst	Transition to higher oxidation states (*e.g.*, Ni^{3+}/Co^{3+})	Requires synchrotron access and complex setup	Combine with complementary techniques (*e.g.*, XPS, Raman) for holistic interpretation
	Tracks oxidation state shifts and coordination environment changes under operational bias/light	Limited time resolution for fast reactions	Use beamline facilities with fast detectors for better time resolution
	Identifies active phases—such as Ni(0), MOOH, linking them to performance and durability	Data analysis (especially EXAFS) is complex and model-dependent	Apply advanced fitting software and reference standards to improve EXAFS/XANES analysis accuracy
	Phase reversibility or permanent restructuring identified	Sample damage under intense beams is possible	Employ cryogenic conditions or beam attenuation to reduce sample damage
		In situ/*operando* cell design can be challenging	Design specialized *in situ*/*operando* cells compatible with synchrotron setups
Liquid cell transmission electron microscopy (LCTEM): nanometre-scale imaging of dynamic processes such as MOF-to-LDH transformations	Direct visualization of phase changes	Limited spatial resolution due to electron scattering in liquid	Use low-dose imaging to reduce beam damage
	Links morphology changes to performance	Beam-induced radiolysis can alter sample chemistry	Employ radiolysis scavengers to minimize beam-induced chemistry
	Real-time nanoscale resolution	Small liquid volume may not represent bulk behavior	Optimize cell thickness and liquid layer to enhance resolution
		Complex cell fabrication and sealing	Design robust, controllable microfluidic cells for better environmental control
		Difficult to control temperature, flow, and electrochemical environment precisely	Combine with complementary techniques for cross-validation

tional theory (DFT) calculations, researchers have successfully identified the reaction pathways and transient intermediates in heterogeneous catalytic systems, such as CO oxidation over PtFe and Pd nanocatalysts.[124] These studies directly observed surface species including oxides, superoxide/peroxide intermediates, and metal–carbon bonds, offering molecular-level insights into catalytic processes. The success of SHINERS demonstrates its strong potential for probing real-time surface transformations and identifying active intermediates during *in situ* electrochemical reactions such as the oxygen and hydrogen evolution reactions in water splitting.

Both Raman and FT-IR spectroscopy can reveal detailed molecular microstructural information from surfaces as thin as 10 nm. Hence, combining both provides a comprehensive understanding of molecular behavior.[126] Recently, their *in situ* applications have become widely employed to monitor changes in chemical bonding during phase transitions of MOFs and their derivatives, and to track the formation of active species during the EWS process.[127–129] However, most current studies on *in situ* Raman analysis of the EWS are conducted at room temperature. Since industrial water electrolysis typically operates at elevated temperatures (50–80 °C), developing high-temperature *in situ* Raman setups would enable evaluation of the temperature sensitivity of MOF structures and provide a deeper understanding of how reconstruction behavior varies with temperature.[130–132]

IR spectroscopy enables fingerprint identification of polarized oxygen-containing intermediates involved in the OER, appearing within the 800–1600 cm^{-1} region. However, this range is particularly susceptible to interference from water absorption. To improve signal strength and surface sensitivity, advanced approaches such as utilizing synchrotron radiation (SR) sources with enhanced IR intensity (SR-FTIR), attenuated total reflectance infrared (ATR-FTIR) spectroscopy and surface-enhanced infrared absorption (SEIRA) techniques have been introduced.[133]

In this context, some researchers have recently developed an *operando* SR-IR technique to probe the OER mechanism.[134,135] Cheng *et al.* used *operando* SR-FTIR to study a lattice-strained NiFe-MOF, where a new band at 1048 cm^{-1} appeared at 1.6 V *vs.* RHE, indicating OOH intermediates. Correlation of SR-FTIR–XAS analyses linked the Ni^{4+}/Ni^{2+} ratio with IR intensity near 1050 cm^{-1}, emphasizing high-valent Ni^{4+} species as active sites. The transient nature of these intermediates demonstrates the value of *operando* IR for real-time mechanistic insight. Similarly, Shao-Horn *et al.* used a combination of *in situ* SEIRA spectroscopy and DFT studies to detect the formation of –OO species on polycrystalline RuO_2.[136]

These *operando* vibrational techniques offer powerful insights into the dynamic reconstruction of MOF-derived LDHs under working conditions. When combined with other complementary techniques they can yield a comprehensive view of lattice evolution, surface chemistry, and catalytic kinetics, enabling rational design of MOF-derived LDHs with enhanced stability and efficiency for practical water splitting.

6.2.2. *In situ*/*operando* electrochemical impedance spectroscopy (EIS). Electrochemical impedance spectroscopy (EIS), and increasingly *in situ*/*operando* EIS, provides a quantitative window into charge-transfer and interfacial processes that accompany the electrochemical activation and reconstruction of electrocatalysts.[137] In typical experiments the impedance is measured across a broad frequency window (commonly 100 kHz → 0.1–0.01 Hz) at catalytic bias points or during potential sweeps to extract solution resistance (R_s), charge-transfer resistance (R_{ct}) and non-ideal capacitive behaviour (CPE) *via* equivalent-circuit modelling. *In situ* EIS measurements have been performed by various researchers to probe the OER reaction kinetics of OER electrocatalysts.[138,139]

Maximum mechanistic insights can be drawn from pairing *operando* EIS with complementary *operando*/spectroscopic probes like Raman, XAS, Differential Electrochemical Mass Spectrometry (DEMS) and activity measurements. EIS tracks how the electrical and mass-transport landscape evolves, while spectroscopy methods identify the chemical/structural nature of the newly formed active phases and mass-spectrometric methods confirm changes in reaction intermediates or selectivity.

6.2.3. X-ray absorption spectroscopy (XAS): monitoring the oxidation states (*via* XANES) and local atomic structure (*via* EXAFS). XAS is a powerful technique for probing the electronic structure and local atomic environment of active sites in catalysts under operating conditions (Fig. 12). It analyzes the energy-dependent fine structure in the X-ray absorption spectrum to reveal detailed geometric and electronic information.[140] It is noteworthy that XAS studies of 3d transition metals are typically conducted at the K-edge, as their edge energies exceed 4000 eV, eliminating the need for ultrahigh vacuum conditions. This makes XAS particularly suitable for *in situ* investigations.[141]

When the incident X-ray energy is below an element's electron binding energy, electrons remain in their ground state, resulting in a nearly flat spectral region with occasional weak pre-edge peaks. At higher energies, electrons are ejected into continuum states, generating interference between outgoing and scattered waves. These oscillations, seen in the EXAFS region, reveal local structural details such as bond lengths and coordination numbers.[143,144] In EXAFS analysis, the local

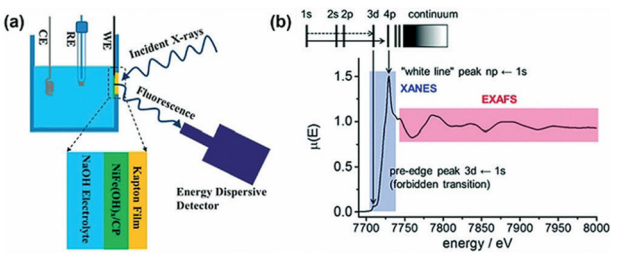

Fig. 12 (a) *In situ* XAS setup scheme and (b) schematic representation of a K edge spectrum; blue: XANES region, red: EXAFS region, adapted from ref. 142 with permission from Wiley,[142] copyright 2019.

structural characteristics are reflected in the radial distribution function, providing valuable insights into the number of neighboring atoms, interatomic distances, and structural disorder, all of which are critical for elucidating reaction mechanisms.[145] Consequently, such structural information is instrumental in establishing correlations between the configuration of catalytic centers and their activity, as revealed through quasi-*operando* and *operando* XAS studies. Also, XAS is a bulk-sensitive technique that provides an average valence state of both surface and bulk regions. Thus, an observed increase in metal valence from *in situ* XAS reflects surface oxidation but does not directly quantify the surface valence state. In contrast, acquiring EXAFS data in electron yield mode enables surface-sensitive analysis (within 1–2 nm), allowing detailed characterization of the local surface structure.

In addition to determining the coordination environment of active centers through EXAFS analysis, identifying the oxidation states of active species is crucial for unraveling the bottleneck OER mechanism.[119,145–147] As the energy increases enough to excite core electrons to unoccupied states, absorption rises sharply, forming the XANES region. XANES provides insight into unoccupied electronic states and is highly sensitive to both the oxidation state and coordination geometry of the absorbing atom. The edge position reflects the oxidation state, while pre-edge features stemming from the normally forbidden 1s to 3d transition become pronounced under reduced symmetry, such as in tetrahedral coordination, serving as indicators of local structural symmetry. A well-established linear correlation between the XANES edge position and the oxidation state has made this technique an effective means of probing the electronic states of catalytic elements.

Recent efforts have increasingly focused on quasi-*operando* and *operando* XANES studies to monitor the dynamic changes in oxidation states of OER catalysts under realistic conditions.[119,145] Wu *et al.* combined quasi-*operando* XANES with theoretical calculations to elucidate the role played by Ni sites in a bimetallic Ni–Fe system. Their findings revealed that electronic interactions with adjacent Fe atoms modulate the Ni electronic structure, generating low-valence Ni centers that bind key OER intermediates with optimal strength, while Fe sites exhibit overly strong adsorption.[148] Since the oxidation state of active species is strongly dependent on the applied potential during electrochemical operation, *operando* XAS measurements are essential to capture these dynamic transformations.[149] Su *et al.* utilized *operando* XANES to investigate the potential-dependent evolution of NiFe–PBA precatalysts. With increasing potential, the absorption edge shifted to higher energies, indicating the oxidation of Ni to higher valence states and the *in situ* formation of amorphous $Ni(OH)_2$ as the true OER-active phase. This oxidation process was reversible and significantly more pronounced than in crystalline $Ni(OH)_2$, underscoring the capability of *operando* XANES to correlate oxidation-state dynamics with catalytic performance.[124]

Furthermore, XAS is generally divided into two types: hard XAS, which uses high-energy X-rays to probe bulk properties and heavy elements *via* core-level transitions, and soft XAS, which employs lower-energy X-rays to study surface-sensitive phenomena and valence band transitions. Hard XAS is typically performed in transmission mode, offering bulk-sensitive analysis with minimal self-absorption effects. In contrast, soft XAS is measured using fluorescence yield (TFY) and electron yield (TEY) modes, with probing depths of a few hundred nanometers and a few nanometers, respectively.[150] The choice of detection mode depends on the sample characteristics; transmission mode suits well-prepared, concentrated samples, while fluorescence yield is preferred for dilute systems or those in dense environments.[151]

Operando XAS studies have provided crucial insights into the structural evolution MOF based electrocatalysts.[119] Lou *et al.* reported a Br-confined Ni-MOF system, where sequential transformations from the pristine framework to a β-$Ni(OH)_2$-like intermediate and finally to a γ-NiOOH phase were observed under operating conditions.[152] The resulting γ-NiOOH exhibited excellent OER activity, attributed to strong Br–Ni electronic interactions that promote *O intermediate formation and enhance reaction kinetics. Similar studies have been included in this review wherein *in situ* XAS has proved to be beneficial for understanding the working of MOF-derived LDHs under electrochemical conditions.

6.2.4. X-Ray photon–electron spectroscopy (XPS). In X-ray photoelectron spectroscopy (XPS), the absorption of X-ray photons induces the emission of photoelectrons into the continuum.[153] XPS is a powerful technique for probing the elemental composition, chemical oxidation states, and electronic environments of materials.[154,155] However, conventional *ex situ* or quasi-*in situ* XPS often fails to represent the true surface chemistry of electrocatalysts under reaction conditions, as air exposure and lack of applied potential can alter the oxidation states of surface species. To overcome these limitations, ambient-pressure XPS (AP-XPS), also known as near-ambient pressure XPS (NAP-XPS), enables real-time surface analysis at subtorr to torr pressures and under electrochemical bias, bridging the "pressure gap" between ultra-high vacuum measurements and realistic catalytic environments (Fig. 13). *In situ* AP-XPS enables direct monitoring of the electrode electrolyte interface by operating with an ultrathin liquid layer, thereby allowing the investigation of catalytic surfaces under near-realistic environments. AP-XPS in combination with other characterizations and DFT has been increasingly applied to study the surface chemistry of electrocatalysts such as transition-metal-based oxides, hydroxides, and (oxy)hydroxides under conditions relevant to the oxygen and hydrogen evolution.[148,156]

In the context of MOF-derived LDHs, *operando* XPS is especially valuable for monitoring ligand removal, metal oxidation, and interfacial species evolution during electrochemical activation.[17,158] When combined with DFT calculations and *operando* XAS, it can provide a consistent picture linking surface oxidation, electronic reconstruction, and catalytic performance.[18,78,123] AP-XPS faces challenges such as limited pressure windows (<1–5 Torr) and signal attenuation for dilute or nanoparticle catalysts, as highlighted by Nguyen

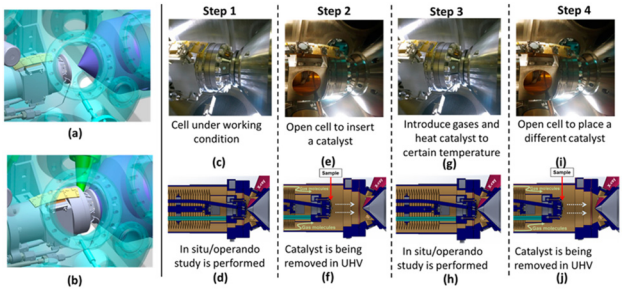

Fig. 13 Newly designed reaction cell integrated into the AP-XPS system of the Tao group. (a) Reaction cell positioned before engagement with the front-cone aperture of the differential pumping stage; (b) reaction cell engaged with the front cone; (c) photograph of the cell under operating conditions; (d) internal configuration of the cell corresponding to panel (c); (e) cell under vacuum after completing the *in situ* experiment; the gas has been purged and the chamber door opened, making it ready for sample removal. (f) Internal structure of the cell in the open state, with the sample stage retracted for easy sample retrieval. (g) Cell prepared for a new *in situ* measurement after inserting a fresh sample, introducing the reaction gas, and heating the system to the required temperature. (h) Internal structure of the cell in its ready-to-operate configuration. (i) Photograph of the cell in standby mode while awaiting the next sample. (j) Corresponding internal structure of the cell, adapted from ref. 153 and 157 with permission from American Chemical Society[153] & AIP publishing,[157] respectively Copyright 2019 & 2022, respectively.

et al. in their comprehensive review.[153] Continued advances in spectrometer design, "tender" X-ray sources, and electrochemical AP-XPS cells are expanding its applicability to liquid-phase electrocatalysis, making it a cornerstone technique for probing the authentic working surfaces of MOF-derived LDHs under true operating conditions.

7. DFT calculations and theoretical insights into water splitting on MOF-derived LDHs

Density Functional Theory (DFT) has become an indispensable tool for unraveling the intrinsic catalytic mechanisms of water splitting, particularly the OER.[159,160] DFT provides atomic-level insights into electronic structure, adsorption energetics, and reaction thermodynamics, enabling the elucidation of catalytic activity trends beyond experimental reach. The key intermediates involved in the OER *OH, *O, and *OOH species are sequentially adsorbed on possible active sites to compute the Gibbs free energy change (ΔG) of each elementary step according to the four-electron reaction pathway:

$$* + H_2O \rightarrow *OH + H^+ + e^-$$

$$*OH \rightarrow *O + H^+ + e^-$$

$$*O + H_2O \rightarrow *OOH + H^+ + e^-$$

$$*OOH \rightarrow * + O_2 + H^+ + e^-$$

The overpotential (η) is then estimated from the largest uphill ΔG among these steps according to:

$$\eta = \frac{\max(\Delta G_i)}{e} - 1.23\,\mathrm{V}$$

where 1.23 V represents the thermodynamic equilibrium potential for OER at standard conditions.

The parameters such as solvent effects, applied potential, and pH, impart valuable impact on "*in situ*/*operando*" theoretical studies. Generally, DFT calculations assume a vacuum environment, overlooking crucial interactions at the solid–liquid interface. To better represent electrochemical conditions, solvent effects must be incorporated through explicit or implicit models. In EWS studies, explicit solvent effects typically account for surface-adsorbed or nearby species such as H_2O, OH^-, H^+, H_3O^+, *etc.* which significantly influence reaction energetics and intermediate stabilization. Solvent molecules can directly influence electrochemical reactions by stabilizing intermediates and modifying catalytic pathways. While explicit models capture direct solvent participation, implicit approaches approximate these effects using the solvent's dielectric constant to represent the reaction environment.[161,162] Current DFT studies of the OER often rely on static, implicit-solvent treatments or a few ordered water layers, which miss key interfacial physics: hydrogen-bond networks, proton-transfer chains, electric-double-layer (EDL) structure, field-dependent charge distribution, and dynamic solvent reorganization that can change both adsorption geometries and reaction barriers. Explicit-solvent and hybrid approaches like *ab initio* molecular dynamics (AIMD), constant-potential DFT, and hybrid quantum mechanics/molecular mechanics (QM/MM) routinely produce different energetics and mechanisms than purely implicit models, so more systematic, realistic solvent modeling is needed to bridge theory with *operando* experiments.[163] Hence, future computational efforts should place greater emphasis on accurately incorporating solvent effects to better reflect real electrochemical environments.

The applied potential and electrolyte pH can markedly alter catalyst surface states, impacting OER activity and pathways. Theoretical studies can thus explore how surface structures evolve with changes in potential and pH, extending beyond simple free-energy analyses.[164] DFT studies to evaluate the OER mainly focus on the thermodynamic aspects of the reaction pathway, either through the adsorbate evolution mechanism (AEM) or *via* the lattice oxygen oxidation mechanism (LOM), which involves direct O–O bond formation from lattice oxygen species.[165] However, due to their computational complexity, reaction kinetics in the OER are less frequently explored than thermodynamics. Transition-state DFT calculations reveal that proton-transfer steps proceed readily, while O–O bond formation (*OOH) presents the highest barrier and is typically rate-determining.[166] Some studies show that these barriers can be tuned through synergistic effects.[167] Notably, neglecting kinetic factors often leads to underestimated theoretical overpotentials.

7.1. Correlation between DFT predictions and experimental observations

A key strength of combining DFT with *in situ*/*operando* spectroscopy and machine learning lies in its ability to correlate atomic-scale theoretical descriptors with experimentally accessible observables, providing a holistic understanding of water-splitting mechanisms.[99,146,168,169] DFT-derived parameters such as d-band center position, charge redistribution, and adsorption free energies of *OH, *O, and *OOH intermediates directly influence macroscopic quantities like overpotential, Tafel slope, and impedance-derived charge-transfer resistance (R_{ct}). DFT calculations show shifting of the d-band centers or optimized OOH adsorption energy typically correspond to tuning of the experimental overpotentials and OER kinetics, as verified by *in situ* Raman, EIS and Tafel analyses.[82,99] Similarly, computed electron-density difference maps and Bader charge analysis provide quantitative insight into charge redistribution among active metal centers, revealing how defects, dopants, or interfaces modulate electronic structure and adsorption energetics, the key factors governing OER kinetics and supported by experimental EIS trends[170,171]

8. Mechanistic insights and surface evolution of MOF-derived LDHs during EWS: *in situ*/*operando* characterization and DFT studies

The process of structural evolution of materials under electrochemical conditions is complex and dynamic, involving the continuous rearrangement of a material's internal structure. To gain a comprehensive understanding of this phenomenon, a combination of *in situ*/*operando* characterization techniques is often necessary. Therefore, the studies enumerated here outline the use of these techniques independently as well as in combinations (Table 3). Wang *et al.* reported the fabrication of edge-enriched (EE) NiFe-LDH nanosheet arrays *via* an *in situ* electrochemical transformation of ZIF-67 nanosheet array directly grown on NF (Fig. 14(a)).[61] The NiFe-BDC array served as a structure-directing template and working electrode in a three-electrode system. The electrochemical transformation of NiFe-BDC MOF NSs into ultrathin NiFe-LDH NS took place using CV in the potential window of 0–0.5 V *vs.* SCE for 50 cycles at 50 mV s^{-1} in 1 M KOH. The EE-NiFe-LDH array delivered an overpotential of 205 mV@10 mA cm^{-2} (Fig. 14(b)) and retained 95% of its current density @100 mA cm^{-2} over 24 hours, demonstrating excellent OER activity and long-term durability. The authors have carried out *operando* Raman studies during the OER, in 1 M KOH, to verify the formation of NiOOH as active catalyst for the OER (Fig. 14(c) & (d)). With increasing potential, two Raman peaks at 456 and 530 cm^{-1} shifted to 474 and 548 cm^{-1}, respectively, indicating the oxidation of Ni(II) to Ni(III) corresponding to transformation from $Ni(OH)_2$ to NiOOH.[172,173] NiOOH formation occurred at a lower potential 1.4 V in the EE-NiFe-LDH array compared with the C-NiFe-LDH (common NiFe-LDH NS) at 1.45 V, reflecting faster Ni(II)/Ni(III) conversion and lower overpotential. This was attributed to the EE-NiFe-LDH's higher density of edge sites with unsaturated coordination, which narrowed the bandgap, enhanced the conductivity, and promoted NiOOH formation.[174] At 1.4 and 1.45 V, the NiOOH signals were stronger in EE-NiFe-LDH, confirming faster kinetics and higher intrinsic OER activity.

DFT studies supported by EXAFS-derived structural models revealed that the superior OER performance of EE-NiFe-LDH originated from the coexistence of Fe and O vacancies. Surface reconstruction to NiFeOOH during OER was considered, and free energy calculations identified Fe as the true active site, with a lower overpotential (theoretical) 440 mV compared with Ni 620 mV. While isolated Fe or O vacancies improved activity moderately, their coexistence further optimized intermediate adsorption and reduced energy barriers, shifting the rate-determining step from O* formation, in pristine NiFe-LDH, to HO* formation.[170] Additionally, Bader charge and PDOS (Partial Density of States) analysis showed that vacancies-enriched Fe sites with higher electron density and narrowed band gap enhanced the conductivity and facilitated charge transfer, in agreement with the EIS. These findings highlighted that coupled Fe–O vacancies and edge-rich structures synergistically tuned electronic states and catalytic energetics, thereby underpinning the remarkable OER activity of EE-NiFe-LDH.

Ni-MOF/LDH heterostructures were synthesized *via* a "MOF-on-MOF" growth strategy, where Ni-MOF was first formed on nickel foam, followed by deposition of oxalate-based MOF (Ox-MOF) and *in situ* alkaline transformation into LDH (Fig. 15(a)).[99] The optimized Ni-MOF/LDH electrode exhibited OER performance requiring a low overpotential of 220 mV to reach 10 mA cm^{-2} and showed a small Tafel slope of 36 mV dec^{-1}, outperforming its pure Ni-MOF and LDH counterparts (Fig. 15(b) & (c)). Mechanistic studies using *in situ* Raman spectroscopy and XPS revealed that Ni sites acted as the primary active centres *via* the generation of NiOOH during OER (Fig. 15(d)–(f)). *In situ* Raman spectroscopy revealed distinct signals at approximately 530 and 700 cm^{-1} when the applied potential was set to 0.1–0.4 V *vs.* Hg/HgO, corresponding to Ni–O stretching vibrations and potential iron hydroxide phases, respectively. Notably, upon increasing the potential to 0.5 V *vs.* Hg/HgO, the Raman spectrum exhibited significant changes, with the emergence of new peaks at 482 and 561 cm^{-1}, attributed to the formation of NiOOH. Furthermore, XPS analysis showed that the Ni $2p_{3/2}$ and $2p_{1/2}$ peaks in Ni-MOF/LDH shifted positively by 1.4 eV and 1.8 eV, respectively, while the Fe $2p_{3/2}$ peak shifted negatively by 2.5 eV compared with the LDH. These shifts indicated partial electron transfer from the Ni-MOF to the LDH, leading to a reduced electron density at the Ni sites, which in turn promoted the formation of NiOOH active species (Fig. 15(g)). These observations indicated that Ni sites played a key role in driving the OER process.

DFT studies demonstrated that Ni-MOF/LDH heterostructures exhibited enhanced conductivity with a higher DOS

Table 3 Summary of reported mechanistic studies of MOF-derived 2D LDH for electrocatalytic water splitting

In situ transformation of MOF into LDHs	Electrochemical activity	*In situ* characterization for the mechanistic study	Mechanistic insights drawn	Ref.
ZIF-67@ZIF-8 NPs were transformed into "shell-in-shell" LDH nanostructures	NA	*In situ* LCTEM	The reaction requires a delicate balance between etching and growth rates; Tuning precursor concentration and solvent composition, the morphology of the final hollow LDH structures can be controlled	18
Nucleation and growth of MOF nanoparticles, ZIF-8 and UiO-66 in real time	NA	*In situ* LCTEM	Successful tracking of particle formation under realistic synthesis conditions Changing the metal: ligand ratio altered growth kinetics and final particle size, highlighting the potential of LCTEM for mechanistic studies and rational control of MOF crystal size and structure during synthesis	122
Edge-enriched (EE) NiFe-LDH nanosheet arrays *via in situ* electrochemical transformation of ZIF-67 nanosheet array directly grown on NF (NiFe-LDH NS)	Overpotential of 205 mV@10 mA cm^{-2} and retained 95% of its current density@100 mA cm^{-2} over 24 hours	*In situ* Raman spectroscopy	The appearance of two Raman peaks at 456 and 530 cm^{-1} shifting to 474 and 548 cm^{-1}, respectively, signifies the oxidation of Ni^{2+} to Ni^{3+} and the corresponding phase transition from $Ni(OH)_2$ to NiOOH, identifying the formation of NiOOH as the active OER species	61
"MOF-on-MOF" growth strategy, where Ni-MOF was first formed on NF, followed by deposition of oxalate-based MOF (Ox-MOF) and *in situ* alkaline transformation into Ni/MOF/LDH	OER performance, requiring a low overpotential of 220 mV to reach 10 mA cm^{-2} and showing a small Tafel slope of 36 mV dec^{-1}	*In situ* Raman spectroscopy	At applied potentials of 0.1, 0.2, 0.3, and 0.4 V *vs.* Hg/HgO, distinct Raman signals appeared around 530 and 700 cm^{-1}, corresponding to Ni–O stretching modes and possible iron hydroxide species When the potential was raised to 0.5 V *vs.* Hg/HgO, notable changes occurred in the Raman spectrum, including the emergence of new peaks at 482 and 561 cm^{-1}, indicative of NiOOH formation	99
CoNi-BDC@LDH electrocatalyst synthesised *via* a one-pot hydrothermal method	OER performance; it reaches 100 mA cm^{-2} at a potential as low as 1.512 V *vs.* RHE at 5 mV s^{-1}, overpotential of 282 mV	Quasi-*operando* analysis: Raman, FTIR, XPS, and XAS after exposing the samples to a specific electrochemical environment for a set duration	Raman spectra showed the transformation of $Ni(OH)_2$ to γ-NiOOH at ≥1.53 V, with characteristic peaks at ~479 and 557 cm^{-1} ATR-FTIR revealed a growing 1090 cm^{-1} band (O–O bond formation) and peaks at ~3590, 1560, and 617 cm^{-1}, indicating surface hydroxyl adsorption and structural changes during OER XPS showed redox shifts: Ni^{3+}/Ni^{2+} decreased (1.23–1.43 V) then increased (1.63 V), while Co^{3+}/Co^{2+} followed the opposite trend, suggesting Ni–Co redox synergy	175
LDH-NDs@C-MOF, confinement-synthesis strategy to fabricate NiFe layered double hydroxide nanodots (LDH-NDs) anchored onto a 3D porous carbon network derived from ZIF-67	Performance with a low overpotential ~230 mV@10 mA cm^{-2}, outperforming both traditional LDH nanosheets and commercial RuO_2	*Operando* XAS, XANES, EXAFS-FT	The *in situ* Ni K-edge XANES spectra showed a clear shift in the white line from 8350.5 eV to 8351.0 eV when a potential of 1.45 V was applied, indicating oxidation of Ni^{2+} to higher valence states under working conditions EXAFS-FT analysis under the same conditions revealed a pronounced distortion and peak splitting in the Ni–Ni	177
Co–Cr oxyhydroxide catalyst (Cr–CoOOH) derived from ZIF-8	The current density at 1.53 V of the Cr–CoOOH is 11.3 mA cm^{-2}, which is 12 times higher than that of pure CoOOH,overpotential of Cr–CoOOH at 10 mA cm^{-1} was 290 mV, (lower than that of 400 mV for CoOOH and even lower than that of 300 mV for IrO_2)	*Operando* ATR-FTIR, EIS, XPS	*Operando* ATR-FTIR showed a blue shift of the OOH* band from 1186 to 1220 cm^{-1}, confirming OOH* adsorption on Cr sites in Cr–CoOOH *Operando* EIS supported enhanced surface deprotonation and charge transfer due to Cr incorporation, providing direct evidence of Cr-site activity Cr oxidation from Cr^{3+} to Cr^{4+} during OER highlights its dynamic redox role XPS analysis revealed Ni^{3+}/Ni^{2+} initially decreased (1.23–1.43 V) then increased (1.63 V), while Co^{3+}/Co^{2+} showed the reverse trend, indicating Ni–Co redox synergy	169

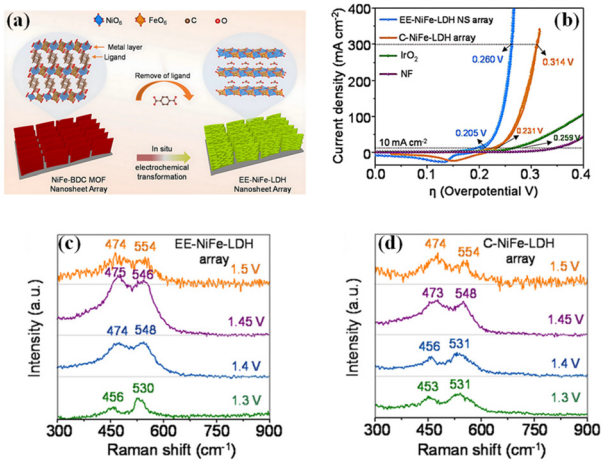

Fig. 14 (a) Schematic representation of the structure-inheritance strategy for fabricating the edge-enriched NiFe-LDH nanosheet **(EE-NiFe-LDH NS)** array, using a NiFe-BDC MOF nanosheet array as a structure-directing template; (b) comparative CV/LSV curves of EE-NiFe-LDH array, conventional **NiFe-LDH (C-NiFe-LDH)** array, IrO_2, and bare NF in 1 M KOH with 95% iR compensation; (c) *operando* Raman spectra of the **EE-NiFe-LDH** array and (d) **C-NiFe-LDH** array collected in the potential range of 1.3–1.5 V *vs.* RHE in 1 M KOH, adapted from ref. 26 with permission from Elsevier,[26] copyright 2021.

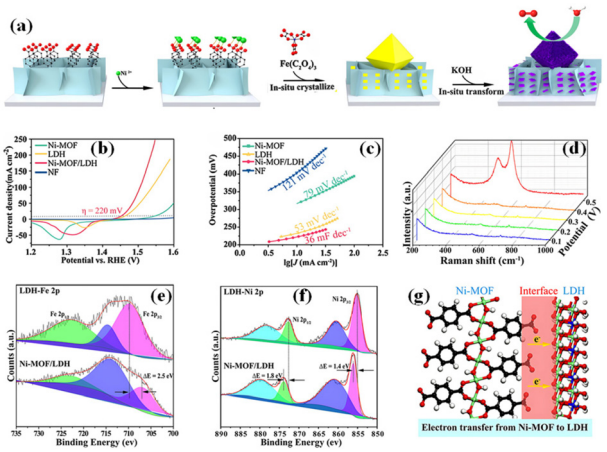

Fig. 15 (a) Schematic illustration of the *in situ* transformation process from Ni-MOF/Ox-MOF to **Ni-MOF/LDH**, depicting the structural evolution during LDH formation; (b) LSV curves comparing the overpotentials of the investigated electrocatalysts; (c) corresponding Tafel plots derived from (b); (d) *in situ* Raman spectra of **Ni-MOF/LDH** recorded under varying applied potentials; (e) high-resolution XPS spectrum of the Fe 2p region, revealing the oxidation states and electronic structure of Fe in LDH; (f) XPS spectrum of the Ni 2p region in **Ni-MOF/LDH**; (g) schematic diagram illustrating partial electron transfer at the heterostructure interface, adapted from ref. 99 with permission from Elsevier,[99] copyright 2021.

near the Fermi level and an upshifted d-band center (−1.33 eV) compared with Ni-MOF (−2.06 eV) and LDH (−1.85 eV), which strengthened intermediate adsorption. The rate-determining barrier was significantly reduced for Ni-MOF/LDH (ΔG = 2.4 eV) relative to Ni-MOF (6.8 eV) and LDH (3.2 eV), highlighting the role played by interfacial electron transfer in optimizing Ni active sites. This facilitated NiOOH formation and confirmed the superior OER performance of the heterostructure.

In situations where true *in situ* characterization is hindered by instrumental limitations, such as the requirement for high vacuum conditions, quasi-*operando* analysis can be employed. This approach involves sequential *ex situ* characterization using techniques like Raman spectroscopy, FTIR, XPS, and XAS after subjecting samples to a defined electrochemical environment, thereby approximating *in situ* conditions. A quasi-*operando* analysis on CoNi-BDC@LDH electrocatalyst synthesised by Liu *et al. via* a one-pot hydrothermal method provided detailed insights into the structural and chemical transformations that occurred during the OER.[175] This structure featured numerous CoNi-LDH nanoplates vertically aligned on cuboidal MOF cores, creating abundant bimetallic Co–Ni interfacial active sites (Fig. 16(a)). To simulate *in situ* conditions, the catalyst was subjected to different applied potentials: 1.23 V, 1.33 V, 1.43 V, 1.53 V, and 1.63 V *vs.* RHE in 1 M KOH for 15 minutes, followed by *ex situ* characterizations.

Raman spectra revealed a transformation from $Ni(OH)_2$ to γ-NiOOH at higher potentials ≥1.53 V. There were peaks at ~479 and 557 cm^{-1}, indicating the formation of γ-NiOOH, a known active phase that plays a crucial role in facilitating the OER process by promoting Ni^{2+} to Ni^{3+} oxidation (Fig. 16(b)).[176] ATR-FTIR spectra showed a growing band at 1090 cm^{-1} with increasing potential, indicating O–O bond formation and the presence of peroxo-like species bridging Ni and Co, evidence for a dual-metal-site mechanism (DMSM)

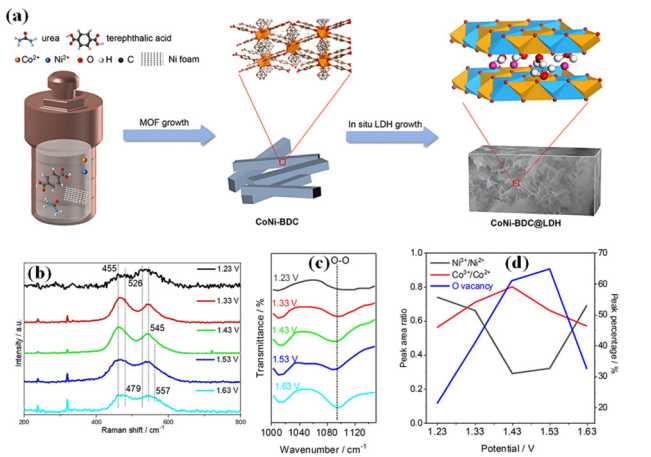

Fig. 16 (a) Schematic illustration of the synthesis process for the hierarchical **CoNi-BDC@LDH** core–shell structure; (b) *ex situ* Raman spectra of **CoNi-BDC@LDH** under various applied potentials, showing the emergence of additional peaks (~479 cm^{-1} and 557 cm^{-1}) at higher overpotentials; (c) enlarged ATR-FTIR spectra highlighting O–O bond formation at 1090 cm^{-1} under different potentials; (d) variation in Co and Ni valence states and oxygen vacancy concentrations, as determined by XPS, after electrochemical treatment at different potentials, adapted from ref. 175 with permission from Elsevier,[175] copyright 2023.

that enhanced the OER kinetics *via* cooperative metal interactions (Fig. 16(c)). Additional FTIR peaks around 3590, 1560, and 617 cm^{-1} confirmed increasing surface hydroxyl adsorption and transformation during OER. XPS revealed dynamic redox shifts: the Ni^{3+}/Ni^{2+} ratio initially decreased (1.23–1.43 V), then rose again (1.63 V), while Co^{3+}/Co^{2+} showed an inverse trend, indicating Ni–Co redox cooperation (Fig. 16(d)). The oxygen vacancy trend paralleled Ni^{3+} changes, suggesting vacancies form near Ni and are vital for activity. Together, these results support a lattice oxygen-mediated mechanism (LOM) involving the formation of a Ni–O–O–M intermediate at the LDH–BDC interface. Ni primarily drove oxygen activation and desorption, while Co facilitated Ni oxidation. This interplay, along with the formation of γ-NiOOH and CoOOH during operation, enhanced OER performance of **CoNi-BDC@LDH**. They have achieved a superior OER activity *via* a synergistic dual-metal-site and lattice oxygen-mediated mechanism involving dynamic Ni/Co redox interactions and active intermediate formation.

Zhang *et al.* presented a simple, template-free strategy to fabricate composition-tunable MOF-derived LDHs for water oxidation applications.[168] They reported the synthesis of hierarchical trimetallic LDH nanosheets *via in situ* transformation through alkaline treatment (Fig. 17(a)). Upon the dropwise addition of 1 M KOH, the copper foil surface gradually changed from light yellow to dark yellow, and the MOF-to-LDH transformation was completed within 30 minutes. The optimized **$FeCo_{0.5}Ni_{0.5}$-LDH** catalyst retained the octahedral morphology of the MOF precursor while forming ultrathin monolayer nanosheets of ~1 nm, significantly enhancing surface area and charge transport. The catalyst demonstrated excellent activity in alkaline media, requiring only 248 mV overpotential to achieve 10 mA cm^{-2} and exhibiting a Tafel slope of 38 mV dec^{-1} (Fig. 17(b) & (c)). *In situ* Raman analyses revealed NiOOH as the main active species and a beneficial electronic modulation effect from Co incorporation. Despite a modest electrochemical surface area, the catalyst showed high intrinsic activity and stability over 50 hours at both moderate and high current densities (Fig. 17(d)).

A study by Dai *et al.* reported a novel confinement-synthesis strategy to fabricate NiFe layered double hydroxide nanodots (LDH-NDs) anchored onto a 3D porous carbon network derived from ZIF-67 (Fig. 18(a)).[177] This **LDH-NDs@C-MOF** catalyst showed superior OER performance with a low overpotential ~230 mV@10 mA cm^{-2}, outperforming both traditional LDH nanosheets and commercial RuO_2 (Fig. 18(b) and (c)). The *in situ* XAS studies were critical in identifying the active sites and understanding the charge transfer processes in the **LDH-NDs@C-MOF** catalyst during the OER. The *in situ* Ni K-edge **XANES** spectra showed a clear shift in the white line from 8350.5 eV to 8351.0 eV when a potential of 1.45 V was applied, indicating oxidation of Ni^{2+} to higher valence states under working conditions (Fig. 18(d)). This shift was not observed in the LDH nanosheets (LDH-NSs), suggesting enhanced redox activity in the nanodots. Moreover, the **EXAFS-FT** analysis under the same conditions revealed a pro-

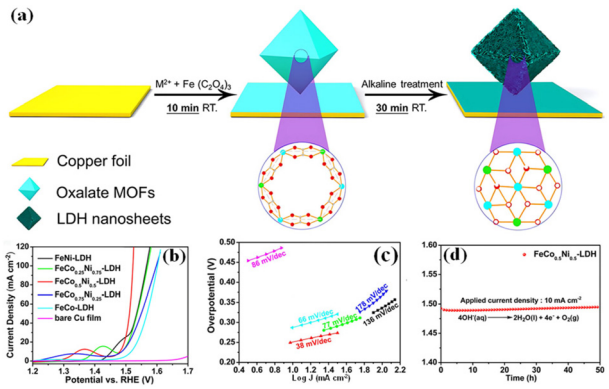

Fig. 17 (a) Schematic depiction of the *in situ* transformation process of oxalate-based MOFs into LDHs; (b) IR-compensated LSV curves comparing the catalytic performance of FeNi-LDH (black), **$FeCo_{0.25}Ni_{0.75}$-LDH** (green), $FeCo_{0.5}Ni_{0.5}$-LDH (red), **$FeCo_{0.75}Ni_{0.25}$-LDH** (blue), **$FeCo_1$-LDH** (brilliant blue), and bare copper foil (purple); (c) corresponding Tafel plots to evaluate the reaction kinetics of the catalysts; (d) chronoamperometric stability curve for **$FeCo_{0.5}Ni_{0.5}$-LDH**, showing current response over time, adapted from ref. 168 with permission from Elseiver,[168] copyright 2020.

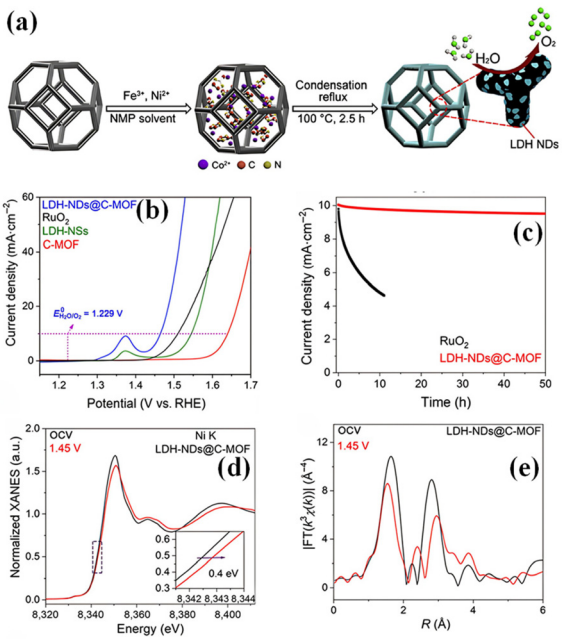

Fig. 18 (a) Schematic representation of the synthesis procedure for the Ni–Fe-based MOF-derived catalyst, comprising LDH nanodots anchored on a MOF-derived carbon network (LDH-NDs@C-MOF); (b) polarization curves of LDH-NDs@C-MOF, LDH-NSs, C-MOF, and commercial RuO_2 in O_2-saturated 1 M KOH at a scan rate of 5 mV s^{-1}; (c) durability comparison between LDH-NDs@C-MOF and RuO_2 at a rotation speed of 1000 rpm in O_2-saturated 1 M KOH; (d) *in situ* Ni K-edge XANES spectra comparison, with the inset showing the shift in the Ni K-edge white line of LDH-NSs before and after applying a potential of 1.45 V; (e) EXAFS-FT collected on the as-prepared LDH-NDs@C-MOF under the OCV and 1.45 V adapted from ref. 177 with permission from Springer Nature,[177] copyright, 2021.

nounced distortion and peak splitting in the Ni–Ni coordination shell for LDH-NDs@C-MOF, further supporting the presence of more edge defects and dynamic structural changes during catalysis (Fig. 18(e)). For Fe, no significant shift in the Fe K-edge XANES was observed due to the stability of Fe^{3+}, but the EXAFS Debye–Waller factor increased under applied potential, indicating structural disorder. These *in situ* findings, combined with *ex situ* XAS and DFT, confirmed that a partial charge transfer occurred from Fe^{3+} to Ni^{2+} *via* bridging oxygen, optimizing the binding energy of OER intermediates and enhancing catalytic activity. This work not only identified active edge sites in LDH-NDs but also presented a general route for designing high-performance electrocatalysts *via* nano confinement and carbon support engineering.

The theoretical insights from DFT calculations provided a crucial understanding of the OER activity observed in the LDH-NDs@C-MOF catalyst. Since metals randomly disperse in LDH, they have constructed two representative structures models, A and B, with ratios of $Fe^{3+}:Ni^{2+}$ being 1 : 2 and 1 : 3, respectively.[171] Bader charge analysis of these models revealed a critical partial charge transfer from Fe^{3+} to Ni^{2+} through a bridging oxygen atom. This electronic redistribution resulted in a decreased average charge on Fe and an increased charge on Ni, which optimally tuned the electronic structure for adsorbing OER intermediates.

Further analysis of the reaction mechanism identified two potential pathways, with the most favorable route occurring synergistically on oxygen-bridged Ni–Fe edge sites. The bridging oxygen atom at these active sites was found to carry a less negative charge than other oxygen atoms in the structure, facilitating the crucial step of OH^- adsorption and O–O bond formation. The free energy diagrams depicted that all elementary OER steps became thermodynamically downhill at an applied potential of 0.624 V. To quantitatively compare activity, the difference in adsorption energies of the *OH and *OOH intermediates was used as a descriptor in a volcano plot. Strikingly, the edge-defect models of the LDH-NDs occupied the peak of this volcano, exhibiting the lowest theoretical overpotentials (as low as 0.222 V), which were superior to both vacancy-free models and even commercial RuO_2. These comprehensive DFT results robustly supported the experimental evidence by confirming that the high density of edge sites in the nanodots governs the enhanced catalytic performance through optimized electronic structure and intermediate binding energetics.

Deng *et al.* used various *operando* techniques to identify the true active sites and their dynamic behaviour during the OER in a Co–Cr oxyhydroxide catalyst (Cr–CoOOH) derived from ZIF-8 MOF.[169] The incorporation of high-valence Cr atoms into active species showed a 12-fold OER enhancement over pure CoOOH (Fig. 19(a)).

Operando EIS provided direct spectroscopic evidence of OOH* on the Cr site by tracking reaction kinetics and intermediate formation during the OER (Fig. 19(b)). Nyquist plots above 1.4 V resulted in two resistive, low-frequency semi-circle components for deprotonation resistance and a high-frequency semi-circle for OER charge-transfer resistance (R_{ct}). Cr-

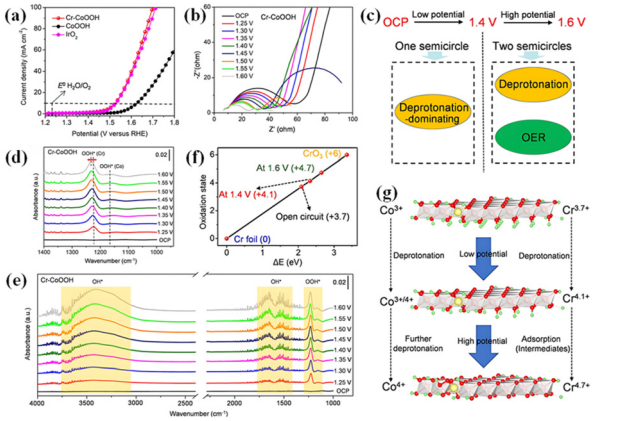

Fig. 19 (a) OER polarization curves of various catalysts loaded on a glassy carbon electrode without *iR* correction (*i* = current, *R* = resistance); (b) *operando* EIS spectra of the Cr–CoOOH catalyst recorded under different applied potentials during the OER process; (c) schematic of multistep deprotonation and OER under working conditions; (d) ATR-IR spectra of Cr–CoOOH collected at various potentials in the range of 1400–1000 cm^{-1}; (e) *operando* ATR-IR spectra of CoOOH in the range of 4000–1000 cm^{-1}, capturing OER intermediates during the reaction; (f) fitted average valence states of Cr derived from XANES analysis; (g) proposed reaction mechanism illustrating the dynamic behavior of Co and Cr sites during the OER process, adapted from ref. 169 with permission from Elsevier,[169] copyright 2021.

CoOOH showed significantly lower R_{ct} than CoOOH, which is a clear indication of the enhanced kinetics and easier intermediate adsorption. The EIS results demonstrated that Cr incorporation enhanced both surface deprotonation and charge transfer during OER, confirming its catalytic advantage (Fig. 19(c)).

Operando ATR-IR spectroscopy was conducted to detect surface-bound OOH* on the OER intermediate (Cr–CoOOH). A distinct blue shift of the OOH* band from 1186 cm^{-1} (CoOOH) to 1220 cm^{-1} (Cr–CoOOH) indicated OOH* adsorption on Cr sites. The shift with increasing potential suggested potential-dependent Cr–OOH* interaction. These results provided direct spectroscopic evidence that Cr sites, and not Co, bind OOH* intermediates, identifying them as the active OER sites (Fig. 19(d) & (e)). Thus, incorporation of high-valence metals like Cr into oxyhydroxide matrices offers a promising route to boost OER performance.

Operando XAS was employed to monitor real-time changes in the oxidation states and local coordination environments of Co and Cr in a Cr-doped CoOOH catalyst during the OER. There was a dynamic oxidation from $Cr^{3.7+}$ to $Cr^{4.7+}$ during the OER, indicating its active role. Also, the Cr–O bond shortening under applied potentials, suggested the formation of OER intermediates on Cr sites (Fig. 19(f)). Based on the observed changes in oxidation states and coordination environments of the metal centers, a reaction mechanism was proposed to explain the dynamic behavior of Co and Cr sites during the OER process (Fig. 19(g)).

DFT analysis revealed that at 1.6 V *vs.* RHE, the basal planes of both Cr–CoOOH and CoOOH readily deprotonated, a process reflected experimentally by the observed increase in

Co and Cr oxidation states. Edge sites, however, remain protonated under these conditions, requiring potentials above 2.09 V. Using the deprotonated basal-plane structures, mechanistic calculations showed that the OER proceeds most efficiently on edge-confined Cr atoms, which lower the limiting potential to 1.72 V, substantially below that of edge-Co in Cr–CoOOH (2.14 V) or pure CoOOH (2.09 V). In-plane Cr sites were inactive, demanding an unrealistically high potential of 2.54 V. The enhanced activity of edge-Cr originates from its higher density of 3d states, which optimizes O* binding relative to OH* and OOH*, equalizing intermediate energetics and minimizing the potential barrier. These findings pinpoint edge-Cr as the dominant active site, reconciling theoretical predictions with *operando* spectroscopic observations.

In conclusion, these studies demonstrate that edge-enrichment, interfacial engineering, and heteroatom doping can accelerate Ni(II)/Ni(III) and Co(II)/Co(III) conversions, optimize adsorption energetics, and enhance overall OER activity. However, critical gaps remain where most mechanistic insights are restricted to ZIF- and NiFe-based systems, the nature of early intermediates and ligand decomposition during MOF-to-LDH conversion is poorly understood, and many *in situ* techniques are limited by environmental constraints, forcing reliance on quasi-*operando* analyses that may not capture transient states.

9. Stability of MOF-derived LDH during OER: experimental validation and theoretical insights

The stability of MOF-derived LDH electrocatalysts during the oxygen evolution reaction represents a defining criterion for their practical deployment in alkaline water electrolysis, as the harsh oxidative potentials and strongly basic conditions impose substantial structural and chemical stresses on the catalyst. Unlike conventionally synthesized LDHs, MOF-derived LDHs possess atomically dispersed metal centers, hierarchical mesoporosity, and defect-rich nanosheet architectures that not only accelerate catalytic kinetics but also endow the material with improved resilience against dissolution and structural fatigue.[178,179] The stability of MOF-derived LDH electrocatalysts during the oxygen evolution reaction is governed by the active species actually formed under anodic bias, how those species are chemically stabilized, and how the reconstructed domains are mechanically and electronically supported by the remaining MOF-derived matrix or engineered heterointerfaces.[180] Most MOF/MOF-derived LDHs do not act as the final active phase but instead undergo controlled electrochemical reconstruction into high-valent oxyhydroxides or mixed-metal LDH domains whose composition, defect density and local coordination environment determine both activity and durability.[33,76,181] For instance, MOFs such as ZIF-67,[182–184] NBU-4,[33] MOF-74,[185] and Ni–MOF[186] readily transform into corresponding oxyhydroxides under anodic polarization. Nonetheless, *operando* studies show that these high-valent M(III)/M(IV) centers and adjacent oxy/hydroxy ligands appear rapidly during activation and, when hosted in ultrathin, defect-rich LDH nanosheets derived from MOF precursors, can remain the dominant surface species during prolonged OER provided that metal leaching and organic decomposition are minimized.[187]

The chemical stability of the active species is therefore determined by factors including (a) composition (*e.g.*, metal–metal ratio), which controls the ability to stabilize high-valent states (NiFe-LDHs stabilize Ni(III/IV) and improve OER kinetics),[188,189] (b) defect and coordination structure (edge sites and under-coordinated metal centers are most active but also most vulnerable to dissolution),[190,191] and (c) the presence of residual conductive carbon/graphitic shells from partial MOF carbonization, which buffer volume changes and maintain electronic percolation, factors repeatedly correlated with improved long-term potential stability in chronopotentiometry tests.[95,192]

Crucially, the MOF precursor acts as a molecular template that controls metal ratio, spatial dispersion and porosity so the *in situ* formed LDH has abundant under-coordinated edge sites (the true catalytic centers) along with residual carbonaceous frameworks or conductive residues.[193] The most important part of the MOF is the ligand framework that plays a pivotal role in modulating both the morphology and the electrocatalytic performance of the resulting LDH electrocatalyst. This is evident from the work of Hu *et al.*, where the 2,5-dihydroxyterephthalate (DHTP) ligand released from MOF-74 during its dissociation chemically modified NiFe LDH.[194] This ligand promoted the formation of Ni(III) and resisted Cl^- corrosion. Thus, LDH-MOF74@NF outperformed almost all previously reported NiFe LDH@NF electrocatalysts, exhibiting excellent OER performance and high durability in KOH and KOH/NaCl solutions. Similar reports have been reported in MOF-derived hydroxides/oxyhydroxides where the nature of the linker significantly influences not only the stability and integrity of the MOF but also governs the transformation pathway and kinetics during electrochemical activation.[195,196] Parameters such as ligand basicity (pK_a), steric effects, π–π stacking interactions, and impact on porosity and hydrophilicity collectively determine how and when the metal–ligand coordination bonds break, allowing hydroxide ions to replace the linkers and form catalytically active metal hydroxides.

Furthermore, it has been reported that the synergistic effect of two metal centers in LDH can enhance both the activity and stability of the LDH electrocatalyst. In the work of Lang *et al.*, DFT calculations revealed pseudo re-oxidized metal-stable Ni^{3+} near oxygen vacancies (O_{vac}), which suppressed the 3d-e_g of the Ni-site and elevated the d-band center towards the competitively low electron-transfer barrier during the OER.[197] A similar observation has also been reported for bimetallic MOF precursors reconstructing into LDHs whose durability under accelerated durability tests and long chronopotentiometry has been benchmarked with *operando* studies to show retention of high-valent oxyhydroxide signatures even after extensive

cycling, evidence that a controlled reconstruction pathway yields a robust active phase rather than a fragile transient one.[76,198–200]

Furthermore, when the LDH is intimately interfaced with conductive carbon (LDH/carbon),[201–203] oxides (LDH/oxides),[204,205] sulfides (LDH/sulfides)[206] or a metallic scaffold (LDH/metal),[170,207] a heterojunction is formed which is a powerful route to stability. This heterointerface electronically stabilizes high-valent centers *via* interfacial charge redistribution and mechanically confines reconstructed domains to prevent aggregation, delamination and rapid metal loss.[192,208,209] For example, the Co-LDH@ZIF-67 core–shell heterojunction structure reported by Yang *et al.* exhibited good stability over 50 h of constant current density of 30 mA cm^{-2}.[210] Similarly, MOF-derived $CoSe_2$@NiFeOOH heterostructures show enhanced OER durability for 100 h CPE at 1.54 (V *vs.* RHE) owing to the synergistic effect of the inner layer $CoSe_2$ and NiFeOOH outer layer.[137] Similarly, the work of Wang regarding the (Co,Ni)Se_2@NiFe layered double hydroxide (LDH) nanocage derived from ZIF-67 exhibited good stability over 17 h of continuous chronopotentiometry at 10 mA cm^{-2} owing to the synergistic effect between iron and nickel/cobalt in optimizing the adsorption/desorption nature of the oxygenated species and the partial delocalization of spin status at the interface (π electron transfer occurred *via* the bridging O^{2-}).[211]

Additionally, MOF/LDH heterojunctions are also reported to enhance performance and stability through generation of defects, optimizing the energy barrier of the OER process, and decrease the adsorption energy of oxygen-containing intermediates.[76] In this context controlled and partial hydrolysis of NiFe MOF led to formation of a NiFe MOF/LDH (NiOOH served as active site) heterojunction with interfacial charge transfer showing minimal potential drift over 50 h at 100 mA cm^{-2}, validated through experimental as well as theoretical calculations.[198] However, excessive hydrolysis, whether by prolonged duration or higher temperature, drives complete conversion of the MOF into LDH, which eliminates the heterojunction and disrupts the internal charge-transfer pathway, ultimately diminishing OER activity. In contrast, a finely tuned partial transformation preserves the MOF/LDH interface, enabling synergistic electronic coupling that delivers superior catalytic performance.[198] A similar observation was also reported by Zhai *et al.* where the semi-transformed hierarchical Fe–Ni LDH/MOF-b2 exhibited better performance than the fully transformed Fe–Ni LDH/MOF-b3.[212]

Moreover, the stability of MOF-derived LDHs is greatly enhanced by fabricating self-supported electrodes grown directly on conductive substrates such as nickel foam or carbon cloth, further enhancing operational durability by preventing catalyst detachment under vigorous O_2 bubble evolution.[69] Chen *et al.* reported NiS@NiFe-LDH heterostructured nanosheet arrays on nickel foam (NF) which facilitated electrolyte diffusion and efficient release of bubbles, ensuring rapid electron transfer and robust electrochemical stability.[213] Similarly, Hu *et al.* reported NF-supported NiFe LDH electrodes directly derived from NF-supported-bimetallic MOF-74 (NiFe) known as LDH-MOF74@NF, exhibiting excellent OER performance and high durability in KOH and KOH/NaCl solutions.[194]

Apart from these, thermodynamic stability also plays a crucial role in the performance and durability of heterojunction-type catalysts derived from MOFs transforming into LDHs for the OER.[36,78,210] From a thermodynamic standpoint, stability is achieved when the active phase and heterointerfaces lie within the lowest-free-energy regions of the potential–pH phase diagram under OER conditions. Experimentally, heterojunctions with better lattice matching and stronger interfacial cohesion show much lower rates of overpotential increase and far less metal dissolution, key indicators of improved thermodynamic stability.[214] Unlike short-term activity metrics, thermodynamic stability describes whether the phases and interfaces present in the catalyst are the lowest-free-energy states under the electrochemical conditions of interest (potential, pH, temperature) and therefore whether they will persist or spontaneously transform, dissolve, or reconstruct during operation. It is well established that in strongly oxidizing aqueous media, metal oxides constitute the most thermodynamically favored state for the vast majority of metals.[215,216] Accordingly, a wide range of metallic compounds tend to undergo spontaneous conversion toward oxide or oxyhydroxide phases (during anodic polarization) under such conditions.[215,216] For MOF-derived systems, which commonly pass through ligand-leaching, dissolution–reprecipitation, and oxyhydroxide formation pathways,[28,36] the relevant stability questions are twofold: (i) which bulk phases (precursor, intermediate, final LDH/oxyhydroxide) are thermodynamically favored at OER potentials, and (ii) whether the heterointerface (LDH/support, LDH/oxide, remaining MOF fragments) is energetically coherent or prone to segregation or delamination.

The dissolution–redeposition equilibrium can also be deliberately tuned by introducing metal ions into the electrolyte. Under the right combination of substrate, potential, and ion concentration, a stable dynamic balance between metal dissolution and redeposition can be established, leading to markedly improved long-term durability. For example, trace amounts of Fe ions (~0.1 ppm) added to alkaline media enable transition-metal (oxy)hydroxides such as NiOOH, CoOOH, and NiCuOOH to develop dynamically stabilized Fe active sites.[217] These sites form through continuous Fe dissolution and redeposition and significantly enhance the catalyst's stability compared with Fe-free electrolytes. In this process, $[Fe(OH)_4]^-$ is believed to serve as the adsorbing species during anodic redeposition, with the Fe–host adsorption energy governing the overall equilibrium.[218] Similarly, incorporating foreign ions can meaningfully reshape the OER pathway in MOF-derived LDH systems.[219] During electrochemical reconstruction, external cations, from either the electrolyte or the MOF precursor, can integrate into the developing LDH framework, altering its electronic structure, active-site environment, and interaction with key OER intermediates (OH*, O*, OOH*), substantially boosting both catalytic activity and operational stability. In this context, Abdelwahab reported

a Sn-doped NiFe LDH integrated with ZIF-67, termed NiFe-LDH-Sn/ZIF-67.[219] Sn doping facilitated the electron transfer process by reducing the equivalent series resistance (ESR) from 325 Ω to 161 Ω, while ZIF-67 improved charge redistribution and catalytic stability by 91.8% after 24 h. Overall, tuning electrolyte metal ions offers a promising strategy to control OER pathways, enhance activity, and achieve durable, dynamically stable catalysis.

Apart from these, Kim *et al.* reported ZIF-67-derived FeCo-LDH. They employed different iron salts including $FeSO_4{\cdot}7H_2O$, $FeCl_2{\cdot}4H_2O$ and $Fe(NO_3)_3{\cdot}9H_2O$, which had a significant impact on the morphology and charge transfer properties of the resulting materials. Among them FeCo-LDH synthesized from iron sulfate solution (FeCo-LDH-SO_4) exhibited a hybrid structure of nanosheets and nanowires, exhibiting a long-term stability of 40 h for the OER.[220]

From a computational perspective, rigorous evaluation of thermodynamic stability combines *ab initio* (DFT) formation energies with electrochemical grand-canonical corrections (computational Pourbaix analysis) and, where feasible, explicit-solvent/constant-potential methods.[163,210,221,222] Theoretical Pourbaix diagrams provide a powerful lens for understanding catalyst evolution. By charting surface stability as a function of pH and potential, they illuminate when metal-based catalysts are prone to reconstruct or dissolve during the OER, thereby revealing the thermodynamic pathways that govern their transformation.[223] On the other hand, formation energies and vacancy formation energies (metal and oxygen) computed by DFT provide the baseline energetic ordering of crystalline phases and the cost of generating defects that often control activity. However, these vacuum energies must be adjusted for aqueous electrochemical environments by accounting for the chemical potentials of solvated ions and electrons (*i.e.*, potential and pH) to construct Pourbaix diagrams that predict the stability windows for solids *versus* dissolved ionic species. Constant-potential DFT, implicit/explicit solvent models, and AIMD snapshots are increasingly recommended because they capture electric double-layer and solvation stabilization effects that alter relative stabilities under bias.[163,224–227] Such combined computational workflows identify: (a) the dissolution potentials for cations (a direct predictor of leaching), (b) the thermodynamic driving force for phase transformation of LDH to amorphous oxyhydroxides or higher-valent species that may be more active but mechanically weaker or transient, (c) the energy of interfacial formation/adhesion that dictates robustness of heterojunctions and (d) lattice-oxygen participation (LOM) in which removal of lattice oxygen (thermodynamically favored under some compositions/defect densities) increases activity yet can progressively destabilize the lattice.[166] These pathways often compete with each other. For example, vacancy formation can simultaneously enhance *OOH binding (improving activity) and lower the energy required for lattice-oxygen loss (reducing stability). Quantifying these competing thermodynamic tendencies is therefore central to the rational design of active and stable MOF-derived electrocatalysts.

Nonetheless, few theoretical calculations are available in literature with respect to MOF-derived LDHs for OER. Yang *et al.* reported DFT calculations combined with interfacial engineering of a Co-LDH@ZIF-67 heterojunction that enhanced the strength of the $Co–O_{out}$ bond in Co-LDH, which made it easier to break the $H–O_{out}$ bond and resulted in a lower free energy change of the potential determining step in the OER and concurrently enhanced the structural stability under alkaline operation.[210] In another case, DFT combined with Monte Carlo simulation of a CoFe-LDH@$Ti_3C_2T_x$ heterojunction revealed guided growth energetics that reduced metal cation leaching and stabilized the conductor–LDH interface under high current densities, thereby improving both activity and thermodynamic resilience.[228]

Several recent studies illustrate how combined DFT/Pourbaix and *operando* experiments clarify stability–activity tradeoffs in MOF-derived LDH systems. Liquid-cell TEM visualizations of ZIF-derived transformations show etching and concurrent LDH nanosheet growth processes whose rates and completeness depend on solution composition and thus on the thermodynamic driving forces for MOF dissolution *vs.* LDH formation.[18,78,123] *Operando* studies on LDH and heterostructures reveal potential-driven oxidation and bond-length changes consistent with DFT-predicted energetics for active-phase emergence, while controlled heterointerface design (improved lattice match, stronger adhesion energies) reduces measured metal leaching and slows overpotential increase during prolonged OER tests.[214] These examples underscore that thermodynamic resilience is frequently achieved not by avoiding reconstruction, but by steering reconstruction toward stable, active, and electronically coupled phases *via* composition and interface engineering.[18]

Best practice for demonstrating stability therefore couples thermodynamic predictions validated with *operando* probes and electrolyte analysis. *Operando* X-ray absorption spectroscopy (XANES/EXAFS) and ambient-pressure XPS reveal potential-dependent oxidation state shifts and local coordination changes that indicate phase conversion (for example, $Ni^{2+} \rightarrow Ni^{3+}/Ni^{4+}$ accompanying γ-NiOOH formation), while *in situ* Raman/SHINERS and ATR-FTIR detect surface species and intermediates (*e.g.*, OOH*), corroborating DFT adsorption energetics. ICP-MS of the electrolyte quantitatively confirms cation leaching predicted from Pourbaix analysis, and LCTEM (liquid-cell TEM) can directly visualize MOF to LDH morphological evolution (etching, hollowing, nanosheet formation) under chemically driven conditions. Together, these *operando* and post-mortem methods link theoretical thermodynamic windows to real-time transformations and degradation modes.[187,229]

In summary, a thermodynamically robust MOF-derived LDH OER catalyst is one whose active phase and heterointerface lie within stable regions of the potential–pH phase diagram for the intended operating window, whose defect chemistry is tuned to balance activity with lattice integrity, and whose interfacial energetics ensure persistent electronic coupling under bias. Achieving this requires a coupled workflow of

DFT/Pourbaix modeling (including solvent and potential effects where possible), predictive interfacial energetics, and *operando* validation (XAS, AP-XPS, Raman) alongside quantitative leaching tests (ICP-MS) and long-duration electrochemical stress tests. Incorporating such thermodynamic assessments into studies of MOF-derived LDHs not only explains observed degradation mechanisms but also provides actionable routes to design catalysts that combine high OER activity with the long-term durability required for practical devices.[166]

10. Conclusions and perspectives

In summary, LDHs hold emerging prospects for designing and developing low-cost and high-performance electrocatalysts towards sustainable energy solutions. Owing to their excellent intrinsic structural and electronic properties, specifically their plentiful active sites, tunable chemical properties, and robust lattice structure, LDHs are today recommended as emerging functional materials. Future work integrating advanced *operando* methods like synchrotron XAS, cryo-TEM, and time-resolved vibrational spectroscopy with multiscale simulations will be essential to resolve active-site dynamics with higher precision, generalize the transformation mechanism across diverse MOF families, and enable rational catalyst design for scalable energy applications. Beyond OER, expanding the scope of MOF-to-LDH transformations to other electrocatalytic reactions such as the HER, CO_2 reduction, and nitrogen fixation will provide broader insights into structure–activity relationships. Additionally, coupling *operando* studies with machine learning-guided data analysis could accelerate the discovery of descriptors for active sites, while scalable synthesis strategies and integration into industrially relevant electrode architectures will be critical for translating these scientific advances into practical energy technologies.

To guide the future advancement of MOF-derived LDH materials for EWS, this article concludes with several perspectives as discussed below:

10.1. The rational design of the MOF precursor

The breakthrough in the advanced synthetic design of MOFs highlights the importance of a strong foundational understanding of MOF chemistry in driving meaningful progress and innovation in the field. For these materials to bridge the gap between laboratory research and industrial deployment, emphasis must also be placed on developing low-cost, scalable MOFs. To date, most efforts have centered around transition metal-based MOFs, particularly those containing Ni, Co, and Fe, for *in situ* conversion into LDHs aimed at water splitting. However, broadening the material palette to include more affordable and redox-active metal ions such as Mn, Cu, V, Cr, Mo, and W offers exciting opportunities. Such expansion in design strategy may pave the way for the next generation of efficient, robust, and scalable materials for clean energy technologies.

10.2. The *in situ* MOF-to-LDH transformation process

Various *in situ* synthetic strategies have been developed for transforming MOFs into LDHs. However, there remain pressing challenges, such as maintaining phase purity, achieving precise cation ratios, and controlling the release of metal ions, that are commonly encountered during LDH synthesis. Addressing these issues calls for rational and controllable structural design strategies that can minimize agglomeration during the *in situ* transformation process. Importantly, fine-tuning the structural and electronic properties of MOFs under actual reaction conditions may enable the formation of stoichiometrically precise and structurally well-defined LDH. The strategic selection of metal ions and organic linkers, combined with the power of advanced computational tools and machine learning, could pave the way for predictive design and efficient synthesis routes, ultimately leading to more reliable and high-performing MOF-derived LDH electrocatalysts.

10.3. In-depth characterizations and mechanistic understanding of the derivation of LDH electrocatalysts

The molecular and atomic-level mechanisms underlying the transformation of MOFs into LDHs remain largely elusive. Despite growing interest, a clear understanding of the dynamic structural and chemical evolution during this process is still lacking. Advanced *in situ* and *operando* characterization techniques, such as XAS, XPS, Raman spectroscopy, and TEM, are essential to capture real-time changes and unravel the transformation pathway. Moreover, limited knowledge of the reaction kinetics, diffusion behaviour, and thermodynamic driving forces continues to hinder the development of high-performance MOF-derived LDH electrocatalysts. During the MOF-to-LDH transformation and subsequent OER operation, the applied anodic potential can induce not only LDH formation and oxygen evolution but also the redeposition of dissolved metal species. Though often overlooked, this phenomenon can markedly influence the catalytic pathway. It underscores that dissolution–redeposition dynamics are strongly governed by the catalyst's intrinsic composition and structural features.

To overcome these challenges, systematic investigations and computational modelling are necessary to enhance transformation efficiency and gain precise insights into atomic arrangements, lattice dynamics, interlayer spacing, defect formation, and the roles played by individual components. Leveraging both theoretical and experimental approaches, including machine learning and spectroscopic tools, will enable the rational design of next-generation electrocatalysts with optimized performance and stability.

10.4. Performance/stability of MOF-derived LDH electrocatalysts

Despite notable advancements, MOF-derived LDH electrocatalysts still face several critical challenges. A key limitation lies in their narrow functional scope. Most studies to date have primarily focused on their application in the OER, with limited exploration of truly bifunctional systems capable of efficiently

catalyzing both the HER and OER within the same electrolyte environment. One promising approach for addressing these shortcomings involves the construction of well-integrated MOF–LDH heterostructures or hybrid composites anchored onto conductive substrates such as carbon cloth or nickel foam. These architectures not only improve electron transport pathways but also enhance mechanical stability during prolonged electrochemical operation for overall bifunctional activity. Furthermore, the deliberate incorporation of dopants and the engineering of defects, such as oxygen vacancies or heteroatom substitution, can significantly modulate the electronic structure of LDH layers. Such modifications enable the fine-tuning of adsorption energies and facilitate faster reaction kinetics for key electrochemical processes, including the OER and HER.

Dissolution and redeposition processes play a major role in determining the long-term stability of OER catalysts, driven by harsh acidic/alkaline conditions, oxidative environments, and even processes such as surface reconstruction or lattice-oxygen involvement. Because dissolution behavior varies with catalyst facets, substrates, and applied potentials, its mechanisms remain complex and not fully understood. Moreover, dissolved species in the electrolyte can influence catalytic activity or undergo redeposition, a phenomenon that has received relatively little attention despite its significant impact on long-term stability. Future research should focus on the roles played by ion effects and redeposition during electrochemical operation.

Furthermore, recent studies have shown that catalysts such as mixed Ni–Fe hydroxides behave very differently under cyclic voltammetry (CV) and chronoamperometry (CA), highlighting the sensitivity of catalyst structure to applied potential. While CV cycling can simulate start-up and shutdown conditions in practical electrolyzers, it does not fully capture the complex redox-driven structural changes that occur under steady OER operation. Therefore, meaningful stability evaluation should rely on long-duration chronoamperometry or chronopotentiometry tests, typically hundreds of hours, supported by measurements of dissolved metal species.

Looking forward, future research must focus not only on boosting intrinsic catalytic activity but also on ensuring long-term operational durability under industrially relevant conditions.

10.5. Regeneration and recyclability of MOF-derived LDHs

Although MOF-derived LDHs often exhibit good initial stability, little is known about their reactivation or recyclability after performance decay. We rarely encountered an article directing research towards understanding the degradation mechanisms of and developing regeneration strategies for MOF-derived LDHs. The future scope lies in identifying the dominant degradation mechanisms through post-mortem and *operando* analyses, and in developing regeneration protocols that restore or enhance activity, such as thermal treatment, chemical reactivation, or electrochemical cycling. Establishing a clear understanding of recyclability will not only improve the sustainability of MOF-derived LDHs but also provide critical insights for designing more robust catalysts capable of long-term, industrially relevant operation.

10.6. Role played by electrolytes in electrocatalytic WS using MOF-derived LDHs

The influence of electrolyte composition such as pH, ionic species, and additives on catalyst stability and activity is often overlooked. Tailoring electrolyte environments to stabilize active phases and optimize ion transport could be as important as catalyst design itself. Future directions should focus on integrated catalyst–electrolyte optimization, combining *operando* characterization and computational modeling to map how different electrolyte environments influence active site stability, reaction pathways, and ion transport kinetics. Such insights will be essential for moving MOF-derived LDHs from proof-of-concept demonstrations to practically viable water-splitting systems, where electrolyte engineering and catalyst design evolve hand-in-hand.

10.7. Hybrid structures with 2D materials

The integration of LDHs with 2D supports like MXenes, graphene, and GQDs has shown promising improvements in conductivity, dispersion, and stability. A key research gap lies in the absence of systematic comparative studies that evaluate different 2D platforms under identical conditions. Without such benchmarks, it remains difficult to establish clear design principles governing optimal hybrid architectures. Expanding the material palette to include less-explored 2D systems, such as black phosphorus, transition metal dichalcogenides (TMDs), boron nitride, or layered double chalcogenides, could open new opportunities to modulate electronic interactions, tailor surface chemistry, and improve structural robustness.

10.8. Limited research data in the field of MOF-derived LDH using *in situ*/*operando* characterization

More extensive research into integrating various *in situ* /*operando* characterization techniques to establish mechanistic insights is needed. A major bottleneck in the development of MOF-derived LDHs lies in the limited availability of real-time mechanistic data. Future research should prioritize the integration of complementary *in situ* and *operando* techniques such as XAS, Raman, XPS, and electrochemical impedance with advanced imaging approaches like LCTEM. When combined, these methods could provide unprecedented resolution in tracking electronic structure changes, ion diffusion, and lattice rearrangements during water splitting. Beyond conventional spectroscopy, coupling *operando* LCTEM with spectroscopic mapping will allow simultaneous monitoring of nanoscale morphology and electronic configuration in real time. Such multimodal approaches can reveal transient intermediate phases, surface reconstruction events, and defect dynamics that are otherwise overlooked.

10.9. Development in theoretical calculations

Theoretical investigations of MOF-to-LDH transformation and their subsequent application in the OER, despite recent progress, still face several fundamental challenges. The transformation from MOFs to LDHs involves complex structural collapse, ligand detachment, metal migration, and dissolution–reprecipitation events that are difficult to capture using conventional static DFT. Existing models often rely on idealized MOF structures that overlook real-world disorder, defect generation, and amorphization occurring during electrochemical activation. Furthermore, accurately simulating the roles played by solvent, hydroxide ions, local pH gradients, and electrolyte composition remains a major limitation, as traditional implicit solvent models fail to reflect the dynamic, highly hydrated environment in which LDH nucleation occurs. Another key challenge is the absence of constant-potential simulations, which limits the ability of current theoretical methods to correctly describe potential-dependent energetics, electric double-layer effects, and surface charging during the OER. Short-lived metastable intermediates observed experimentally through *operando* Raman or XAS are equally difficult to stabilize computationally, making it challenging to construct reliable mechanistic pathways. In addition, LDHs derived from MOFs often possess high defect densities, edge-exposed sites, and partially amorphous regions, features that are difficult to model using periodic slab calculations. Reactive dynamics methods such as AIMD[230] and ReaxFF[231] can, in principle, track transformation pathways, but their high computational cost restricts simulation length and system size, especially for large MOF frameworks. A further challenge lies in capturing competing thermodynamic tendencies; the same defect that enhances OER kinetics may also accelerate lattice oxygen loss or structural weakening, complicating the prediction of durability for MOF-derived electrocatalysts.

Looking ahead, several strategies can significantly strengthen theoretical studies in this domain. The adoption of constant-potential DFT and grand-canonical approaches, often *via* computational Pourbaix analysis, will enable more realistic modeling of electrochemical bias and surface charge evolution during MOF degradation and LDH formation. These Pourbaix diagrams, constructed by adjusting DFT-calculated vacuum energies for the chemical potentials of solvated ions, electrons, pH, and applied potential, provide a powerful framework for identifying stability windows, predicting dissolution potentials of metal cations, and determining when MOF-derived LDHs are prone to reconstruct or convert into amorphous oxyhydroxides under OER conditions. Grand-canonical DFT, explicit/implicit solvation models, constant-potential methods, and AIMD snapshots are increasingly recommended because they better account for electric double-layer structure, solvation stabilization, and potential-dependent restructuring. The integration of AIMD with machine-learning potentially promises to overcome computational limitations, allowing for simulations of large, defect-rich MOF structures over longer timescales. Improved reactive force fields tailored for mixed-metal MOF and LDH systems will enhance the accuracy of transformation pathway predictions. Moreover, hybrid explicit–implicit solvation models can more accurately simulate ion transport, local pH effects, and solvation dynamics at electrified interfaces. Multiscale modeling frameworks that combine DFT, reactive dynamics, mesoscale models, and the kinetic Monte Carlo method can offer a unified picture of MOF disassembly, LDH nucleation, and OER catalytic cycling. Future work integrating DFT with *in situ*/*operando* experiments, such as Raman, LCTEM, and XAS, can validate theoretical predictions, identify true active sites, and uncover transformation signatures. Advanced free-energy methodologies can further map the thermodynamic and kinetic stability of intermediates involved in framework collapse and OER turnover. Ultimately, the development of real-time computational studies of MOF-derived LDHs, incorporating defects, mixed-metal compositions, and *operando* environmental factors, holds immense potential for guiding the rational design of next-generation OER electrocatalysts.

10.10. Potential cross-disciplinary approaches

Emerging tools such as AI-driven synthesis planning and machine-learning-assisted *operando* data interpretation remain underutilized in this field. Their integration could accelerate the rational discovery of new materials and uncover hidden correlations between structure, activity, and stability. Furthermore, incorporating machine-learning-driven data analytics can accelerate the interpretation of large, complex *operando* datasets, enabling predictive insights into structure–activity–stability relationships. Establishing such mechanistic clarity will be pivotal for the rational design of robust MOF-derived LDH electrocatalysts tailored for long-term, industrially relevant operation.

10.11. Testing electrocatalysts under industry-like conditions

Establishing standardized benchmarking metrics, along with testing under industrially relevant conditions, is critical for evaluating the true practical potential of MOF-derived LDH electrocatalysts. Inconsistent experimental protocols including differences in iR correction, mass loading, and electrolyte composition make it difficult to compare results across studies. Testing under realistic operational conditions, including high current densities, long-duration electrolysis, and exposure to practical electrolytes, *e.g.*, alkaline, neutral, or seawater, will provide meaningful insights into catalyst robustness, scalability, and commercial viability. Integrating these approaches shall ensure that reported performance reflects practical applicability and accelerates the design of MOF-derived LDH catalysts suitable for real-world water-splitting devices.

In summary, thermodynamic analysis and DFT insights together yield several practical design principles for creating stable and active MOF-derived LDH electrocatalysts. First, constructing mechanically and electronically robust heterointerfaces, characterized by low interfacial formation energies, favorable lattice matching, or conformal amorphous interlayers, helps prevent delamination and ensures efficient

charge transfer during the OER. Second, while introducing defects, vacancies, and edge sites can significantly lower reaction barriers and enhance intrinsic activity, their concentration must be carefully controlled, as excessive defect densities can trigger irreversible lattice-oxygen loss and structural degradation. Third, heteroatoms and residues inherited from MOF precursors, such as phosphate or nitrogen groups, can act as stabilizing ligands that increase the dissolution potential of metal centers, thereby improving resistance to oxidative leaching. Fourth, protective yet conductive ultrathin overlayers, such as carbon coatings or doped phosphate shells, can suppress metal dissolution while maintaining high electrical conductivity. Finally, strategic alloying or trace-metal doping (*e.g.*, Fe, Cr, Mn) helps redistribute redox load across the lattice, mitigating localized over-oxidation that would otherwise accelerate catalyst breakdown. These design rules are most powerful when guided by DFT-calculated formation and segregation energies, vacancy formation costs, and Pourbaix-predicted dissolution thresholds, and subsequently validated through *operando* spectroscopy and electrolyte analysis. Collectively, such an integrated computational-experimental approach provides a rational pathway for advancing durable, high-performance MOF-derived LDH catalysts for oxygen evolution.

We anticipate that MOF-derived LDHs may turn out to be the next-generation low-cost advanced electrocatalysts for water splitting and the sustainable green energy economy. There is still plenty of room to achieve more novelty in MOF-derived LDH electrocatalysts.

Author contributions

Meena Chettri: conceptualization, literature survey, formal analysis, writing & editing – original draft; Nilankar Diyali: conceptualization, literature survey, validation; formal analysis, writing and editing draft; Bhaskar Biswas: supervision, conceptualization, funding acquisition, data curation, writing – reviewing and editing.

Conflicts of interest

The authors declare no competing financial interest.

Data availability

No primary research results, software or code have been included and no new data were generated or analysed as part of this review.

Acknowledgements

B. B. sincerely acknowledges the Anusandhan National Research Foundation (ANRF) for financial support (ANRF/IRG/2024/000343/CS). M. C. sincerely acknowledges UGC for Savitribai Jyotirao Phule Fellowship for single girl child (SJSGC) (202223-UGCES-22-GE-WES-F-SJSGC-6410). ND thanks UGC for providing fellowship (231610208373).

References

1 Y. Liu, S. Liu, Y. Wang, Q. Zhang, L. Gu, S. Zhao, D. Xu, Y. Li, J. Bao and Z. Dai, *J. Am. Chem. Soc.*, 2018, **140**, 2731–2734.
2 X. Ren, Q. Lv, L. Liu, B. Liu, Y. Wang, A. Liu and G. Wu, *Sustainable Energy Fuels*, 2019, **4**, 15–30.
3 M. Zeng and Y. Li, *J. Mater. Chem. A*, 2015, **3**, 14942–14962.
4 N. Cheng, S. Stambula, D. Wang, M. N. Banis, J. Liu, A. Riese, B. Xiao, R. Li, T. K. Sham, L. M. Liu, G. A. Botton and X. Sun, *Nat. Commun.*, 2016, **7**, 1–9.
5 A. E. Hughes, N. Haque, S. A. Northey and S. Giddey, *Resources*, 2021, **10**, 1–40.
6 J. Han, Y. Dou, J. Zhao, M. Wei, D. G. Evans and X. Duan, *Small*, 2012, **9**, 98–106.
7 X. Wan, Y. Song, H. Zhou and M. Shao, *Energy Mater. Adv.*, 2022, **2022**, 1–17.
8 D. Alves, P. R. Kasturi, G. Collins, T. N. Barwa, S. Ramaraj, R. Karthik and C. B. Breslin, *Mater. Adv.*, 2023, **4**, 6478–6497.
9 A. Farhan, A. Khalid, N. Maqsood, S. Iftekhar, H. M. A. Sharif, F. Qi, M. Sillanpää and M. B. Asif, *Sci. Total Environ.*, 2024, **912**, 169160.
10 B. F. Rivadeneira-mendoza, A. M. Tucker-qui, M. L. Gorozabel-mendoza, B. P. Iris, A. Josu, K. K. Yadav, L. A. Zambrano-intriago, A. Alberto and J. M. Rodríguez-díaz, DOI: 10.1016/j.nexus.2025.100399.
11 X. Liu, G. Verma, Z. Chen, B. Hu, Q. Huang, H. Yang, S. Ma and X. Wang, *Innovation*, 2022, **3**, 100281.
12 F. Parsapour, M. Moradi and A. Bahadoran, *Adv. Colloid Interface Sci.*, 2023, **313**, 102865.
13 M. Liu, L. Kong, X. Wang, J. He, J. Zhang, J. Zhu and X. H. Bu, *Nano Res.*, 2021, **14**, 4680–4688.
14 S. Sanati, R. Abazari, J. Albero, A. Morsali, H. García, Z. Liang and R. Zou, *Angew. Chem., Int. Ed.*, 2021, **60**, 11048–11067.
15 G. Li, L. Lu, L. Pei, Z. Ma, Y. Yuan, M. L. Hu, Q. Miao and J. Zhong, *Inorg. Chem.*, 2022, **61**, 738–745.
16 P. Vijayakumar, S. Lenus, K. Pradeeswari, M. Kumar, J. H. Chang, M. Kandasamy, M. Krishnamachari, Z. Dai, A. A. Al-Kahtani and P. Sankar Krishnan, *Energy Fuels*, 2024, **38**, 4504–4515.
17 G. Yilmaz, K. M. Yam, C. Zhang, H. J. Fan and G. W. Ho, *Adv. Mater.*, 2017, **29**, 1606814.
18 W. Wang, H. Yan, U. Anand and U. Mirsaidov, *J. Am. Chem. Soc.*, 2021, **143**, 1854–1862.
19 H. Yang, G. X. Zhang, H. J. Zhou, Y. Y. Sun and H. Pang, *Energy Mater. Adv.*, 2023, **4**, 1–30.
20 S. Weng, Q. An, Y. Xu, Y. Jiao and J. Chen, *Chemosensors*, 2023, **11**, 242.

21 H. Zou, B. He, P. Kuang, J. Yu and K. Fan, *ACS Appl. Mater. Interfaces*, 2018, **10**, 22311–22319.
22 M. Rinawati, Y. X. Wang, W. H. Huang, Y. T. Wu, Y. S. Cheng, D. Kurniawan, S. C. Haw, W. H. Chiang, W. N. Su and M. H. Yeh, *Carbon*, 2022, **200**, 437–447.
23 J. Zhao, J. Lian, Z. Zhao, X. Wang and J. Zhang, *A Review of In situ Techniques for Probing Active Sites and Mechanisms of Electrocatalytic Oxygen Reduction Reactions*, Springer Nature Singapore, 2023, vol. 15.
24 T. Zhao and Q. Zhang, *Carbon Energy*, 2020, **2**, 582–613.
25 Z. Chen, Q. Fan, J. Zhou, X. Wang, M. Huang, H. Jiang and H. Cölfen, *Angew. Chem., Int. Ed.*, 2023, **62**, e202309293.
26 D. Friebel, M. W. Louie, M. Bajdich, K. E. Sanwald, Y. Cai, A. M. Wise, M. J. Cheng, D. Sokaras, T. C. Weng, R. Alonso-Mori, R. C. Davis, J. R. Bargar, J. K. Nørskov, A. Nilsson and A. T. Bell, *J. Am. Chem. Soc.*, 2015, **137**, 1305–1313.
27 S. S. Naik, J. Theerthagiri, F. S. Nogueira, S. J. Lee, A. M.-A. Kim, G. Maia, L. M. C. Pinto and M. Y. Choi, *ACS Catal.*, 2023, **13**, 1477–1491.
28 S. Zhao, C. Tan, C. T. He, P. An, F. Xie, S. Jiang, Y. Zhu, K. H. Wu, B. Zhang, H. Li, J. Zhang, Y. Chen, S. Liu, J. Dong and Z. Tang, *Nat. Energy*, 2020, **5**, 881–890.
29 J. Linke, T. Rohrbach, A. H. Clark, M. Andrzejewski, N. P. M. Casati, F. L. Buchauer, M. R. Kraglund, C. Chatzichristodoulou, E. Meade, M. Ranocchiari, T. J. Schmidt and E. Fabbri, *Adv. Energy Mater.*, 2025, **15**, 2501401.
30 J. Linke, T. Rohrbach, A. H. Clark, M. Andrzejewski, N. P. M. Casati, E. Meade, M. Wojtas, M. Ranocchiari, T. J. Schmidt and E. Fabbri, *SusMat*, 2025, **5**, e70009.
31 J. Lyu, X. Gong, S. J. Lee, K. Gnanasekaran, X. Zhang, M. C. Wasson, X. Wang, P. Bai, X. Guo, N. C. Gianneschi and O. K. Farha, *J. Am. Chem. Soc.*, 2020, **142**, 4609–4615.
32 J. Linke, T. Rohrbach, M. Ranocchiari, T. J. Schmidt and E. Fabbri, *Curr. Opin. Electrochem.*, 2021, **30**, 100845.
33 N. Diyali, S. Diyali, M. Chettri, S. Saha, S. K. Agrawalla, H. Bagdwal, C. S. Purohit, M. Singh and B. Biswas, *ACS Appl. Mater. Interfaces*, 2025, **17**, 9351–9363.
34 S. Sanati, A. Morsali and H. García, *Energy Environ. Sci.*, 2022, **15**, 3119–3151.
35 S. Sanati, R. S. Varma, M. Liu and R. Abazari, *Energy Environ. Sci.*, 2025, 7733–7755.
36 M. Etesami, S. R. Motlagh, R. Khezri, M. Gopalakrishnan, J. Theerthagiri, M. Y. Choi, K. Nootong, A. Somwangthanaroj and S. Kheawhom, *EnergyChem*, 2024, **6**, 100128.
37 T. Zhao, Y. Wang, S. Karuturi, K. Catchpole, Q. Zhang and C. Zhao, *Carbon Energy*, 2020, **2**, 582–613.
38 R. Abazari, S. Sanati, W. K. Fan, M. Tahir, S. Nayak, K. Parida, M. El-Shahat, R. M. Abdelhameed, D. S. Nesterov, A. M. Kirillov and J. Qian, *Coord. Chem. Rev.*, 2025, **523**, 216256.
39 J. Zhu, L. Hu, P. Zhao, L. Y. S. Lee and K. Y. Wong, *Chem. Rev.*, 2020, **120**, 851–918.
40 M. N. Lakhan, A. Hanan, A. Hussain, I. A. Soomro, Y. Wang, M. Ahmed, U. Aftab, H. Sun and H. Arandiyan, *Chem. Commun.*, 2024, **60**, 5104–5135.
41 M. Chettri, S. Saha, N. Diyali, R. Debnath, H. Bagdwal, M. Singh and B. Biswas, *Sustainable Energy Fuels*, 2024, **8**, 5553–5560.
42 N. Diyali, S. Diyali, S. J. Panda, C. S. Purohit, G. K. Dalapati and B. Biswas, *ACS Appl. Energy Mater.*, 2025, **8**, 14346–14362.
43 A. Debnath, N. Diyali, S. Diyali, S. K. Agrawalla, A. Hassan, H. Bagdwal, M. Singh, M. A. Dar, C. S. Purohit, G. K. Dalapati and B. Biswas, *Appl. Energy Mater.*, 2025, **8**, 7575–7582.
44 S. Saha, N. Diyali, S. Diyali, S. J. Panda, M. Das, S. Acharya, P. K. Mudi, M. Singh, P. P. Ray, C. S. Purohit and B. Biswas, *Dalton Trans.*, 2024, **53**, 13805–13814.
45 S. Zhao, Z. H. Wang, J. Y. Wang, P. F. Wang, Z. L. Liu, J. Shu and T. F. Yi, *Coord. Chem. Rev.*, 2025, **524**, 216321.
46 S. Diyali, N. Diyali, M. Das, M. Joshi, P. P. Ray, M. S. A. Sher Shah, A. Roy Choudhury and B. Biswas, *Cryst. Growth Des.*, 2022, **22**, 7590–7602.
47 A. Debnath, S. Diyali, M. Das, S. J. Panda, D. Mondal, D. Dhak, C. S. Purohit, P. P. Ray and B. Biswas, *Dalton Trans.*, 2023, **52**, 8850–8856.
48 S. Diyali, S. Saha, N. Diyali, A. Bhattacharjee, A. Mallick, S. K. Agrawalla, C. S. Purohit and B. Biswas, *ChemSusChem*, 2024, **18**, e202401089.
49 N. Diyali, M. Chettri, S. Saha, A. Saha, S. Kundu, D. Mondal, D. Dhak and B. Biswas, *CrystEngComm*, 2023, **25**, 6837–6844.
50 Y. Zheng, Y. Jiao, Y. Zhu, L. H. Li, Y. Han, Y. Chen, M. Jaroniec and S. Z. Qiao, *J. Am. Chem. Soc.*, 2016, **138**, 16174–16181.
51 H. Dau, C. Limberg, T. Reier, M. Risch, S. Roggan and P. Strasser, *ChemCatChem*, 2010, **2**, 724–761.
52 C. G. Morales-Guio, L. A. Stern and X. Hu, *Chem. Soc. Rev.*, 2014, **43**, 6555–6569.
53 J. K. Nørskov, T. Bligaard, A. Logadottir, J. R. Kitchin, J. G. Chen, S. Pandelov and U. Stimming, *J. Electrochem. Soc.*, 2005, **152**, J23.
54 J. Song, C. Wei, Z. F. Huang, C. Liu, L. Zeng, X. Wang and Z. J. Xu, *Chem. Soc. Rev.*, 2020, **49**, 2196–2214.
55 G. Zuo, H. Wang and Y. Wang, *Langmuir*, 2025, **41**, 10727–10741.
56 X. Liu, L. Zhang and J. Wang, *J. Mater.*, 2021, **7**, 440–459.
57 G. Wang, D. Huang, M. Cheng, S. Chen, G. Zhang, L. Lei, Y. Chen, L. Du, R. Li and Y. Liu, *Coord. Chem. Rev.*, 2022, **460**, 214467.
58 M. Zhu, W. Cai, H. Wang, L. He and Y. Wang, *J. Alloys Compd.*, 2021, **884**, 160931.
59 Y. Zhu, W. Du, Q. Zhang, H. Yang, Q. Zong, Q. Wang, Z. Zhoua and J. Zhana, *Chem. Commun.*, 2020, **56**, 13848–13851.
60 M. Decker, Q. Lenne, J. Ghilane and C. M. Sánchez-sánchez, *Curr. Opin. Electrochem.*, 2025, **53**, 101728.

61 B. Wang, X. Han, C. Guo, J. Jing, C. Yang, Y. Li, A. Han, D. Wang and J. Liu, *Appl. Catal., B*, 2021, **298**, 120580.
62 B. C. Shi, M. Jin, Y. Zou, S. Wang, Y. Nie, D. Yao and Y. J. Tang, *Rare Met.*, 2025, 1–11.
63 S. S. Veroneau, A. C. Hartnett, J. Ryu, H. Hong and G. Daniel.
64 R. Zhang, G. Van Straaten, V. Palma, G. Zafeiropoulos, W. M. M. Kessels, M. N. Tsampas and M. Creatore. DOI: 10.1021/acscatal.0c04933.
65 C. Environments, DOI: 10.1021/acsenergylett.1c01350.
66 J. Zhu, X. F. Lu, D. Luan, X. Wen and D. Lou, DOI: 10.1002/anie.202408846.
67 H. Shi, T.-Y. Dai, W.-B. Wan, Z. Wen, X.-Y. Lang and Q. Jiang, *Adv. Funct. Mater.*, 2021, **31**, 2102285.
68 S. Li, J. Li, X. Wang, Y. Sun, Z. Tang, X. Gao, H. Zhang, J. Xie, Z. Yang and Y. M. Yan, *Small*, 2024, **20**, 1–10.
69 J. Liang, H. Luo, T. Lei and G. Yang, *Sustainable Energy Fuels*, 2024, **8**, 2682–2694.
70 B. Wang, S. Jiao, Z. Wang, M. Lu, D. Chen, Y. Kang, G. Pang and S. Feng, *J. Mater. Chem. A*, 2020, **8**, 17202–17211.
71 X. Wang, X. Zong, B. Liu, G. Long, A. Wang, Z. Xu, R. Song, W. Ma, H. Wang and C. Li, *Small*, 2022, **18**, 1–12.
72 L. Yu, H. Zhou, J. Sun, F. Qin, F. Yu, J. Bao, Y. Yu, S. Chen and Z. Ren, *Energy Environ. Sci.*, 2017, **10**, 1820–1827.
73 Y. Wei, Z. Han, T. Liu, X. Ding and Y. Gao, *ChemCatChem*, 2024, **202400447**, 1–5.
74 X. Zhao, Y. Zheng, H. Dai, J. Yang, Q. Chen, J. Zhou and G. Sun, *Adv. Mater. Interfaces*, 2022, **9**, 2102595.
75 J. Huo, Y. Wang, L. Yan, Y. Xue, S. Li, M. Hu, Y. Jiang and Q. G. Zhai, *Nanoscale*, 2020, **12**, 14514–14523.
76 M. Xiao, C. Wu, J. Zhu, C. Zhang, Y. Li, J. Lyu, W. Zeng, H. Li, L. Chen and S. Mu, *Nanoresearch*, 2023, **16**, 8945–8952.
77 Q. Dong, C. Shuai, Z. Mo, R. Guo, N. Liu, G. Liu, J. Wang, W. Liu, Y. Chen, J. Liu, Y. Jiang and Q. Gao, *CrystEngComm*, 2021, **23**, 1172–1180.
78 S. Sk, R. Madhu, D. S. Gavali, V. Bhasin, R. Thapa, S. N. Jha, D. Bhattacharyya, S. Kundu and U. Pal, *J. Mater. Chem. A*, 2023, **11**, 10309–10318.
79 K. Jayaramulu, S. Mukherjee, D. M. Morales, D. P. Dubal, A. K. Nanjundan, A. Schneemann, J. Masa, S. Kment, W. Schuhmann, M. Otyepka, R. Zbořil and R. A. Fischer, *Chem. Rev.*, 2022, **122**, 17241–17338.
80 B. Ruqia and S. Il Choi, *ChemSusChem*, 2018, **11**, 2643–2653.
81 M. A. Qadeer, X. Zhang, M. A. Farid, M. Tanveer, Y. Yan, S. Du, Z. F. Huang, M. Tahir and J. J. Zou, *J. Power Sources*, 2024, **613**, 234856.
82 J. Jiang, C. Xi, Y. Zhao, Y. Zhu, K. Hu, Y. Wang, S. Wang, Z. Zhang and S. Han, *ACS Catal.*, 2025, **15**, 2561–2575.
83 L. Hu, R. Xiao, X. Wang, X. Wang, C. Wang, J. Wen, W. Gu and C. Zhu, *Appl. Catal., B*, 2021, **298**, 120599.
84 N. Li, T. Yang, L. Huang, H. Jiang, J. Xiao, X. Ma, H. Lou, C. Xie and Y. Yang, *ACS Appl. Mater. Interfaces*, 2023, **14**, 52530–52541.
85 G. K. Gebremariam, A. Z. Jovanović and I. A. Pašti, *Hydrogen*, 2023, **4**, 776–806.
86 K. Chen, B. Xu, L. Shen, D. Shen, M. Li and L. H. Guo, *RSC Adv.*, 2022, **12**, 19452–19469.
87 W. Sheng, H. A. Gasteiger and Y. Shao-Horn, *J. Electrochem. Soc.*, 2010, **157**, B1529.
88 J. Durst, C. Simon, F. Hasché and H. A. Gasteiger, *J. Electrochem. Soc.*, 2015, **162**, F190–F203.
89 R. Subbaraman, D. Tripkovic, K. C. Chang, D. Strmcnik, A. P. Paulikas, P. Hirunsit, M. Chan, J. Greeley, V. Stamenkovic and N. M. Markovic, *Nat. Mater.*, 2012, **11**, 550–557.
90 N. M. Marković, S. T. Sarraf, H. A. Gasteiger and P. N. Ross, *J. Chem. Soc., Faraday Trans.*, 1996, **92**, 3719–3725.
91 T. Shinagawa and K. Takanabe, *Phys. Chem. Chem. Phys.*, 2015, **17**, 15111–15114.
92 L. Amaral, D. S. P. Cardoso, B. Šljukić, D. M. F. Santos and C. A. C. Sequeira, *Mater. Res. Bull.*, 2019, **112**, 407–412.
93 R. Zhang, P. E. Pearce, Y. Duan, N. Dubouis, T. Marchandier and A. Grimaud, *Chem. Mater.*, 2019, **31**, 8248–8259.
94 T. J. Wang, X. Liu, Y. Li, F. Li, Z. Deng and Y. Chen, *Nano Res.*, 2020, **13**, 79–85.
95 M. Rinawati, Y. X. Wang, K. Y. Chen and M. H. Yeh, *Chem. Eng. J.*, 2021, **423**, 130204.
96 F. Zheng, M. A. Gaikwad, Z. Fang, S. Jang and J. H. Kim, *Energy Fuels*, 2024, **38**, 6290–6299.
97 L. Hu, R. Xiao, X. Wang, X. Wang, C. Wang, J. Wen, W. Gu and C. Zhu, *Appl. Catal., B*, 2021, **298**, 120599.
98 L. Yin, X. Du, C. Di, M. Wang, K. Su and Z. Li, *Chem. Eng. J.*, 2021, **414**, 128809.
99 W. Da Zhang, Q. T. Hu, L. L. Wang, J. Gao, H. Y. Zhu, X. Yan and Z. G. Gu, *Appl. Catal., B*, 2021, **286**, 119906.
100 J. Huang, K. Li, L. Wang, H. She and Q. Wang, *Chin. Chem. Lett.*, 2022, **33**, 3787–3791.
101 H. Xu, C. Shan, X. Wu, M. Sun, B. Huang, Y. Tang and C. H. Yan, *Energy Environ. Sci.*, 2020, **13**, 2949–2956.
102 L. Ye, J. Wang, Y. Zhang, M. Zhang, X. Jing and Y. Gong, *Appl. Surf. Sci.*, 2021, **556**, 149781.
103 X. Wang, J. He, B. Yu, B. Sun, D. Yang, X. Zhang, Q. Zhang, W. Zhang, L. Gu and Y. Chen, *Appl. Catal. B Environ.*, 2019, **258**, 117996.
104 Y. Zhou, Y. Chen, M. Wei, H. Fan, X. Liu, Q. Liu, Y. Liu, J. Cao and L. Yang, *CrystEngComm*, 2021, **23**, 69–81.
105 J. F. Qin, M. Yang, T. S. Chen, B. Dong, S. Hou, X. Ma, Y. N. Zhou, X. L. Yang, J. Nan and Y. M. Chai, *Int. J. Hydrogen Energy*, 2020, **45**, 2745–2753.
106 B. Chen, D. Kim, Z. Zhang, M. Lee and K. Yong, *Chem. Eng. J.*, 2021, **422**, 130533.
107 N. Han, S. Luo, C. Deng, S. Zhu, Q. Xu and Y. Min, DOI: 10.1021/acsami.0c19839.
108 P. He, X. Y. Yu and X. W. D. Lou, *Angew. Chem., Int. Ed.*, 2017, **56**, 3897–3900.
109 H. Jiang, S. Zhang, Q. Fu, L. Yan, J. Zhang and X. Zhao, *Molecules*, 2023, **28**, 2280.

110 J. Zhang, N. Cheng and B. Ge, *Adv. Phys. X*, 2022, **7**, 2046157.
111 M. Barawi, C. A. Mesa, L. Collado, I. J. Villar-García, F. Oropeza, V. A. de la Peña O'Shea and M. García-Tecedor, *J. Mater. Chem. A*, 2024, **12**, 23125–23146.
112 W. Shen, Y. Ye, Q. Xia and P. Xi, *EES Catal.*, 2025, **3**, 10–31.
113 T. Xia, Y. Yang, Q. Song, M. Luo, M. Xue, K. K. Ostrikov, Y. Zhao and F. Li, *Nanoscale Horiz.*, 2023, **8**, 146–157.
114 Y. Zhan, T. Yang, S. Liu, L. Yang, E. Wang, X. Yu, H. Wang, K. Chou and X. Hou, *Nanomaterials*, 2025, **15**, 917.
115 Q. Qi, C. Zhang and J. Hu, *Coord. Chem. Rev.*, 2025, **522**, 216235.
116 C. L. Jones, C. E. Hughes, H. H. M. Yeung, A. Paul, K. D. M. Harris and T. L. Easun, *Chem. Sci.*, 2021, **12**, 1486–1494.
117 W. Cheng, X. Zhao, H. Su, F. Tang, W. Che, H. Zhang and Q. Liu, *Nat. Energy*, 2019, **4**, 115–122.
118 L. Liu, W. Li, X. He, J. Yang and N. Liu, *Small*, 2022, **18**, 1–22.
119 S. Zuo, Z. P. Wu, H. Zhang and X. W. Lou, *Adv. Energy Mater.*, 2022, **12**, 2103383.
120 C. Han, M. T. Islam and C. Ni, *ACS Omega*, 2021, **6**, 6537–6546.
121 K. Gnanasekaran, K. M. Vailonis, D. M. Jenkins and N. C. Gianneschi, *ACS Nano*, 2020, **14**, 8735–8743.
122 J. P. Patterson, P. Abellan, M. S. Denny, C. Park, N. D. Browning, S. M. Cohen, J. E. Evans and N. C. Gianneschi, *J. Am. Chem. Soc.*, 2015, **137**, 7322–7328.
123 Q. Chang, D. Yang, X. Zhang, Z. Ou, J. Kim, T. Liang, J. Chen, S. Cheng, L. Cheng, B. Ge, E. H. Ang, H. Xiang, M. Li and X. Song, *Nanoscale*, 2023, **15**, 13718–13727.
124 X. Su, Y. Wang, J. Zhou, S. Gu, J. Li and S. Zhang, DOI: 10.1021/jacs.8b05294.
125 J. Hu, T. Guo, X. Zhong, J. Li, Y. Mei, C. Zhang, Y. Feng, M. Sun, L. Meng, Z. Wang, B. Huang, L. Zhang and Z. Wang, *Adv. Mater.*, 2024, **36**, 2310918.
126 A. Orlando, F. Franceschini, C. Muscas, S. Pidkova, M. Bartoli, M. Rovere and A. Tagliaferro, *Chemosensors*, 2021, **9**, 262.
127 Y. Deng, A. D. Handoko, Y. Du, S. Xi and B. S. Yeo, *ACS Catal.*, 2016, **6**, 2473–2481.
128 Y. Deng and B. S. Yeo, *ACS Catal.*, 2017, **7**, 7873–7889.
129 S. Lee, K. Banjac, M. Lingenfelder and X. Hu, *Angew. Chemie Int. Ed.*, 2019, **58**, 10295–10299.
130 L. F. Olbrich, B. Jagger, J. Ihli and M. Pasta, *ACS Energy Lett.*, 2024, **9**, 3636–3642.
131 R. M. S. Yoo, D. Yesudoss, D. Johnson and A. Djire, *ACS Catal.*, 2023, **13**, 10570–10601.
132 M. Chatenet, B. G. Pollet, D. R. Dekel, F. Dionigi, J. Deseure, P. Millet, R. D. Braatz, M. Z. Bazant, M. Eikerling, I. Staffell, P. Balcombe, Y. Shao-Horn and H. Schäfer, *Chem. Soc. Rev.*, 2022, **51**, 4583–4762.
133 X. Zhao, H. Su, W. Cheng, H. Zhang, W. Che, F. Tang and Q. Liu, *ACS Appl. Mater. Interfaces*, 2019, **11**, 34854–34861.
134 W. Cheng, X. Zhao, H. Su, F. Tang, W. Che, H. Zhang and Q. Liu, *Nat. Energy*, 2019, **4**, 115–122.
135 S. Zhu, X. Qin, Y. Yao and M. Shao, *J. Am. Chem. Soc.*, 2020, **142**, 8748–8754.
136 R. R. Rao, M. J. Kolb, L. Giordano, A. F. Pedersen, Y. Katayama, J. Hwang, A. Mehta, H. You, J. R. Lunger, H. Zhou, N. B. Halck, T. Vegge, I. Chorkendorff, I. E. L. Stephens and Y. Shao-Horn, *Nat. Catal.*, 2020, **3**, 516–525.
137 Y. Tang, J. Li, Z. Lu, Y. Wang, K. Tao and Y. Lin, *Nanomaterials*, 2023, **13**, 2621.
138 Z. Xiao, Y. Huang, C. Dong, C. Xie, Z. Liu, S. Du, W. Chen, D. Yan, L. Tao, Z. Shu, G. Zhang, H. Duan, Y. Wang, Y. Zou, R. Chen and S. Wang, *J. Am. Chem. Soc.*, 2020, **142**, 12087–12095.
139 J. Chen, H. Li, Z. Yu, C. Liu, Z. Yuan, C. Wang, S. Zhao, G. Henkelman, S. Li, L. Wei and Y. Chen, *Adv. Energy Mater.*, 2020, **10**, 2002593.
140 C. H. M. Van Oversteeg, H. Q. Doan, F. M. F. de Groot and T. Cuk, *Chem. Soc. Rev.*, 2017, **46**, 102–125.
141 J. Li, R. Güttinger, R. Moré, F. Song, W. Wana and G. R. Patzke, *Chem. Sci. Rev.*, 2017, **46**, 6124–6147.
142 K. Zhu, X. Zhu and W. Yang, *Angew. Chem., Int. Ed.*, 2019, **58**, 1252–1265.
143 M. Newville.
144 D. Joseph, S. Basu, S. N. Jha and D. Bhattacharyya, *Nucl. Instrum. Methods Phys. Res., Sect. B*, 2012, **274**, 126–128.
145 J. Timoshenko and B. R. Cuenya, *Chem. Rev.*, 2021, **121**, 882–961.
146 M. Risch, D. M. Morales, J. Villalobos and D. Antipin, *Angew. Chem., Int. Ed.*, 2022, **61**, e202211949.
147 M. E. Kreider and M. Burke, *ChemElectroChem*, 2023, **10**, e202200958.
148 Z. Wu, H. Zhang, S. Zuo, Y. Wang, S. L. Zhang, J. Zhang, S. Zang, X. Wen and D. Lou, *Adv. Mater.*, 2021, **33**, 2103004.
149 R. Zhang, Q. Wu, P. Sherrell, D. Li, K. Huang, J. Chen and X. Yao, *Sci. China Chem.*, 2023, **66**, 2221–2237.
150 K. Nakanishi and T. Ohta, DOI: 10.1002/sia.3870.
151 P. Macarena, V. Bokhoven, A. Jeroen, P. Zimmermann, S. Peredkov, P. Macarena and S. Debeer, *Coord. Chem. Rev.*, 2025, **423**, 213466.
152 W. Cheng, S. Xi, Z. Wu, D. Luan, X. W. David Lou and D. Lou, *Sci. Adv.*, 2021, **7**, 1–10.
153 L. Nguyen, F. F. Tao, Y. Tang, J. Dou and X. Bao, *Chem. Rev.*, 2019, **119**, 6822–6905.
154 K. Siegbahn, *J. Electron Spectros. Relat. Phenomena*, 1974, **5**, 3–97.
155 D. M. Littrell and B. J. Tatarchuk, *J. Vac. Sci. Technol. A*, 1986, **4**, 1608–1612.
156 H. Ali-lo, M. W. Louie, M. R. Singh, L. Li, H. G. S. Casalongue, H. Ogasawara, E. J. Crumlin, Z. Liu, A. T. Bell, A. Nilsson and D. Friebel, *J. Phys. Chem. C*, 2016, **120**, 2247–2253.
157 L. Nguyen and F. F. Tao, *Rev. Sci. Instrum.*, 2016, **87**, 064101.

158 Y. Wang, D. Yan, S. El Hankari, Y. Zou and S. Wang, *Adv. Sci.*, 2018, **5**, 1800064.
159 E. Skúlason, V. Tripkovic, M. E. Björketun, S. Gudmundsdóttir, G. Karlberg, J. Rossmeisl, T. Bligaard, H. Jónsson and J. K. Nørskov, *J. Phys. Chem. C*, 2010, **114**, 18182–18197.
160 E. Fabbri and T. J. Schmidt, DOI: 10.1021/acscatal.8b02712.
161 J. A. Gauthier, C. F. Dickens, L. D. Chen, A. D. Doyle and J. K. Nørskov, DOI: 10.1021/acs.jpcc.7b02383.
162 J. A. Gauthier, S. Ringe, C. F. Dickens, A. J. Garza, A. T. Bell, M. Head-gordon, J. K. Nørskov and K. Chan, *ACS Catal.*, 2018, **9**, 920–931.
163 S. Ringe, G. H. Nicolas, H. Oberhofer and K. Reuter, *Chem. Rev.*, 2022, **122**, 10777–10820.
164 Z. Wang, W. A. Goddard IIII and H. Xiao, *Nat. Commun.*, 2023, **14**, 4228.
165 Z. Huang, J. Song, Y. Du, S. Xi, S. Dou, J. Marie, V. Nsanzimana, C. Wang, Z. J. Xu and X. Wang, *Nat. Energy*, 2019, **4**, 329–338.
166 S. C. Cho, J. H. Seok, H. N. Manh, J. H. Seol, C. H. Lee and S. U. Lee, *Nano Converg.*, 2025, **12**, 1–27.
167 Z. Wu, D. T. Caracciolo, Y. Maswadeh, J. Wen, Z. Kong, S. Shan, J. A. Vargas, S. Yan, E. Hopkins, K. Park, A. Sharma, Y. Ren, V. Petkov, L. Wang and C. Zhong, *Nat. Commun.*, 2021, 1–14.
168 W. Da Zhang, H. Yu, T. Li, Q. T. Hu, Y. Gong, D. Y. Zhang, Y. Liu, Q. T. Fu, H. Y. Zhu, X. Yan and Z. G. Gu, *Appl. Catal., B*, 2020, **264**, 118532.
169 L. Tang, M. Xia, S. Cao, X. Bo, S. Zhang, Y. Zhang, X. Liu, L. Zhang, L. Yu and D. Deng, *Nano Energy*, 2022, **101**, 107562.
170 J. Zhang, J. Liu, L. Xi, Y. Yu, N. Chen, S. Sun, W. Wang, K. M. Lange and B. Zhang, *J. Am. Chem. Soc.*, 2018, **140**, 3876–3879.
171 Y. Wang, F. L. Hu, Y. Mi, C. Yan and S. Zhao, *Chem. Eng. J.*, 2021, **406**, 127135.
172 M. W. Louie and A. T. Bell, *J. Am. Chem. Soc.*, 2013, **135**, 12329–12337.
173 Z. Yan, H. Sun, X. Chen, H. Liu, Y. Zhao, H. Li, W. Xie, F. Cheng and J. Chen, *Nat. Commun.*, 2018, **9**, 1–9.
174 Q. He, Y. Wan, H. Jiang, Z. Pan, C. Wu, M. Wang, X. Wu, B. Ye, P. M. Ajayan and L. Song, *ACS Energy Lett.*, 2018, **3**, 1373–1380.
175 Z. Liu, H. Li, H. Sen Kang, A. T. N'Diaye and M. H. Lee, *Chem. Eng. J.*, 2023, **454**, 140403.
176 R. N. Dürr, P. Maltoni, H. Tian, B. Jousselme, L. Hammarström and T. Edvinsson, *ACS Nano*, 2021, **15**, 13504–13515.
177 S. Zhao, D. Zhang, S. Jiang, Y. Cui, H. Li, J. Dong, Z. Xie, D. W. Wang, R. Amal, Z. Xia and L. Dai, *Nano Res.*, 2021, **14**, 3329–3336.
178 J. Song, J. Chen, Z. Xu and R. Y. Lin, *Chem. Commun.*, 2022, **58**, 10655–10658.
179 J. Du, F. Li and L. Sun, *Chem. Soc. Rev.*, 2021, **50**, 2663–2695.
180 L. He, Y. Zhou, M. Wang, S. Li and Y. Lai, *Nanomaterials*, 2024, **14**, 1533.
181 V. Vishwakarma, N. Diyali, A. De, A. R. Choudhury and B. Biswas, *ChemPlusChem*, 2025, **90**, e202500177.
182 S. Liu, Y. Zhang, L. Hao, A. Nsabimana and S. Shen, *Sep. Purif. Technol.*, 2025, **354**, 129501.
183 K. Sielicki, G. Leniec, B. Zielin, A. Dymerska and S. Bartosz, *J. Energy Chem.*, 2023, **86**, 263–276.
184 C. Han, Y. Lv, X. Tang, S. Zhang, Y. Jiang, Z. Lu and S. Dai, *Nano Energy*, 2025, **25**, 11484–11491.
185 M. Rinawati, Y. Wang, K. Chen and M. Yeh, *Chem. Eng. J.*, 2021, **423**, 130204.
186 R. Ramachandran, Y. Lan, Z. Xu and F. Wang, *ACS Appl. Energy Mater.*, 2020, **3**, 6633–6643.
187 J. Timoshenko and B. R. Cuenya, *Chem. Rev.*, 2021, **121**, 882–961.
188 M. Wilhelm, A. Bastos, C. Neves, R. Martins and J. Tedim, *Mater. Des.*, 2021, **212**, 110188.
189 K. Karuppasamy, R. Bose, D. B. Velusamy, D. Vikraman, P. Santhoshkumar, P. Sivakumar, A. Alfantazi and H. Kim, *ACS Sustainable Chem. Eng.*, 2022, **10**, 14693–14704.
190 C. Wu, H. Li, Z. Xia, X. Zhang, R. Deng, S. Wang and G. Sun, *ACS Catal.*, 2020, **10**, 11127–11135.
191 B. W. Xue, C. H. Zhang, Y. Z. Wang, W. W. Xie and N. Li, *Nanoscale Adv.*, 2020, **2**, 5555–5566.
192 C. Li, Y. Bao, E. Liu, B. Zhao and T. Sun, *Molecules*, 2023, **28**, 1475.
193 Y. Ni, D. Shi, B. Mao, S. Wang, Y. Wang and A. Ahmad, *Small*, 2023, **19**, 2302556.
194 Z. Liu, J. Ge and J. Hu, *Inorg. Chem. Front.*, 2025, **12**, 6246–6256.
195 X. Ma, D. J. Zheng, S. Hou, S. Mukherjee, R. Khare, G. Gao, Q. Ai, B. Garlyyev, W. Li, M. Koch, J. Mink, Y. Shao-Horn, J. Warnan, A. S. Bandarenka and R. A. Fischer, *ACS Catal.*, 2023, **13**, 7587–7596.
196 X. Ma, L. Schr, G. Gao, Q. Ai, M. Zarrabeitia, C. Liang, M. Z. Hussain, R. Khare, K. Song, D. J. Zheng, M. Koch, I. E. L. Stephens, S. Hou, Y. Shao-horn, J. Warnan, A. S. Bandarenka and R. A. Fischer, *ACS Catal.*, 2024, **14**, 15916–15926.
197 Z. Zhao, Q. Shao, J. Xue, B. Huang, Z. Niu, H. Gu, X. Huang and J. Lang, *Nano Res.*, 2022, **15**, 310–316.
198 S. Jiang, M. Wu, Z. Xu, J. Zhao and R. Liu, *Colloids Surf., A*, 2023, **677**, 132400.
199 G. Zhao, K. Rui, S. X. Dou and W. Sun, *Adv. Funct. Mater.*, 2018, **28**, 1–26.
200 Y. Zhai, X. Ren, Y. Sun, D. Li, B. Wang and F. Liu, *Appl. Catal., B*, 2023, **323**, 122091.
201 X. Guo, X. Zheng, X. Hu, Q. Zhao, L. Li, P. Yu and C. Jing, *Nano Energy*, 2021, **84**, 105932.
202 D. Wu, X. Hu, Z. Yang, T. Yang, J. Wen, G. Lu, Q. Zhao, Z. Li, X. Jiang and C. Xu, *Ind. Eng. Chem. Res.*, 2022, **61**, 7523–7528.
203 Q. Shi, H. Liu, J. Liang, Y. Zhang, Y. Dong, W. Yang and Q. Liu, *Int. J. Hydrogen Energy*, 2022, **47**, 16047–16055.

204 S. Sirisomboonchai, S. Li, A. Yoshida, X. Li, C. Samart, A. Abudula and G. Guan, *ACS Sustainable Chem. Eng.*, 2019, **7**, 2327–2334.
205 Z. Gao, T. Ma, X. Chen, H. Liu, L. Cui, S. Qiao, J. Yang and X.-W. Du, *Small*, 2018, **1800195**, 1800195.
206 Y. Li, H. Guo, Y. Zhang, H. Zhang, J. Zhao and R. Song, *J. Mater. Chem. A*, 2022, **10**, 18989–18999.
207 H. Su, J. Jiang, N. Li, Y. Gao and L. Ge, *Chem. Eng. J.*, 2022, **446**, 137226.
208 P. Zhai, C. Wang, Y. Zhao, Y. Zhang, J. Gao, L. Sun and J. Hou, *Nat. Commun.*, 2023, **14**, 1873.
209 Q. Dong, J. Zhou, Y. Li, J. Liu, Y. Wen, J. Wang, X. He, Q. Jin and Z. Sun, *J. Alloys Compd.*, 2025, **1038**, 182828.
210 Z. Li, X. Zhang, Y. Kang, C. C. Yu, Y. Wen, M. Hu, D. Meng, W. Song and Y. Yang, *Adv. Sci.*, 2021, **8**, 2002631.
211 J. Li, H. Sun, L. Lv, Z. Li, X. Ao, C. Xu, Y. Li and C. Wang, *ACS Appl. Mater. Interfaces*, 2019, **11**, 8106–8114.
212 J. Huo, Y. Wang, L. Yan, Y. Xue, S. Li, M. Hu, Y. Jiang and Q. Zhai, *Nanoscale*, 2020, **12**, 14514–14523.
213 Z. Chen, D. Wang, T. Li, Y. Chen, C. Su, W. Wang, C. Dong, X. Shan and Z. Chen, *ACS Appl. Energy Mater.*, 2025, **8**, 8262–8269.
214 J. Wang, Z. Zhao, M. Guo, L. Xiao, H. Tang, J. Li, Z. Kou and J. Li, *EES Catal.*, 2024, **2**, 862–873.
215 B. R. Wygant, K. Kawashima and B. Mullins, *ACS Energy Lett.*, 2018, **3**, 2956–2966.
216 R. Ahmed, A. E. Allah, A. A. Farghali, W. M. A. El Rouby and A. Abdelwahab, *Nanoscale Adv.*, 2025, **7**, 5401–5410.
217 D. Y. Chung, P. P. Lopes, P. Farinazzo Bergamo Dias Martins, H. He, T. Kawaguchi, P. Zapol, H. You, D. Tripkovic, D. Strmcnik, Y. Zhu, S. Seifert, S. Lee, V. R. Stamenkovic and N. M. Markovic, *Nat. Energy*, 2020, **5**, 222–230.
218 L. Bai, C. Hsu, D. T. L. Alexander, H. M. Chen and X. Hu, *J. Am. Chem. Soc.*, 2019, 14190–14199.
219 R. Ahmed, E. Allah, A. A. Farghali and M. A. El Rouby, *Nanoscale Adv.*, 2025, **7**, 5401–5410.
220 F. Zheng, M. A. Gaikwad and J. H. Kim, *Korean J. Mater. Res.*, 2023, **33**, 377–384.
221 Z. W. Chen, L. X. Chen, Z. Wen and Q. Jiang, *Phys. Chem. Chem. Phys.*, 2019, **21**, 23782–23802.
222 B. S. Hammes-schiffer, *Science*, 2017, **355**, 28–29.
223 A. S. Raman, R. Patel and A. Vojvodic, *Faraday Discuss.*, 2021, **229**, 75–88.
224 M. M. Melander, *npj Comput. Mater.*, 2024, **10**, 1–11.
225 D. Le, *Catalysis*, 2023, **1**, 1–25.
226 J. Huang, *J. Chem. Theory Comput.*, 2023, **19**, 1003–1013.
227 H. Cao, X. Lv, S. Qian, J. Li and Y. Wang, *J. Phys. Chem. Lett.*, 2024, **15**, 1314–1320.
228 J. Sheng, J. Kang, P. Jiang, K. Meinander, X. Hong, H. Jiang, O. Ikkala, H. Komsa, B. Peng and Z. Lv, *Small*, 2025, **21**, 2404927.
229 F. Chen, Z. Wu, Z. Adler and H. Wang, *Joule*, 2021, **5**, 1704–1731.
230 C. Arntsen, C. Chen and G. A. Voth, *Chem. Phys. Lett.*, 2017, **683**, 573–578.
231 T. P. Senftle, S. Hong, M. Islam, S. B. Kylasa, Y. Zheng, Y. K. Shin, C. Junkermeier, R. Engel-herbert, M. J. Janik, H. M. Aktulga, T. Verstraelen, A. Grama and A. C. T. Van Duin, *npj Comput. Mater.*, 2016, **2**, 15011.